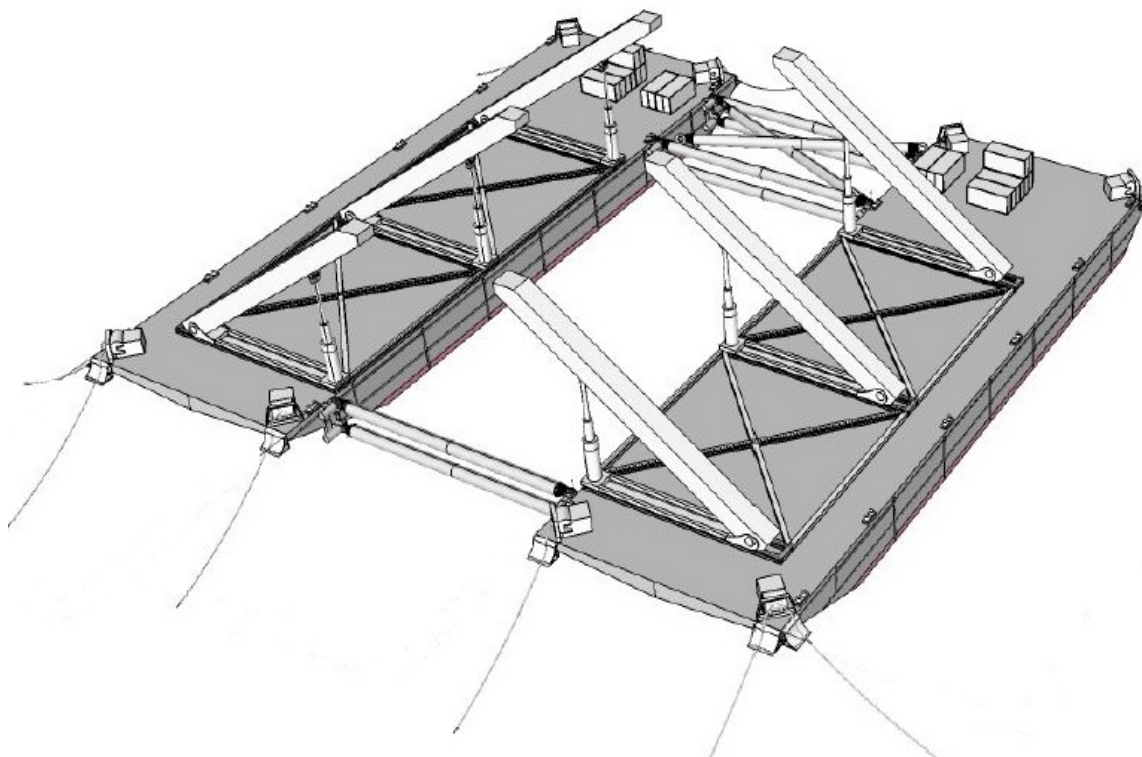# Mammoet Offshore Platform

"Hydrodynamic Assessment & Motion Optimization of Mechanically Coupled Barges"

Vasileios A. Mathios

TUDelft
Delft University of Technology

Challenge the future

MAMMOET

Mammoet Offshore Platform
"Hydrodynamic Assessment & Motion Control of Mechanically Coupled Barges"

MASTER OF SCIENCE THESIS

For the degree of Master of Science in Offshore and Dredging Engineering
Faculty of Mechanical, Maritime and Materials Engineering
Delft University of Technology

Vasileios A. Mathios
4305507

Delft, November 2015

DELFT UNIVERSITY OF TECHNOLOGY
DEPARTMENT OF OFFSHORE AND DREDGING ENGINEERING

The undersigned hereby certify that they have read and recommend to the Faculty of Mechanical, Maritime and Materials Engineering for acceptance a thesis under the title

MAMMOET OFFSHORE PLATFORM "HYDRODYNAMIC ASSESSMENT & MOTION CONTROL OF MECHANICALLY COUPLED BARGES"

VASILEIOS A. MATHIOS

in partial fulfillment of the requirements for the degree of

MASTER OF SCIENCE
OFFSHORE AND DREDGING ENGINEERING

Chairman of Graduation Committee: _____
       Prof. Dr. A. V. Metrikine

Company Supervisor (Mammoet BV)   _____
       Ir. H. Jansen

University Daily Supervisor: _____
       Dr. Ir. J. W. van Wingerden

University Thesis Counsellor: _____
       Ir. A. van der Stap

Abstract

The decommissioning market expenditure is expected to grow further in the years to come due to increasing number of platforms that near the end of their production cycle, mainly being fixed steel structures ($<$4,000 [Te]) positioned in shallow waters (30 to 75 [m]). The risks of such operation emerged the need for semi-submersible, heavy-lift vessel or ultimately catamaran vessel design (i.e Pioneering Spirit), all being expensive concepts with high lifting capacities making a single-lift option possible, also ensuring robust operating windows; however, these designs are tailored to be project-specific and technically redundant.

Such way of thinking do not comply with the lean, modular and reusable engineering philosophy Mammoet Global Engineering is introducing via its novel conceptual design counterproposal, under the name Mammoet Offshore Platform (MOP); a twin barge concept with proper mechanical couplings would create a modular and thus resusable, less stiff configuration that achieves operational robustness in irregular seas.

The technical challenge identified is the asymmetric barge roll motion due to the eccentric topside weight and the respective roll hydrodynamic loading. Roll motion in beam waves (90^{0} angle of attack) is expected to be the dominant design parameter and is addressed via the implementation of a kinematic constraint so that barges and topside roll (φ) is synchronized. Furthermore, the barges are modeled to heave and pitch independently, therefore significant differential motions in the corresponding DOF (*bank* : ρ & *flip* : χ) are anticipated and need to be treated; the use of a passive link, modeled as a spring-dashpot, has qualified while its structural parameters will be optimized with the H_∞ technique.

The research question in hand comprises of MOP concept technical feasibility study which will be quantitatively assessed via the following Key Performance Indices (KPI):

- Steady-state dynamic behavior of MOP (constrained barges) against two free floating barges and a catamaran barge of identical geometry specifications, working entirely in the frequency domain (modeling in linear potential solver Wamit)

- Steady-state dynamic behavior of MOP (constrained barges & link optimized in H_∞) against the model identified in the previous analysis (state-space modeling and control in Matlab)

The frequency domain simulations for the case studies tabulate that the roll kinematic constraint has successfully attenuated & shifted the peak response while the link structural properties optimization has minimized the differential barge motions in heave and pitch ensuring wider operational windows and verifying this workflow as a proof of concept.

Acknowledgements

This line of research (also refer to the works of Janssen (2013); Benne (2014); Wang (2015)) would never have been carried out without Henk Jansen, the mind & soul behind this original idea of wave effect identification applied in multibody structures. I will always be in debt to him for his countless hours of tutoring and counselling; always passionate to explore and convey his knowledge and sparkling thoughts to his disciples;

My gratefulness goes also to Satish Prabhakar, associate supervisor of this Thesis, being the exclusive factor of the hydrodynamics analysis successful implementation. Always there to tutor me and share his thoughts and precious insight selflessly throughout this (almost) 2-year journey of mine in Mammoet Naval.

Prof. Jan-Willem van Wingerden is the single person who took me in and got me familiarized to control techniques, being patient and always available to help me with whatever came my way. His faith to me and this application will never be forgotten.

Special thanks to prof. Metrikine and ir. van der Stap for their valuable help in this work; their input is deeply appreciated.

This Thesis is dedicated to my parents, Jenny and Tasos and my sister, Evi for their 26-year non-stop love & care. My thoughts are always on you.

Contents

List of Figures

Chapter 1

Introduction

1.1 North Sea Decommissioning

Projected North Sea decommissioning activity estimates vary, with the most conservative predicting that the market will require more than 30 bn pounds of expenditure before 2040 in the UK Continental Shelf (UKCS) alone (Sea (2014)). This estimation comes from the fact that oil & gas companies operating in North Sea have been successfully producing offshore since the 70's so virtually all infrastructure put in place will require to be decommissioned within the next few years (2015-2040; peaking at 2023) in a safe manner, a task that must be carried out in one of the harshest marine environments (Jamieson (2013)).
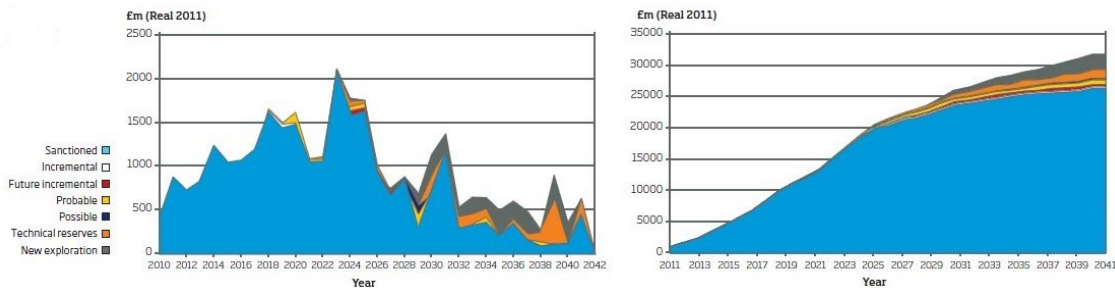
Figure 1.1.1: Potential Decomissioning Expenditure (Year-by-Year & Cumulative) 2010-2040Jamieson (2013)

As for the technicalities implemented, the challenge that shapes the decommissioning market needs lies within the heterogeneity of the types, designs and weights of the offshore structures present in the area, while the waterdepth and metocean also varies significantly. However, one can identify a pattern on a decommissioning sub-market comprised of platforms of certain type and weight, positioned in shallow waters; more specifically, 4 out of 5 North Sea offshore structures are fixed with steel substructures in waterdepths ranging from $30\ to\ 75[m]$ while weighing less than $4,000\ [mt]$, thus characterized as relatively light steel structures.
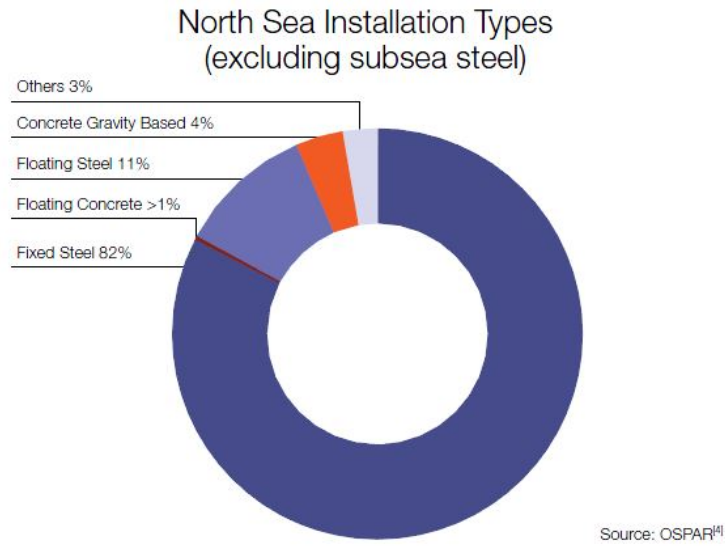
(a) Installation Types in North Sea
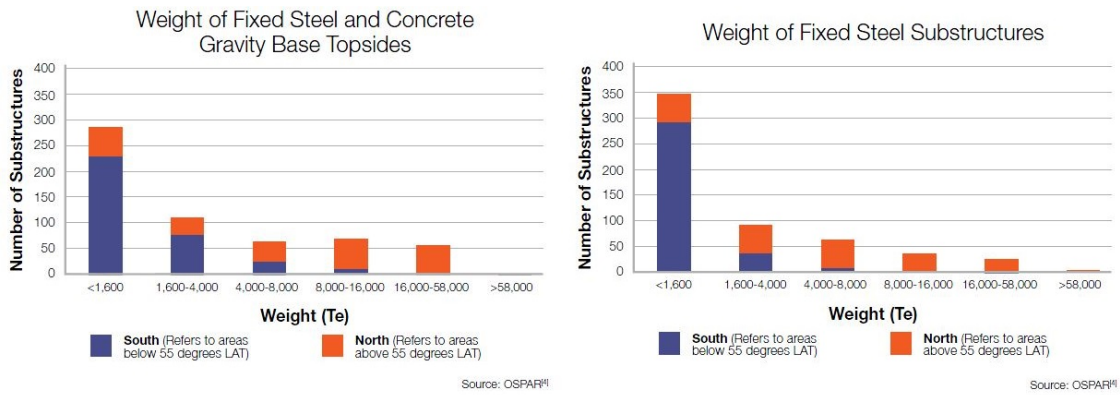
(b) Topside & Sustructure Weights in North Sea

Figure 1.1.2: North Sea Installation Types & Weights (OSPAR©)
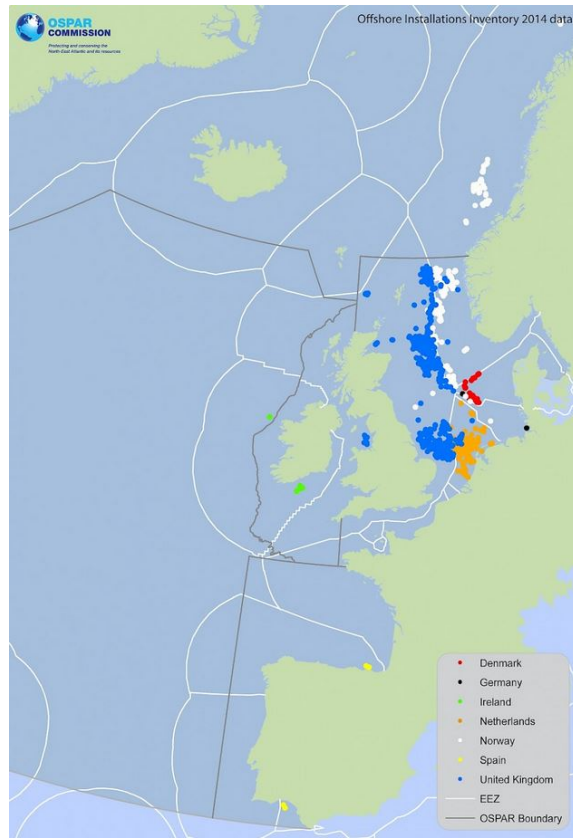
(a) Total Number of Installations
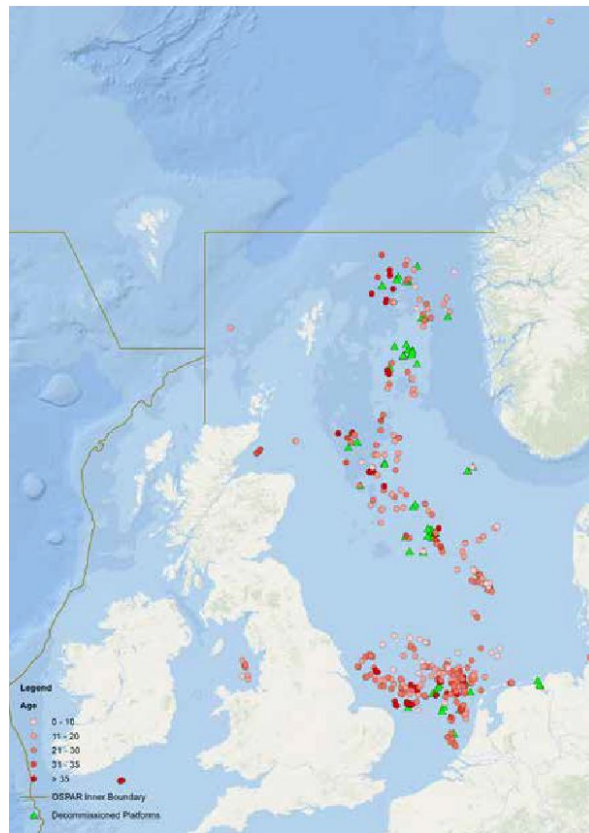
(b) Structures to be decommissioned

Figure 1.1.3: North Sea Installations & Decommissioning Prospects (OSPAR©)

The decommissioning approach taken is subject to a comparative assessment by the contractor, considering the technical feasibility, health, safety & environmental (HSE) impact, economic implications of each approach, presented as follows:

- Piece-small: The installation is disassembled offshore by getting cut into small sections that can be shipped back to shore. This method requires the most offshore resources (cranes, lifting devices, automated cutters, tugs, transport barges etc) being time consuming mainly due to the heavy workload of dismantling. Therefore, it only qualifies as a decommissioning approach when the topside/substructrure structural integrity is in question. Additionally, it is a method that may qualify in case that single lift operation is not possible or proper offshore equipment is not available.

- Reverse installation: the topside is seperated from the jacket and removed with a single integrated lift or multiple module lifts by a specialized vessel (semi-sub crane & heavy lift vessels) while (most of) the substructure is removed with a reverse float-over, ultimately making the whole operation the exactly reversed process of an installation. This method would require less manual labor offshore but it still employs a lot of resources and manhours. Examples of these semi-subs are Heerema's Balder and Thialf, Saipem's S7000 and as for the heavy lift vessels Seaway's Stanislav Yudin etc.

(a) Balder   (b) Stanislav Yudin
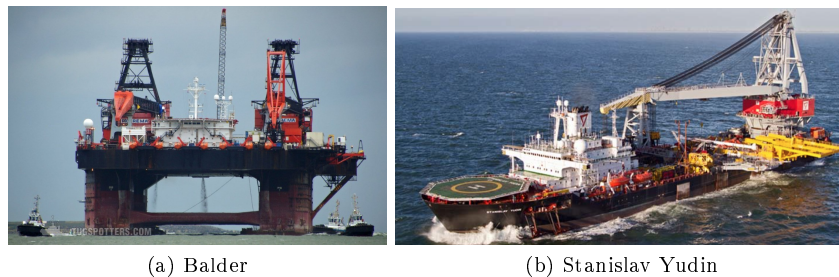
Figure 1.1.4: Examples of SSCV and HLV

- Single Lift: The topsides and substructure are removed in one piece and shipped back onshore for decommissioning and recycling in the yard. Several companies have designs of single lift decommissioning units but the only vessel being developed is Allseas's Pioneering Spirit, a 382x123m vessel as large as two super tankers and in catamaran shape, able to single lift up to 48,000 tonnes.

(a) Pioneering Spirit (Catamaran Design)   (b) Versabar (Multibody Concept)

Figure 1.1.5: Single Lift Solutions

1.2 Research Motivation & Previous In-House Research

The stimulus for Mammoet Innovation department to start the engineering research for a decommissioning floating unit was YME platform removal in 2012, a contract which was finally awarded to Allseas. The decommissioning operation will be carried out on a single lift by the Pioneering Spirit, a gigantic catamaran structure with a capacity to lift more than twice the weight of YME heavyweight platform (23,000 tonnes). Such engineering solutions are thus considered to be excessively stiff and expensive for the current decommissioning market needs; furthermore, monolithic structures like the Pioneering Spirit (catamaran) or the Versabar concept (multibody configuration - refer to figure 1.1.5b) serve decommissioning purposes only and cannot be reused in other offshore operations, a rationale that conflicts Mammoet philosophy on lean, modular and reusable engineering multi-purpose solutions.

Its counterproposal, Mammoet Offshore Platform (MOP) complies to this philosophy by introducing a lighter configuration consisting of relatively cheap cargo barges upon which hydraulic cranes are mounted and simple (passive) structural components that couple the barges mechanically. This solution is investigated under the research hypothesis that by *fine-tuning the structural properties of the configuration intermediate components the system hydrodynamic steady-state response will be manipulated so that the desired operational conditions are met (robust system performance for a design sea state).*

Under that scope, Mammoet Global Engineering B.V. under Henk Jansen started a line of research on the identification of the wave effect on multibody structures, aiming to ultimately come up with an innovative design that will be tailored for offshore decommissioning applications. Janssen (2013) was the first to suggest that the frequency domain hydrodynamic analysis carried out in-house with the radiation-diffraction potential solver Wamit should be identified (fitted) in a linear, time-invariant state space model, a common tool by control engineers for fast time-domain simulations and control algorithm synthesis. He accomplished to create a radiation force-to-motion system subspace identification MATLAB algorithm for multi-input, multi-output (MIMO) systems, such as the vessel-wave model. The physical constraints (stability, passivity, low- and high-frequency asymptotic behavior tending to zero) are imported to the algorithm as model properties that constrain the identified model. This prior knowledge of the model was successfully enforced onto the identified radiation models via his constrained frequency-domain subspace identification (CFDSI).

Janssen's line of work was succeded by Wang (2015) who recreated the CFDSI algorithm in Python workflow and also accomplished to enforce the model properties to the identified state-space model with improved accuracy. Wang also tested his algorithm to various case studies that were hydrodynamically modeled for the present study, namely one free barge, two mechanically uncoupled and coupled barges, thus extending the script into multibody cases. Finally, he modeled the transient dynamics of the coupled topside-lift cylinders-barges system during lift-off, coming to the conclusion that *if the barges roll is synchronized then the topside heave is attenuated resulting in a quicker acquisition of the desired safety clearance between the jacket and the topside.*

Benne (2014) made his contribution by elaborating a topside removal market overview, developing an analysis tool of comparing the different removal methods so to come with the two qualifying; one would introduce the topside's selfweight as a roll moment via hydraulic cranes to the barges whereas the other would transfer it to the barges center of gravity (COG) through gantry beams. Both were hydrodynamically tested and Benne pointed out that the models are successfully coupled mechanically but that the heave and pitch kinematic constraints (differential heave and pitch motion attenuation) were judged to be "infeasible" for a design significant wave height of $H_s = 1.0 \ [m]$.

(a) Scissors   (b) Gantry
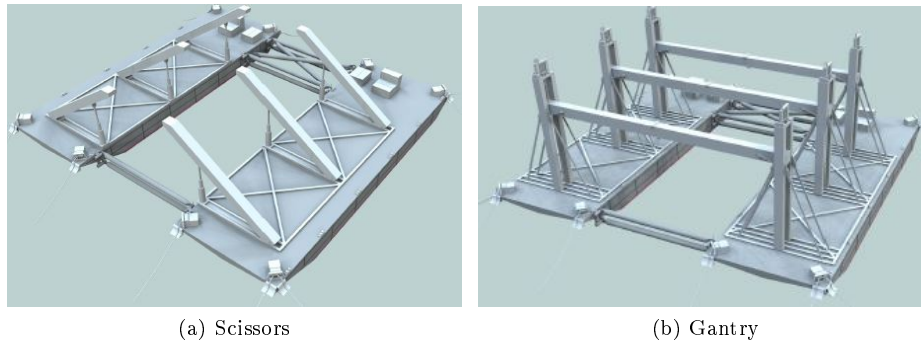
Figure 1.2.1: Two qualifying methods

1.3   MOP Concept Problem Description

The limiting operational issue identified in the previous in-house research was the hydrodynamic roll moment acting in *asymetric fashion* on the barges, resulting in significant shear stresses and bending moments on the topside when attached to the multibody configuration. Additionally, in 100% load transfer, topside's weight would add vertical heave forcing on barges while its eccentric centre of gravity with respect to the barges COG result in structural *anti-phase* roll moment, superimposed to the hydrodynamic heave and roll forces, respectively. *The effect of the coupled topside is forcing the barges to rotate into (roll) and drift away (sway) from each other* as it is graphically illustrated in figure 1.3.1a. Hydrodynamic roll beam forces are expected to be the dominant design parameter for the configuration therefore the option of implementing a holonomic constraint to the transverse direction is chosen by employing two rigid bars so to connect the twin barges. The barges will therefore roll in a synchronized manner as visualized in figure 1.3.1b.Throughout the hydrodynamic analysis, the bars will just be utilized as kinematic constraints, thus being unstiffened and undamped. The kinematic constraint is expected to attenuate and shift the peak roll response in the frequency domain approach; however if the response is still considered high, proper performance filter component W_P will be designed so to properly address the excessive roll motion.

(a) Assymetric roll moment treated by link (Wang (2015)) (b) Synchronized Roll
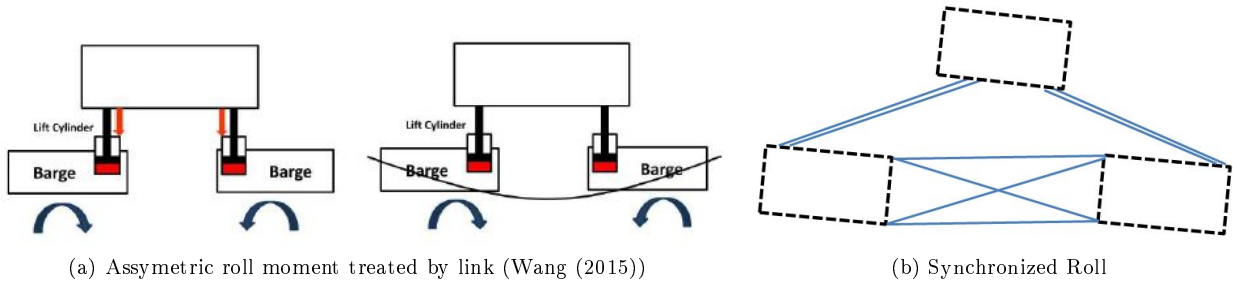
Figure 1.3.1: Assymetric Roll Moment & Kinematic Constraint

As for the heave and pitch force response amplitude operators (RAO), they are expected to be relatively lower in magnitude (which correspond to lower spectral wave energy to be treated) and dominant in quartering seas; the wave direction of 45 *degrees* is thus investigated. For theses degrees, the application of a similar kinematic constraint similar to the one employed in roll degree of freedom would not be recommended as this would result at an infeasible, stiff design Benne (2014); alternatively, the differential heave normalized by the gap between the barges (abbr. ρ) and differential pitch (abbr. χ), which from now on will be referred as *bank* and *flip*, respectively, will be treated by tuning the structural properties of the link bars; the link damping will be assumed constant and will be estimated with respect to the radiation damping while the link stiffness will be properly optimized with H_∞ synthesis techniques (refer to Chapter 3).

(a) Bank Topside Rotation (2D artist impression) (b) Link Structure
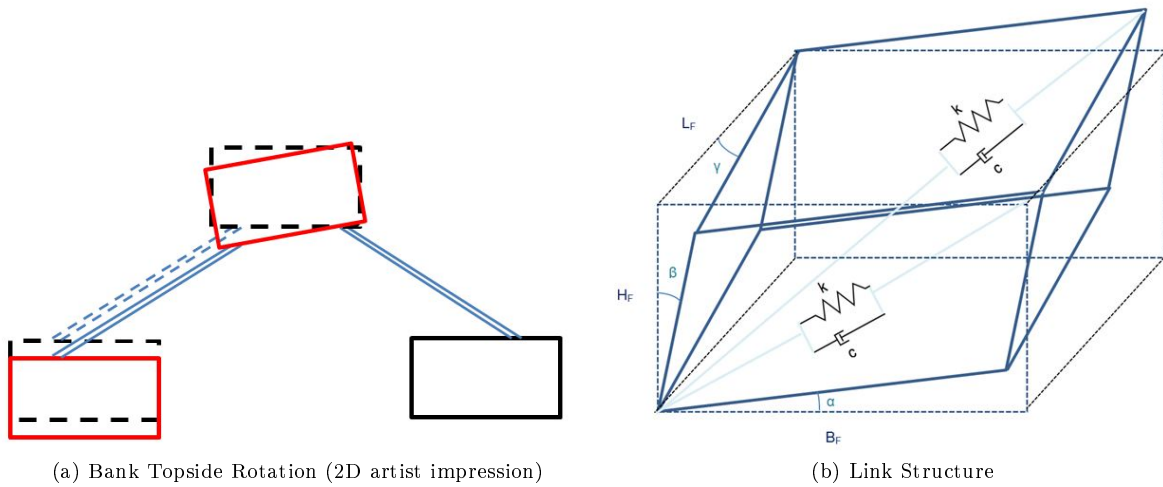
Figure 1.3.2: Bank Topside Rotation & Link Model Visualization

1.4 Research Question & Thesis Objective

This Thesis poses the following research question: " *Would an engineering solution like MOP (twin crane barges kinematically constrained in roll and stiffened in heave and pitch) be technically feasible in terms of operability on a North Sea environment?* ". Answering that question, the interconnected barges-link-waves model will be built up in frequency domain (Phase A - Chapter 2) and state-space representation (Phase B - Chapter 3) where link structural parameters will be optimized so that the system steady-state response is fitted to the operational requirements. More specifically, MOP technical feasibility study will be assessed via the following Key Performance Indices:

- Steady-state responce of MOP (without link bars) against two free floating barges and a catamaran barge of identical geometry specifications; the case study modeling is carried out in linear potential solver Wamit;

- Steady-state response of MOP (link properties optimized in H_∞ synthesis framework) against the MOP model without the link; the state space modeling and optimization is carried out in Matlab.

The objective is to successfully model the aforementioned case studies in Phase A and the interconnected system in Phase B which requires the identification of the waves-barges physical processes, verify numerically that the roll kinematic constraint is reducing the barges peak roll amplitude and the barges differential heave and pitch motion is minimized via the link properties optimization by selecting the closed-loop transfer function to meet an admissible performance standard γ. Ultimately, this numerical model workflow will be verified as a proof of the MOP concept and open wider conversation for further development in the future.

1.5 Solution Approach & Report Format

For the method used for this application, 3 dual barge case studies will be modeled and simulated in frequency domain linear radiation & diffraction potential solver Wamit, namely 2 free barges (Case A1), one catamaran barge (Case A2 - borrowing the idea developed in the Pioneering Spirit design) and 2 barges constrained in roll via kinematic constraint. The frequency-related output (hydr. added mass $A(j\omega)$ and damping $B(j\omega)$) will be employed so to derive the radiation and diffraction state-space models using the subspace identification algorithm (CFDSI) developed by Janssen. Working entirely in linear, time-invariant, state-space framework, the interconnection between the wave effect, barges and link state-space models will be made. Finally, the link stiffness optimization will be delivered by utilizing the non-convex, non-smooth algorithm elaborated by Apkarian and Noll (2006) and the effects of this passive element on the systems behavior will be illustrated in postprocessing.

Research Steps

- Model 3 diverse multibody case studies in linear radiation-diffraction solver Wamit; compare and elaborate on their responses in frequency domain; verify the necessity of designing a kinematic constraint in roll only;

- Identify the JONSWAP wave spectrum in state-space; the radiation and diffraction state-space models by using the CFDSI algorithm; build up the state-space model describing the waves-multibody configuration interaction (generalized plant P); define the passive link component with tunable parameters $C(\theta)$;

- Apply the H_∞ synthesis method to derive the link properties resulting in suboptimal system performance γ; define performance filter control component W_p to treat the excessive roll if needed;

- Simulate the dynamic response of the integrated barges-link model both in frequency and time-domain.
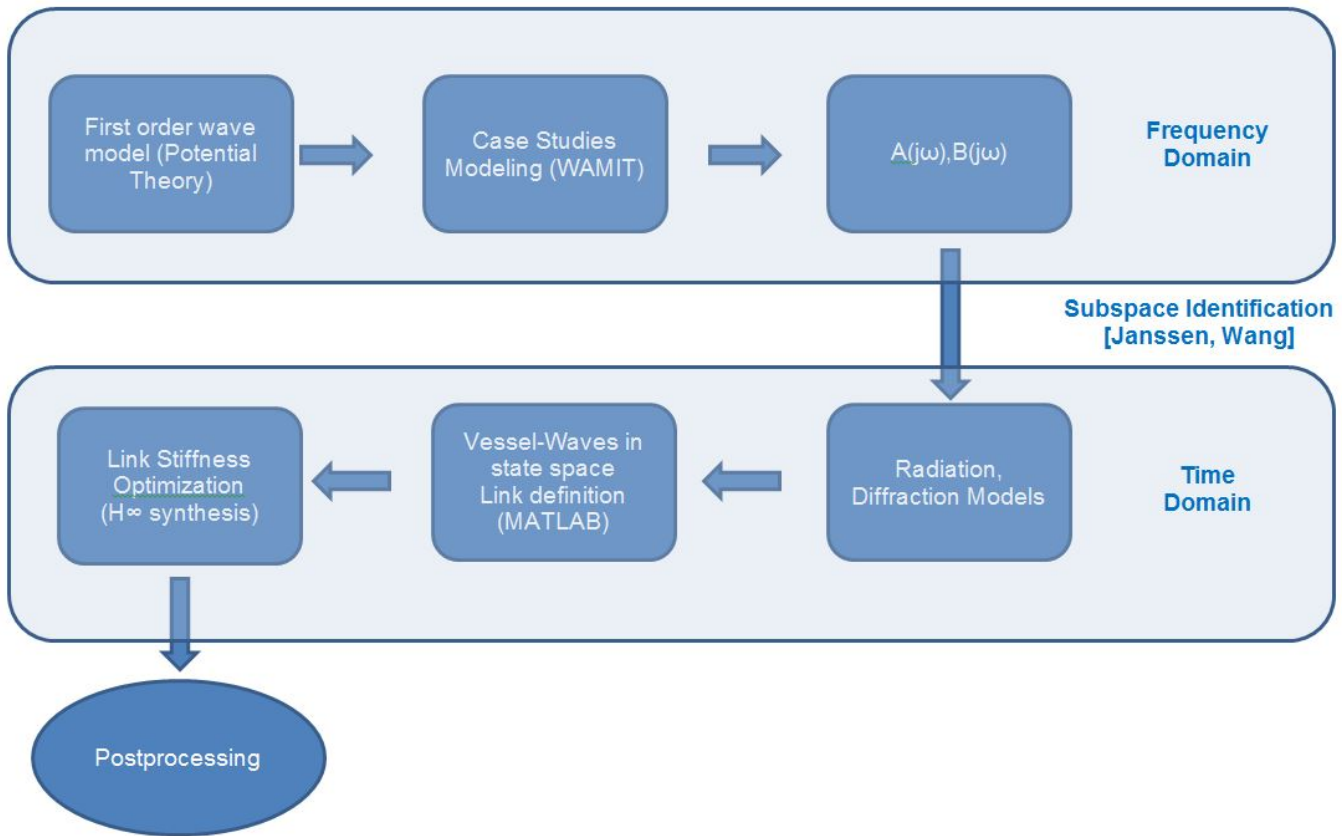
Figure 1.5.1: Method of Approach Flowchart

Chapter 2 illustrates the line of thinking behind the case studies modeling in frequency domain via Wamit solver, determining the hydrodynamic coefficients which will be the input data for the identification algorithm used later on and concluding by explaining the modeling choices made with the help of the motion/force RAO plots produced in postprocessing. Chapter 3 presents the state-space modeling process with all physical processes identified, how the link is defined and the H_∞ optimization tool used; the respective conclusions are drawn with the simulation postprocessed graphs. Finally, Chapter 4 summarizes the work done in both phases of analysis (hydrodynamics and H_∞ synthesis) and comes to the final research conclusions, recommending possible paths for similar studies in the future.

In Appendices A & B the essential background one needs to cover on ship hydrodynamics and motion control is provided, in order for readers from different disciplines to get aligned to the research modeling and simulation (Chapters 2-3) carried out. Appendix A focuses on potential theory assumptions and describing equations, ship kinematics and kinetics, introduction in multibody hydrodynamic interactions, wave effect state-space identification and model reduction. Appendix B summarizes the fundamentals on classical feedback control (closed-loop transfer function, evaluating closed-loop stability and performance), the definitions of a matrix infinite norm and weight sensitivity in MIMO models and a synopsis of H_∞ control, presenting the classical convex optimization approach and paying more attention to the fixed-order, fixed-structure synthesis approach used herein, essentially making the problem non-convex; its solution comes through a non-smooth algorithm developed by Apkarian and Noll (2006).

Chapter 2

MOP Hydrodynamics

The scope of this section is to present the line of thinking leading to the final configuration case study in terms of system motions in vertical displacement (heave) and in- & out-plane rotations (roll and pitch) degrees of freedom by ultimately designing a link mechanism with respect to the following *parameters*:

- *modularity*; the link shall be a separate module easily detachable from the barges, ensuring their maximum independence for other operations and minimum *complexity* for barge's optimum *mobility;*

- *cost effectiveness*; the link should optimize the engineering compromise made between system differential motions in the aforementioned degrees of freedom while being economically feasible (minimum steel and damper usage);

- *robustness*; the link should drastically broaden the system's operational windows (compared to the two free barges case study) for a maximum sea state of $H_{1/3} = 3[m], T_z = 9[sec]$.

At this point of analysis, 3 diverse multibody configurations will be modeled and their hydrodynamic behavior in frequency domain will be evaluated and compared via the postprocessed motion & force RAO. The goal of this comparison is to visualize the beneficial effect of the roll constraint to the systems response and also show graphically that the heave and pitch constraints as depicted in the catamaran case study do not offer the corresponding added value to a model's hydrodynamic performance. Therefore, the point made is that a more flexible connection where barges can heave and pitch independently would be more beneficial in terms of cost/performance trade off. However, the differential heave and pitch deflections are expected to be significant and shall therefore be treated with passive control (Chapter 3).

2.1 Case Studies Description

First, the barge selection and its geometry dimensions and inertia properties along with the qualifying multibody shape configuration will be briefly presented. The hydrodynamic behavior of one unmoored barge will be examined first (Run A0); for the sake of economy, the input data will be shown only once since they will be utilized in all runs in an identical manner; any differences in between runs, if encountered, will be duly noted. The hydrodynamic coupling in between two identical, unmoored barges (12 DOF's) with an incorporated gap of 65 $[m]$ will be modeled (Run A1) and compared to the case A0. The objective is to quantitatively estimate the diffraction and shielding effect due to the presence of a multibody configuration and examine model's validity.

(a) A0 - One Free Barge   (b) A1 - Two free barges
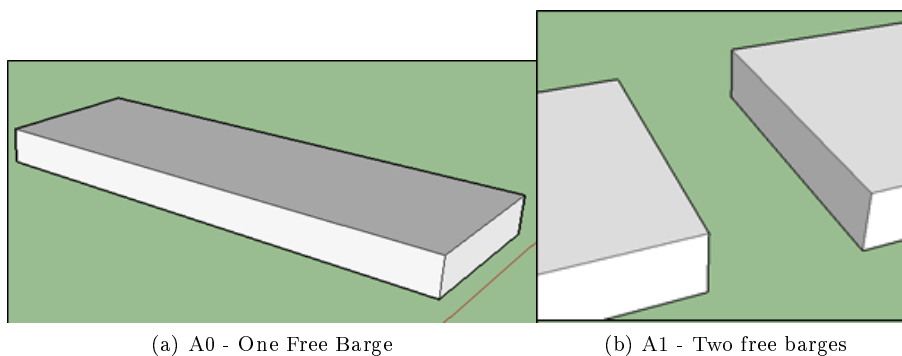
Figure 2.1.1: A0 - A1 case studies

The effect of mechanical coupling is researched on next; first a single-body catamaran barge (run A2) will be modeled and its responses will be compared to the A1 multibody run. The catamaran barge is practically a multibody configuration with all rigid-body degrees of freedom fully coupled mechanically; therefore the 12DOF system is automatically reduced to a 6DOF. The added value of this comparison (Runs A1-A2) is that it will provide the upper and lower threshold values of body amplitude for the final case study A3 - semi stiffened barges, where *two identical unmoored bodies are fully constrained in roll plus all the horizontal DOFs; surge, sway and yaw degrees of freedom and can vibrate independently to the remaining degrees of heave and pitch.* The final model will be a multibody, unmoored, constrained case study with $12 - 4 = 8$ degrees of freedom. The barge's state vector for the final case study with respect to a reference frame O with its origin in the middle of the center line connecting the two barges COG in y axis would be: $b = (x, y, z_1, z_2, \varphi, \theta_1, \theta_2, \psi)^T$. Ultimately, the resulting RAO of both barges in the final case study should be identical in the mechanically coupled DOFs, both in amplitude and phase, in order to validate the success of the model process. The challenge in the modeling comes with the Wamit V7.06 interface, since it does not allow the user to insert kinematic constraints to the system or facilitate the researcher with a GUI interface (e.g. pick up objects and couple them mechanically with 3D trusses or rod elements); although the hull geometry generation and interaction is based on the fundamentals of finite element method, the user interface is not modular and everything has to be scripted with proper input files. The method of imposing kinematic constraints in multibody configurations (K∞ method) will be further elaborated in a separate section below.

(a) A2 - Catamaran Barge   (b) A3 - Semi stiffened Barges
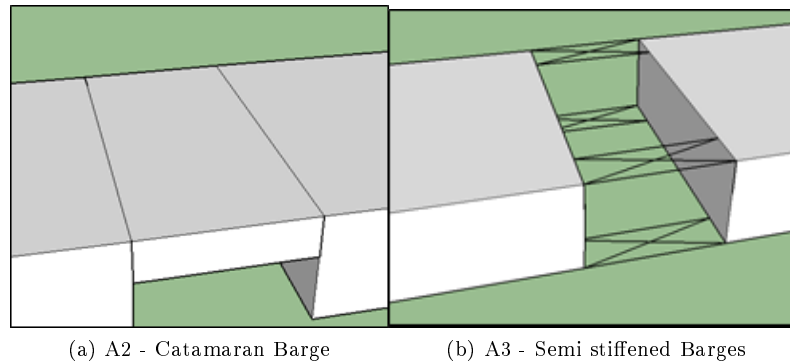
Figure 2.1.2: A2 - A3 case studies

2.2 Barge Specifications

The stimulus for this case study is based on the in-house enquiry for further research and development on the topic of offshore multibody dynamics in the last 2 years. An in-house market research and preliminary conceptual study has been elaborated in order to come up with this final barge specification (basic dimensions and inertia-ballast properties) and multibody configuration. Single medium-sized barge was judged to perform under par, especially in lift off. As for the different multibody configurations, the strength-weakness-opportunity-threat (SWOT) analysis qualified a two barge configuration positioned parallel to each other, which is easier to position underneath the platform and in between the substructure piling and behaves more efficiently in comparative hydrodynamic analysis (ballast & unloaded, ballast and fully loaded) when compared to a T-shaped or L-shaped barge configuration.

(a) Single barge with submerged ballast tanks in Tshape   (b) Two barges in parallel with supporting submerged ballast tanks
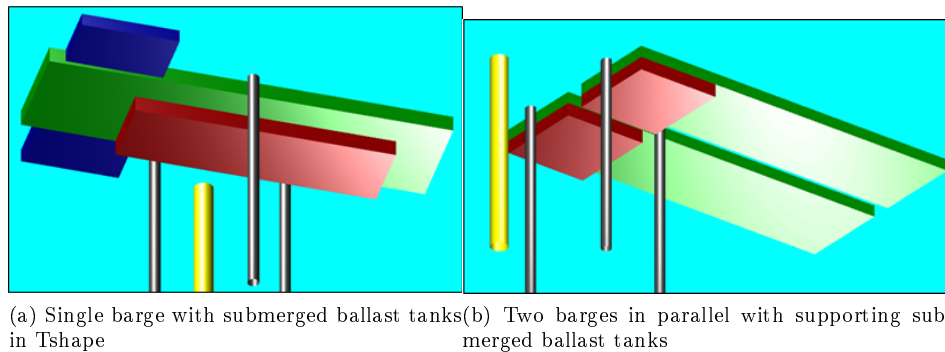
Figure 2.2.1: Previous in-house concepts

The configurations that were disqualified were experiencing resonant low-frequency responses in roll, sway and pitch DOF when loaded whereas the U-shaped had a smoother and attenuated response due to its configuration symmetry, while the 2 floating bodies provide broader waterplane area which enhances the configuration stabilization in vertical degrees of freedom, especially during the lift-off phase.

The latter concept suggested that the barges shall approach the supporting structure with their

aft; this approach causes a high pitching arm, thus unsually high load introduction to the barge. That operational issue would be overcome by adding extra ballast via submerged tanks attached to the barges keel. The new concept of mechanically coupled barges with proper passive link mechanism introduces a distance between the vessels which make it possible for them to properly maneuver around and place the platform in the middle of the configuration.

In terms of barge dimensions, the analyses were carried out for case study rectangular box-shaped barges, based on the specifications of Saipem Castoro XI which is considered to be a LFS (large floating structure) with 150x40x9 [m]. At this point, the analysis comprises of the geometry modeling of the configurations, solving the radiation/scatter problem in Wamit for the desired frequency range and wave directionality (ω, β) and compares the RAO of different configurations in the DOF of interest. On the table below the barge specifications used for the analysis and will be universally applied in all runs are provided.

Barge Specifications (Saipem Castoro XI)		
LOA	150	[m]
Breadth	40	[m]
Depth	9	[m]
Maximum draught	6.5	[m]
Gross tonnage	15400	[ton]
Cargo deadweight	29469	[ton]
Ballast tank capacity	38975	[m^3]

(a) Barge basic geometry specifications   (b) Saipem Castoro XI

Figure 2.2.2: Saipem Castoro XI specifications

2.3 Modeling - Results

2.3.1 Case A0 - One free barge & Case A1 - Two free barges

The one free barge *Case A0*, is the simplest of all analyses carried out in this framework and is the basis for all comparisons and assumptions made in this section. The single barge will be solved both for radiation and diffraction potentials in infinite waterdepth for 57 discrete wave periods ranging from $3.0[s] - 30[s]$ and 19 wave headings $(0 - 270^o)$ for all 6 rigid body modes. The barge geometry is given explicitly as input to Wamit through proper FORTRAN subroutine. The desired output shall be the hydrodynamic radiation added mass and damping coefficients, the hydrodynamic scatter (incoming & diffracted) loads, the hydrostatic stiffness and the barge motion/force RAO. Finally, bodies COG coordinates, free/fixed modes definition, full mass matrix and external mass, stiffness damping matrices are added in the force input file (*.frc). The heave, roll and pitch RAO are plotted in post processing and produce smooth curves fully corresponding to a free barge behavior in waves.

Case A1 is based on A0 and the only change implemented is the incorporation of a second barge with the exact same geometry and inertia properties at a horizontal distance of $65[m]$ to the original barge. The heave response in 90° wave direction is slightly distorted due to wave scattering and shielding effects when compared to the single barge case but naturally the amplitude profile remain in the same range of magnitude. The distortion due to the same cause is also visible in the pitch response in quartering seas (especially 60°). The response magnitude change significantly in the roll degree of freedom, proving the vessels increased sensitivity to the respective DOF. Hydrodynamic coupling enhance roll peak response in beam waves by more than 30% although the vessels distance is rather high but naturally does not shift the vessels fundamental roll period.
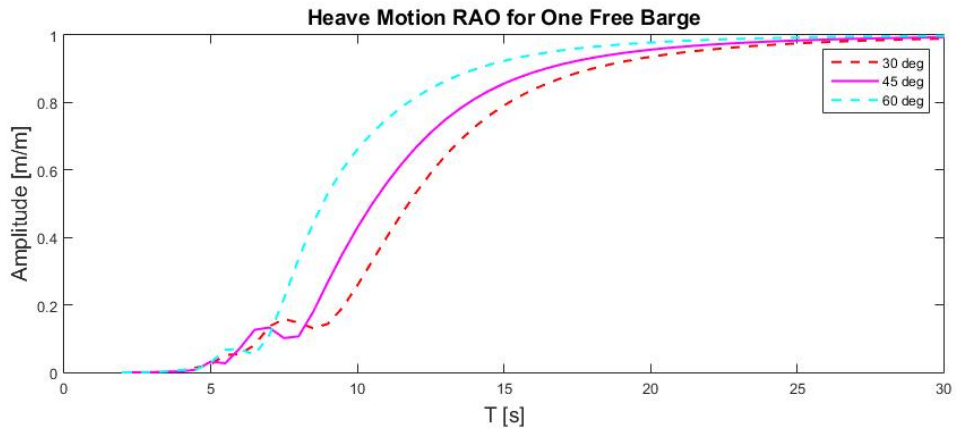
(a) Heave RAO for single barge
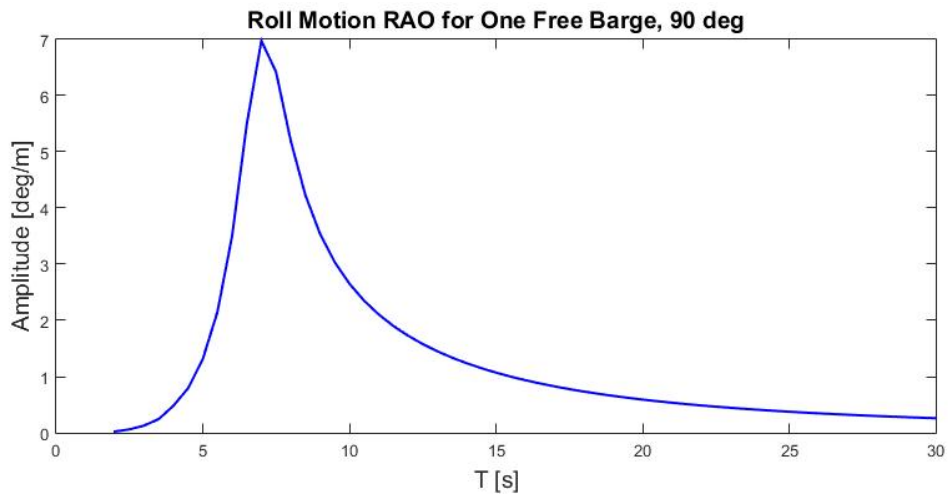
(b) Roll RAO for single barge
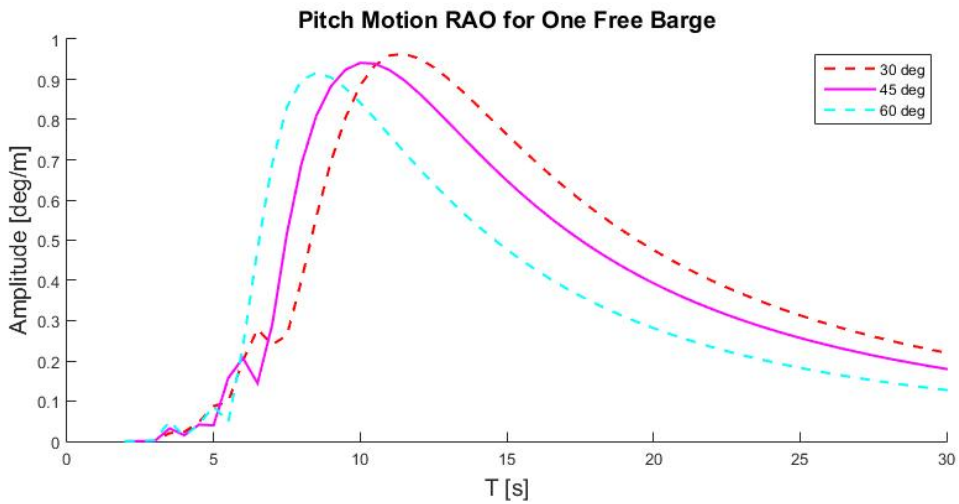
(c) Pitch RAO for single barge

Figure 2.3.1: Heave, roll & pitch RAO for single barge - Case A0
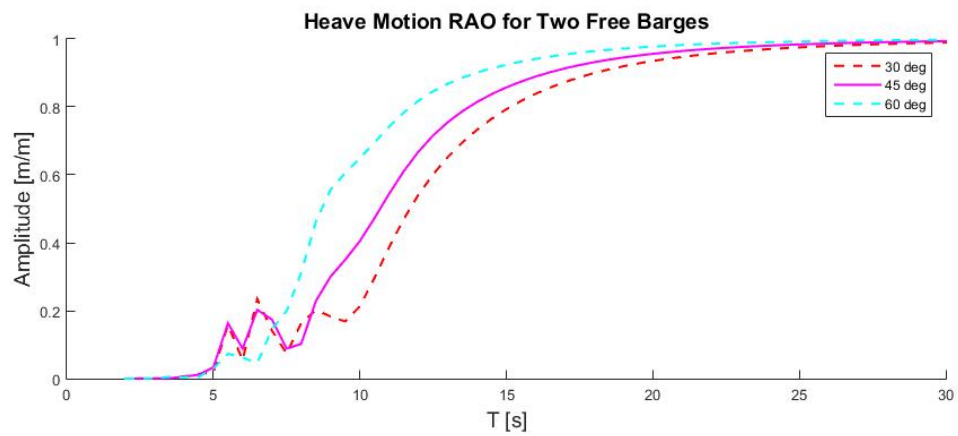
(a) Heave RAO for two barges
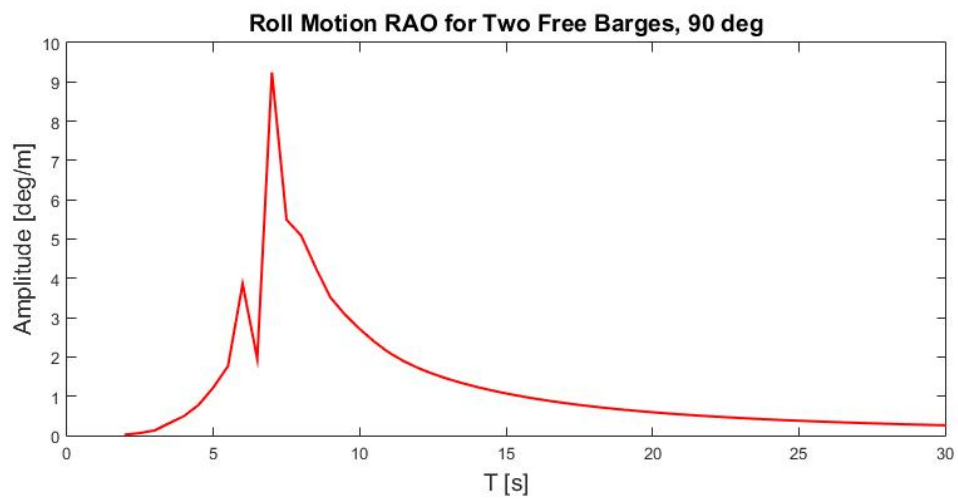
(b) Roll RAO for two barges
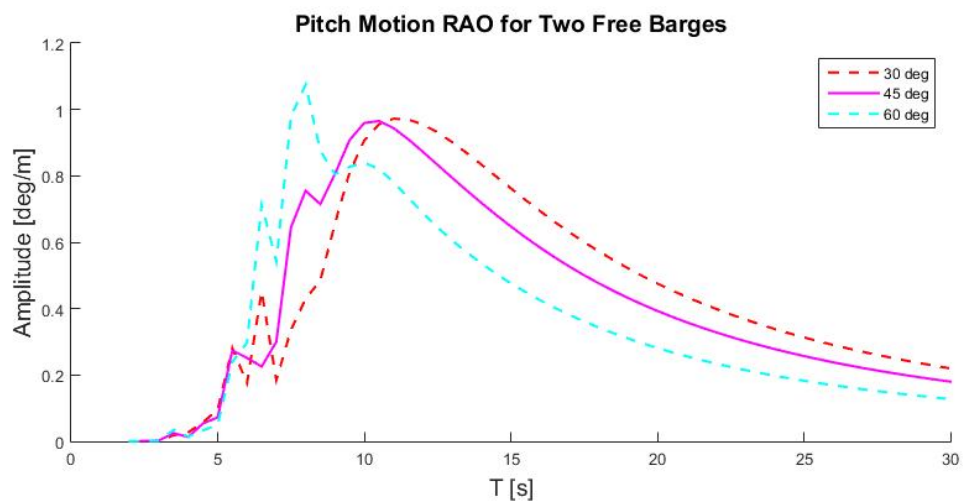
(c) Pitch RAO for two barges

Figure 2.3.2: Heave, roll & pitch RAO for two barges - Case A1

It is true that the A1-multibody roll response in beam waves is presenting a few discrepancies (discontinuities that result in narrow peaks) that is explained as follows: the irregularities in the roll amplitude are explained by the sway, roll and yaw phase profiles which are coupled according to the following equation of motion:

$$a_{42}\ddot{y} + c_{42}\dot{y} + k_{42}y + (I_{xx} + a_{44})\ddot{\varphi} + c_{44}\dot{\varphi} + k_{44}\varphi + (-I_{xz} + a_{46})\ddot{\psi} + c_{46}\dot{\psi} + k_{46}\psi = X_{w4} \quad (2.3.1)$$

The phase profile for all 3 degrees of freedom keep a constant trend in high period band $(T > 12[s])$ while significant phase fluctuations are observed in the wave period band $(T = 5 - 9[s])$, fully reasoning the phenomenon.
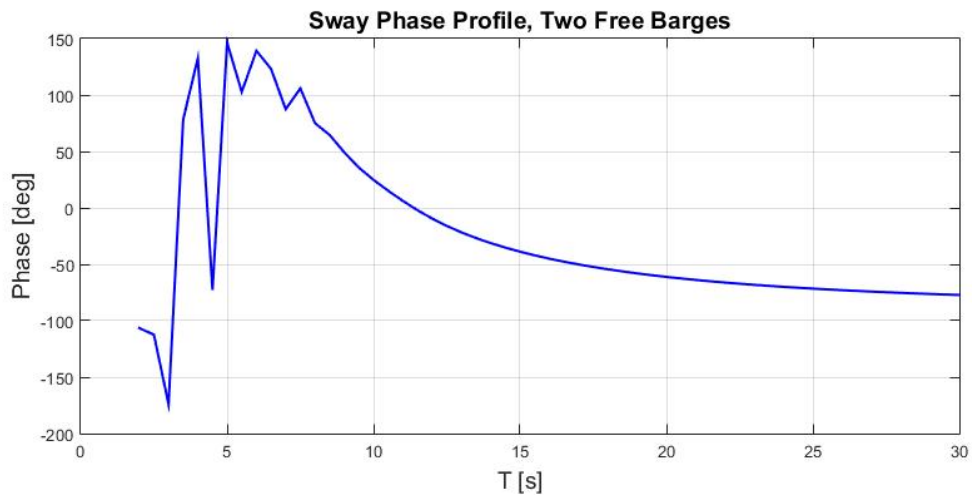
(a) Sway phase profile
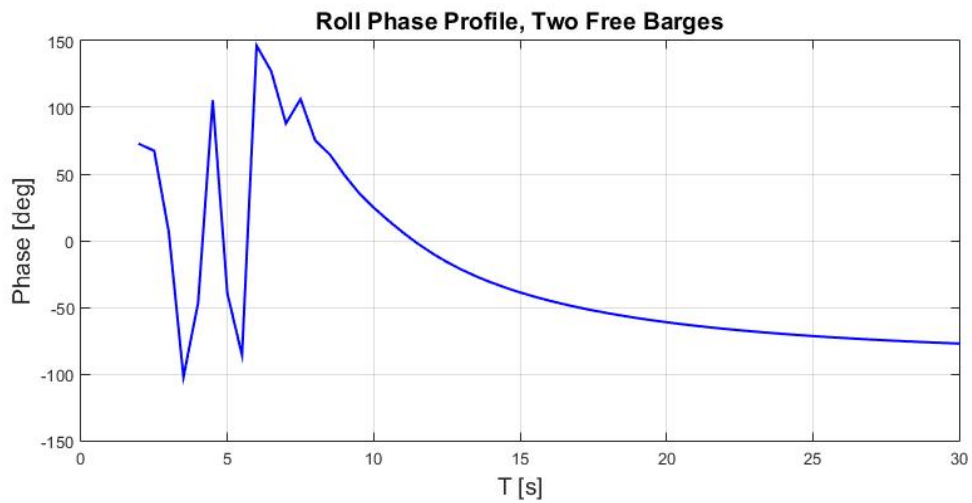
(b) Roll phase profile
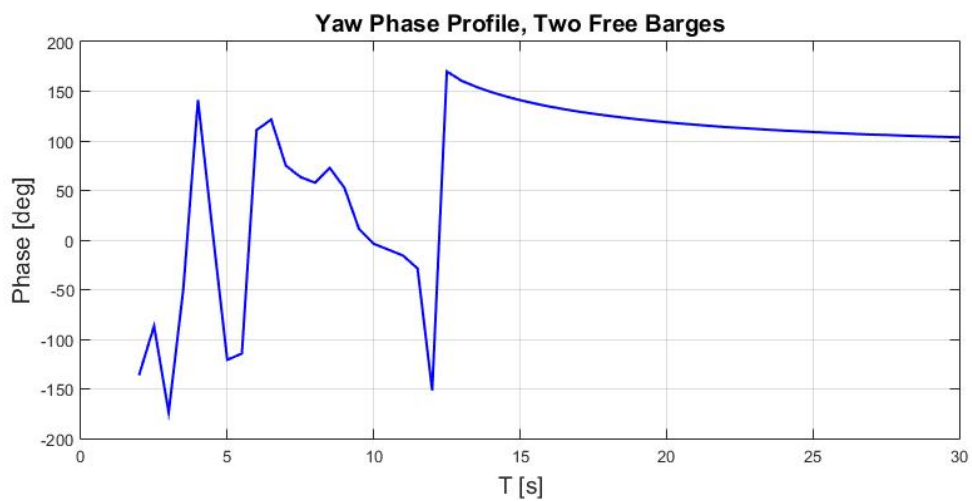
(c) Yaw phase profile

Figure 2.3.3: Sway, roll & yaw phase profiles in two free barges roll RAO in beam waves

2.3.2   Case A2 - Catamaran barge & Case A3 - constrained barges

In *Case A2* both barges hull characteristics remain the same, therefore the system waterplane area and inertia properties are identical which in turn translates to the same results for the radiation component of the problem. However, that is not the case in the scatter problem; the two hulls are clamped with a plate structure on top. As a result, the catamaran roll response is greatly improved peaking at $1.10[deg/m]$, merely 10% of the A1 response in the same spectra ($9.24[deg/m]$) in the wave period range and the peak response ($1.37[deg/m]$) is shifted to lower periods $T_{roll(A2)} = 4[s]$ and out of the wave frequency band $T_z = 5 - 9[s]$. This improved roll motion behavior however comes at the expense of higher hydrodynamic loads which require the linking mechanism to be much stiffer, making the configuration less mobile and less feasible. This argument is further elaborated in the coming subsection.

As for the heave response, a low-period spike in beam waves is encountered, a resonant-like behavior due to the wave trapping in the gap between the catamaran hulls. Sun et al. (2010), explained the phenomena for first-order analysis of resonant free surface responses in gap between adjacent barges, coming to the conclusion that the resonances experienced in low periods are only visible in beam waves since they correspond to a standing wave mode that is antisymmetric across the gap and therefore cannot be excited in the symmetric case of head seas. This mode is causing unrealistic RAO results in lower periods and this numerical divergence can be dealt with the use of a free surface damper lid in the horizontal distance between the barges [refer to section A.5;Pauw et al. (2007); Newman (2004)].Furthermore, at a wave period of $T_z = 11[s]$, a near-zero motion response is encountered both in heave and pitch for the catamaran at a 60° wave angle of attack which is best described as the discrete wave period where the near-zero excitation is encountered. The phenomenon is elaborated for the case of pontoon design for semi-submersible structures [Newman and Lee (1999)]. The same phenomenon is also described in literature as cancellation frequency near-resonance.
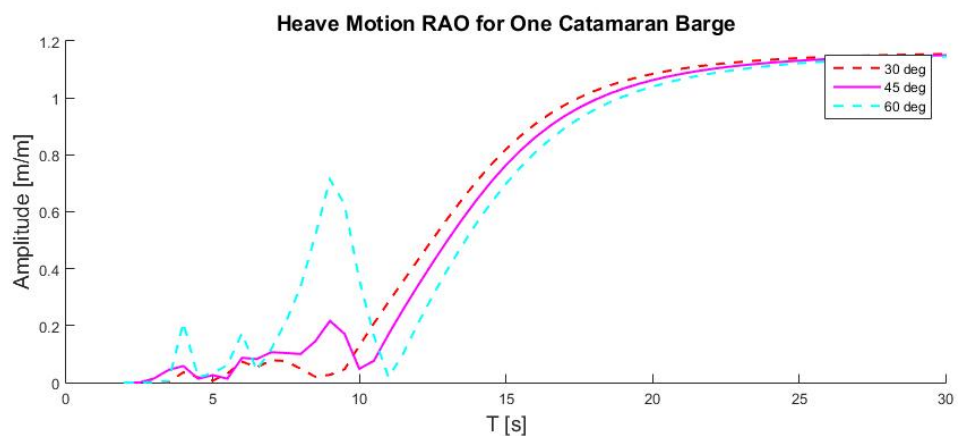
(a) Heave RAO for catamaran barge
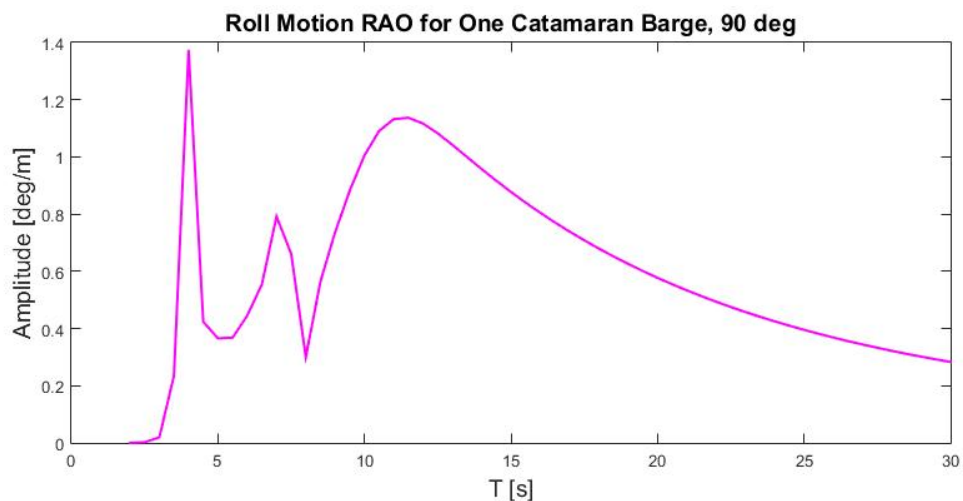
(b) Roll RAO for catamaran barge
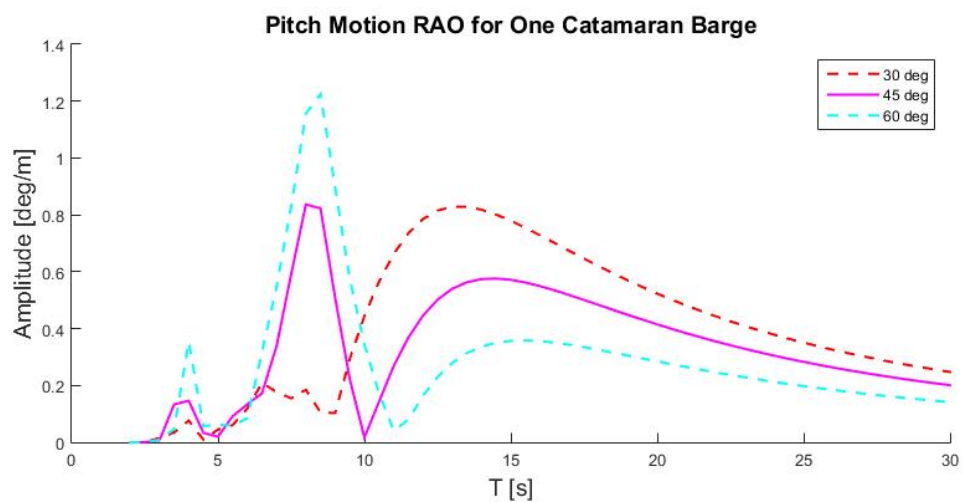
(c) Pitch RAO for catamaran barge

Figure 2.3.4: Heave, roll and pitch RAO for catamaran barge - Case A2

The modeling scope for the constrained barges - *Case A3* is to initiate the creation of an external stiffness matrix which will represent the stiffness added by the link mechanism to the system. However, the need for absolute coupling of barges in all horizontal motions (surge, sway & yaw) and roll indicates that the user shall impose identical motions to the respective DOF or, to be more precise, t*he differential motion of barges in these DOF shall converge to zero.* The stiffness values in the diagonal and off-diagonal terms are thus needed to be sufficiently close to infinity for the following constraint equation to be met

$$k_\infty \frac{d(x_{i,i} - x_{i,i+6})}{d\omega} = 0, .. for : i = 1, 2, 4, 6 \tag{2.3.2}$$

The k_∞ value has no physical representation and is merely a way to impose kinematic link constraints in Wamit but it shall correspond (be proportional) to a stiffness value characteristic of the system. The stiffness matrix built-up will be performed step by step by triggering a stiffness value proportional to the hydrostatic stiffness in the vertical direction $k_{z,hyd}$ in every DOF separately, starting with roll and moving on to the horizontal motions. This proportionality is dictated by a magnification factor n defined by the user. The model is solved for the prescribed external stiffness, e.g. in the roll DOF, and the user has to validate whether the RAO amplitude and phase of both vessels matches completely. Only then the infinite stiffness implementation would be valid; identical response for both barges in a certain stiffened DOF depicts that there is no differential motion in the respective degree of motion and therefore the (theoretically) k_∞ does suffice.
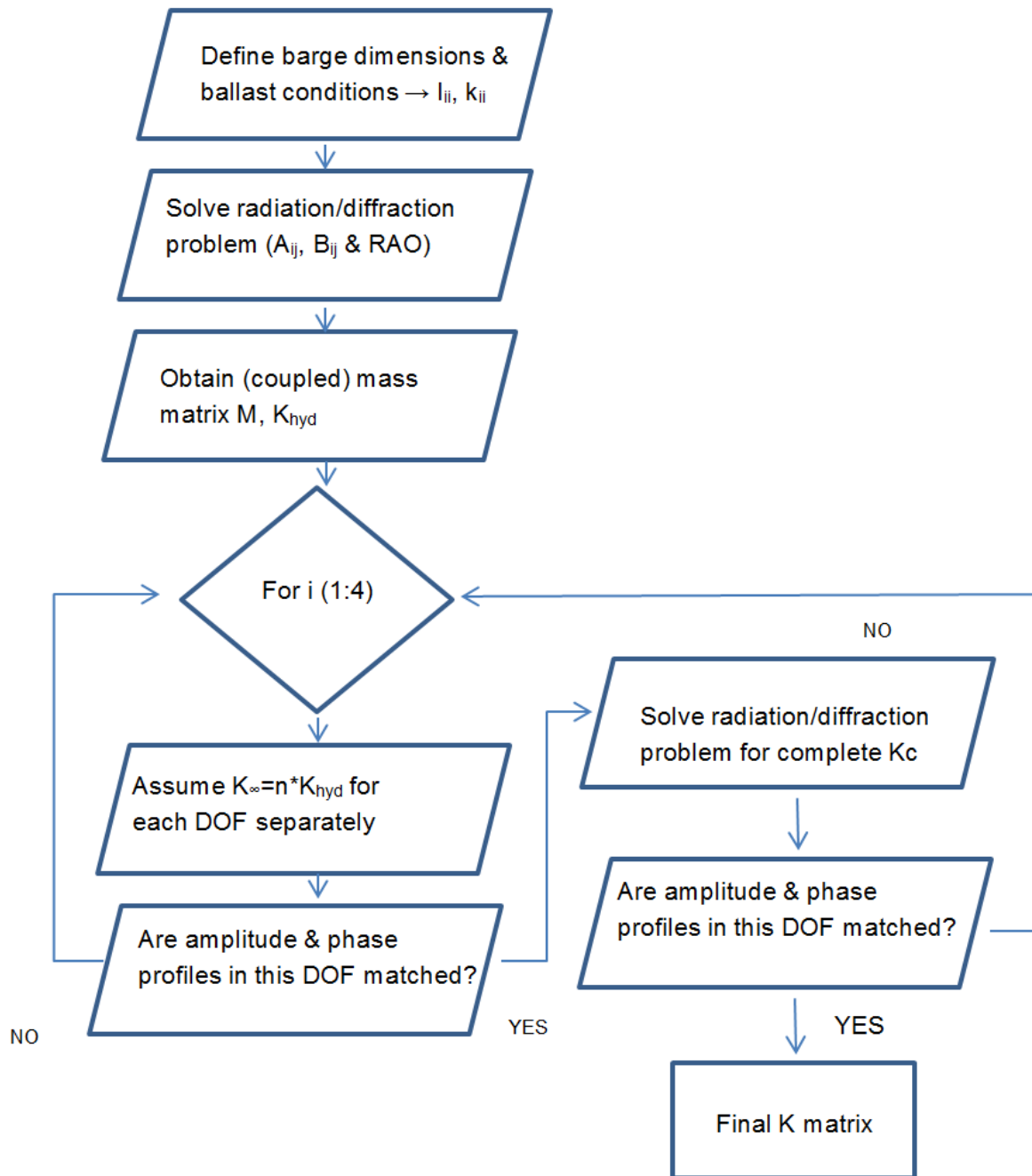
Figure 2.3.5: Process flow chart

The final built-up for the pseudo 12x12 system (8 lines are identical and can subsequently be deducted to 4 in the final system of equations) should look like the matrix tabulated in figure 2.3.6:

$$\begin{pmatrix}
n_1 k^\infty & 0 & 0 & 0 & 0 & n_1 k^\infty \frac{b}{2} & -n_1 k^\infty & 0 & 0 & 0 & 0 & n_1 k^\infty \frac{b}{2} \\
0 & n_1 k^\infty & 0 & 0 & 0 & 0 & 0 & -n_1 k^\infty & 0 & 0 & 0 & 0 \\
0 & 0 & k_z & 0 & k_{z\theta} & 0 & 0 & 0 & -k_z & 0 & -k_{z\theta} & 0 \\
0 & 0 & 0 & n_1 k^\infty \frac{b^2}{4} & 0 & 0 & 0 & 0 & 0 & -n_1 k^\infty \frac{b^2}{4} & 0 & 0 \\
0 & 0 & k_{\theta z} & 0 & k_\theta & 0 & 0 & 0 & -k_{\theta z} & 0 & -k_\theta & 0 \\
n_1 k^\infty \frac{b}{2} & 0 & 0 & 0 & 0 & n_2 k^\infty \frac{b^2}{4} & n_1 k^\infty \frac{b}{2} & 0 & 0 & 0 & 0 & -n_2 k^\infty \frac{b^2}{4} \\
-n_1 k^\infty & 0 & 0 & 0 & 0 & n_1 k^\infty \frac{b}{2} & n_1 k^\infty & 0 & 0 & 0 & 0 & n_1 k^\infty \frac{b}{2} \\
0 & -n_1 k^\infty & 0 & 0 & 0 & 0 & 0 & n_1 k^\infty & 0 & 0 & 0 & 0 \\
0 & 0 & -k_z & 0 & -k_{z\theta} & 0 & 0 & 0 & k_z & 0 & k_{z\theta} & 0 \\
0 & 0 & 0 & -n_1 k^\infty \frac{b^2}{4} & 0 & 0 & 0 & 0 & 0 & n_1 k^\infty \frac{b^2}{4} & 0 & 0 \\
0 & 0 & -k_{\theta z} & 0 & -k_\theta & 0 & 0 & 0 & k_{\theta z} & 0 & k_\theta & 0 \\
n_1 k^\infty \frac{b}{2} & 0 & 0 & 0 & 0 & -n_2 k^\infty \frac{b^2}{4} & n_1 k^\infty \frac{b}{2} & 0 & 0 & 0 & 0 & n_2 k^\infty \frac{b^2}{4}
\end{pmatrix}$$

Figure 2.3.6: Global stiffness matrix assembly

The heave and pitch diagonal terms and their respective inter- and intra- couplings are tabulated with a red color since they represent the barges-link stiffness. The first value assigned to the magnification factor is $n = 10$, a solution which was immediately dismissed since the RAO match in surge/sway/yaw was not possible. However, the roll profiles were matching ($\varphi_1 = \varphi_2$) for $k_{roll} = 1.65e + 12 [N/m]$. This is a first indication that the surge/yaw stiffness terms need to be further magnified. Through iterations, the final value was decided to be $n = 1000$ which corresponds to a $k_\infty = 6e + 10 [N/m]$. For that value of infinite stiffness, it is also confirmed that the complete match of surge, sway and yaw responses are identical ($x_1 = x_2$, $y_1 = y_2$, $\psi_1 = \psi_2$). All discrete stiffness terms are superimposed to a full matrix where once again a RAO match in all DOF should occur simultaneously. However, the results for surge and yaw and its coupling terms were showing a small discrepancy. The linear equation that stands by applying a unitary displacement $x_i = 1$ (displacement method) is the following:

$$k_\infty [(x_1 - x_2) + \frac{b}{2}(\psi_1 + \psi_2)] = 0$$

However in principle:

$$\psi_1 = \psi_2$$

At this stage the further magnification of the yaw stiffness was iteratively determined at $k_{\psi\psi} = 1.65e + 16 [N/m]$, which provided a perfect match both in amplitude and phase.

2.3.3 General Case Studies Postprocessing

The A3 constrained case study was carried out considering that the asymmetric hydrodynamic roll moments exerted on barges should ideally cancel out each other by imposing proper kinematic constraint in roll degree of freedom (k_∞ principle in Wamit framework). Moreover, differential heave and pitch is expected to be also reduced and could be further treated with proper feedback motion control (mass-spring-dashpot mechanism) in passive fashion. The roll motion and force RAO for all cases are shown below and vividly depict the differences in response for the different case studies:

- The single barge case (A0-blue line) is responding in a smooth manner for all degrees of freedom;

- Two free barges case (A1-red line) is experiencing minor distortions in roll in the wave frequency range due to phase shifts in sway, roll and yaw degrees of freedom caused by the wave diffraction effect while the roll peak response occurs in the same period ($T_{roll(A0)} = T_{roll(A1)} = 7[s]$) and for 30% higher amplitude as in the single barge case;

- The catamaran case (A2-purple line) is excited at 10% in roll compared to the one free barge case, exhibiting close to zero motion response at a certain cancellation frequency in heave and pitch degrees of freedom. This motion performance is highly desirable and exhibits the necessity for mechanical roll synchronization of barges;

- In stiffened barges (A3-green line) the roll peak response (5.03 deg/m -45% lower than in two free barges) occurs at the same fundamental period ($T_{roll(A3)} = T_{roll(A2)} = 4[s]$) as the catamaran barge which validates that the holonomic constraint was successfully implemented in Wamit. In such manner, by synchronizing the roll DOF, the fundamental roll period is shifted out of the wave period range, eliminating the resonant behavior of the configuration due to the wave effect. Additionally, this structural property is achieved by designing a less stiff mechanism which in turn experiences less hydrodynamic loading as one can see visualized in the force RAO plots. Thus, the stiffened configuration combine the free barges flexibility and the catamaran motion performance in roll making this solution technically optimized and feasible.
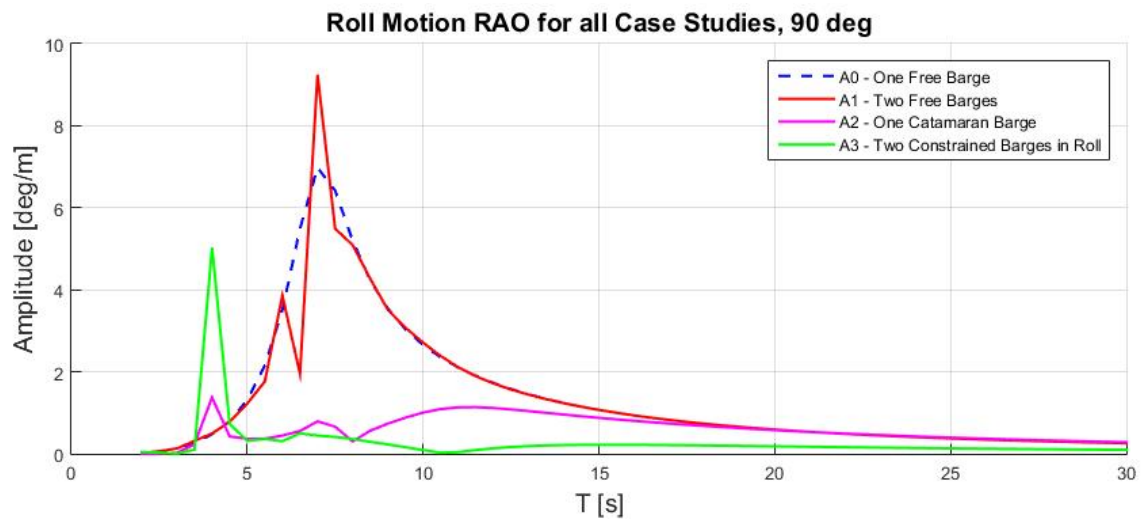
Figure 2.3.7: Motion roll RAO
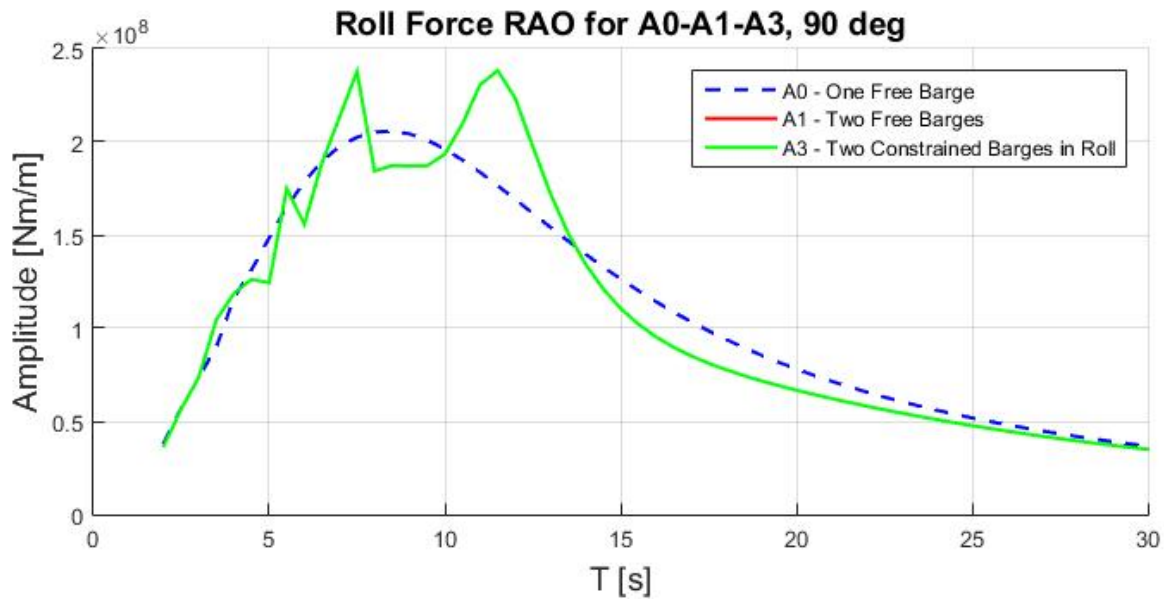
(a) Force Roll RAO for one single barge (A0),two free (A1) and two coupled (A3) barges
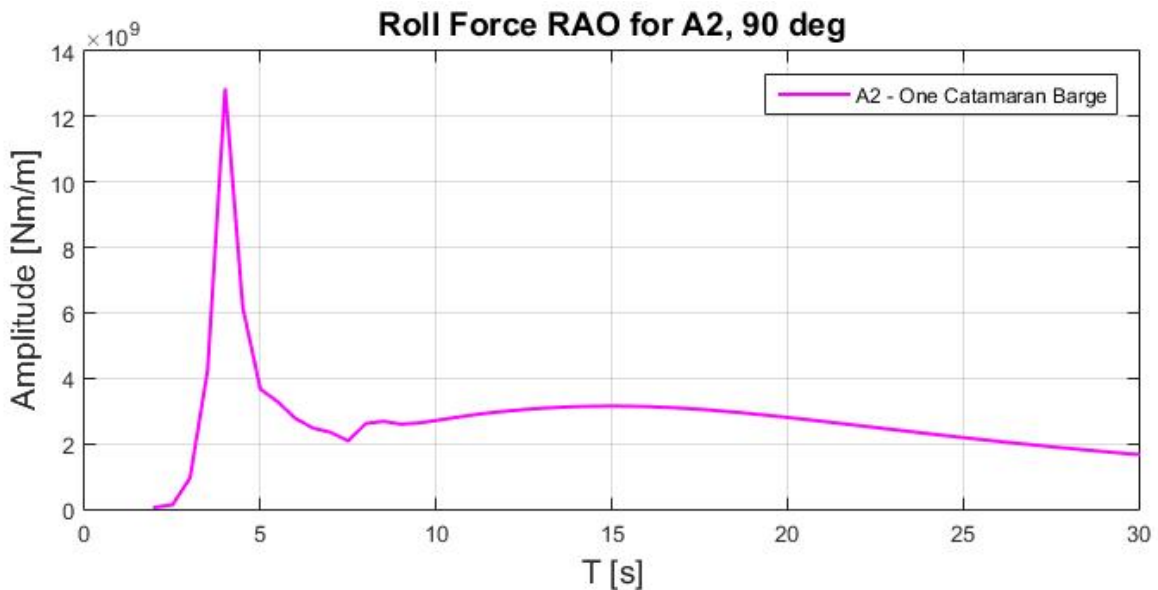
(b) Force roll RAO for catamaran (A2) barge

Figure 2.3.8: Force roll RAO for all cases (beam waves)

As for the heave and pitch, identical comparison plots for all models were made. The catamaran structure (purple line) is again having near-zero cancellation periods ($T_c = 11$[s] in both degrees of freedom) but it is obvious that within the wave frequency band of interest, the attenuation of motions compared to the other cases is not that significant than in roll DOF. Surprisingly, the constrained barge (A3-green line) is having a lower pitch peak response compared to the catamaran. These plots validate that by constraining the barges in heave and pitch degrees of freedom not much (if any) value is added to the ultimate goal of improved motion performance while on the

other hand making the link mechanism more cost ineffective (more steel) and less mobile.
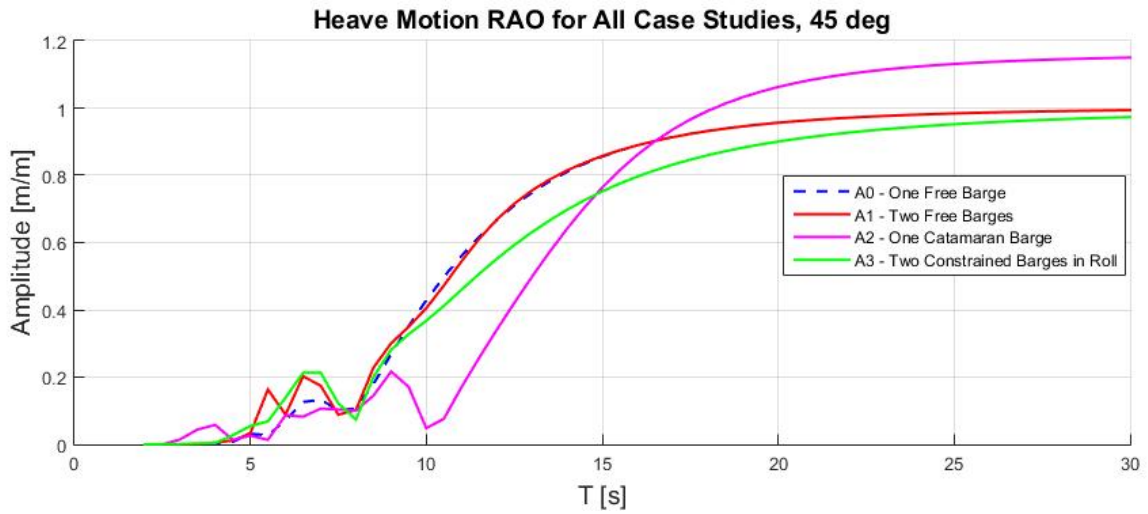
(a) Heave Motion RAO
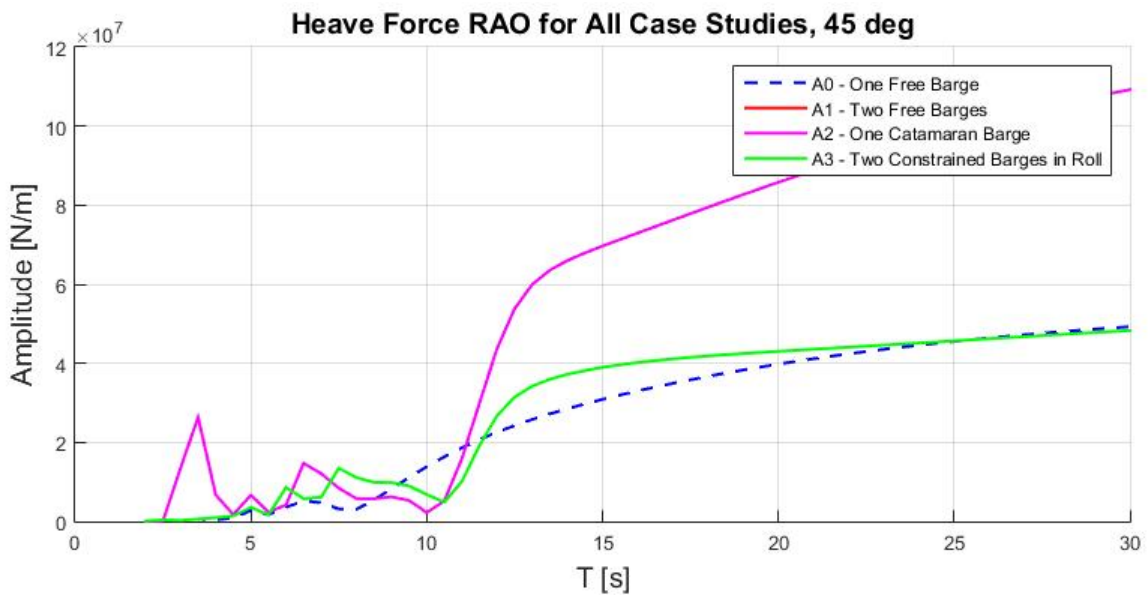
(b) Heave Force RAO

Figure 2.3.9: Heave motion/force RAO for all case studies (45° of wave direction)
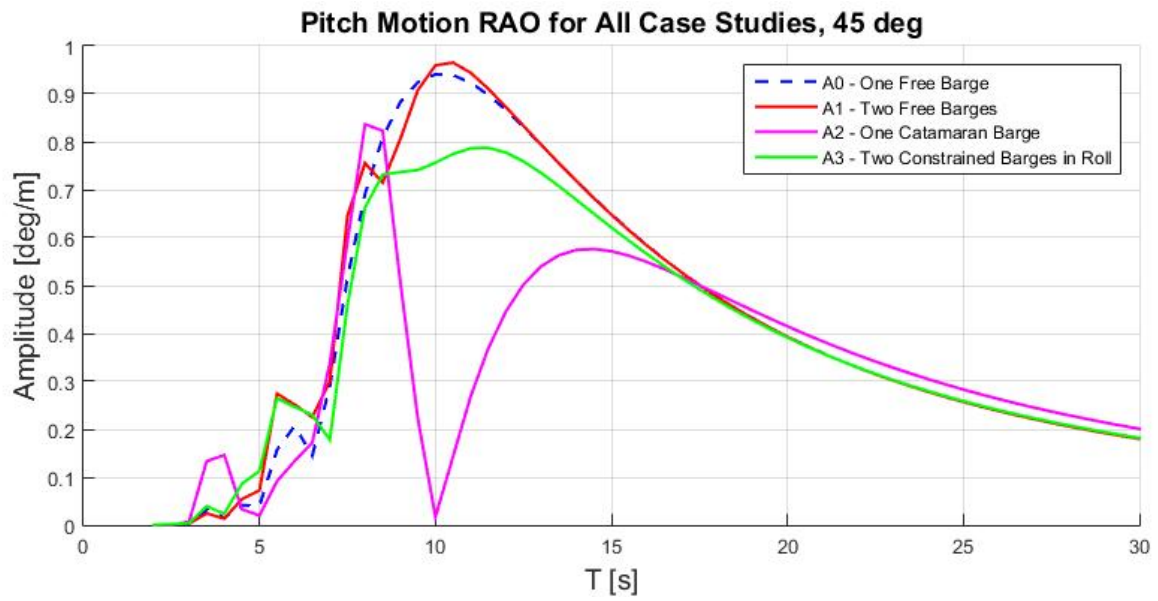
(a) Pitch Motion RAO
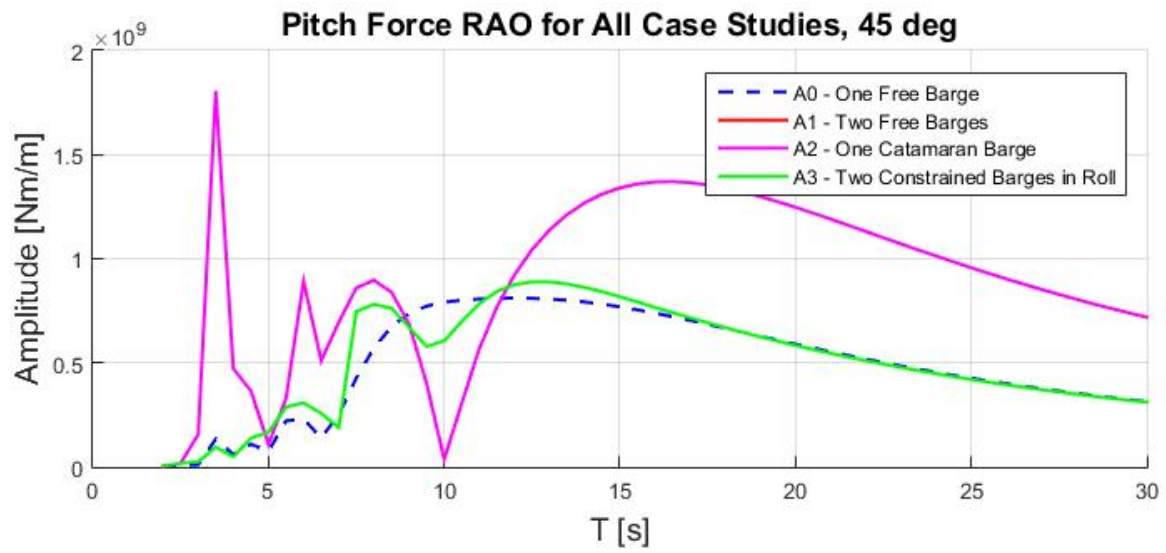
(b) Pitch Force RAO

Figure 2.3.10: Pitch motion/force RAO for all cases (45°of wave direction)

Remark One has to analyze the numerical output of 3D radiation-diffraction solver with care and caution. As already pointed out in section A.5, the undamped free surface of a linear (viscous damping-free) model responds in a non-physical manner in certain eigenfrequencies refered as *irregular frequencies* in related literature (Journèe and Massie (2001)). Leakage of the effect of these irregular frequencies to its neighbouring frequency band is occuring due to the body panel discretization; effective methods to reduce the effects of irregular frequencies are extensively reported in the aforementioned section A.5. In this exercise, these irregular frequencies are 'taken out' of the velocity potential and source strength direct calculation with a simultaneous automatic free surface discretization.

A representative example of the irregular frequency effect is given herein. First, the multibody simulations were carried out without taking the irregular frequency effect into consideration. The results for a moderate distance in between vessels were indeed worrying but the researcher's full trust into the (already proved) solver was the reason for trying to physically explain a non-physical flow which was simply a modeling error due to the linear assumptions taken (no viscous damping considered). In an effort to validate the irregular frequencies effect to the numerical output the following has been done: the roll RAO of a multibody model of vessels extremely distanced to each other (260 m) where the hydrodynamic coupling shall be minimal to non-existent, was compared to a single body roll RAO. The resulting transfer functions should be identical but the following profile was produced tabulating graphically the irregular frequencies effect.
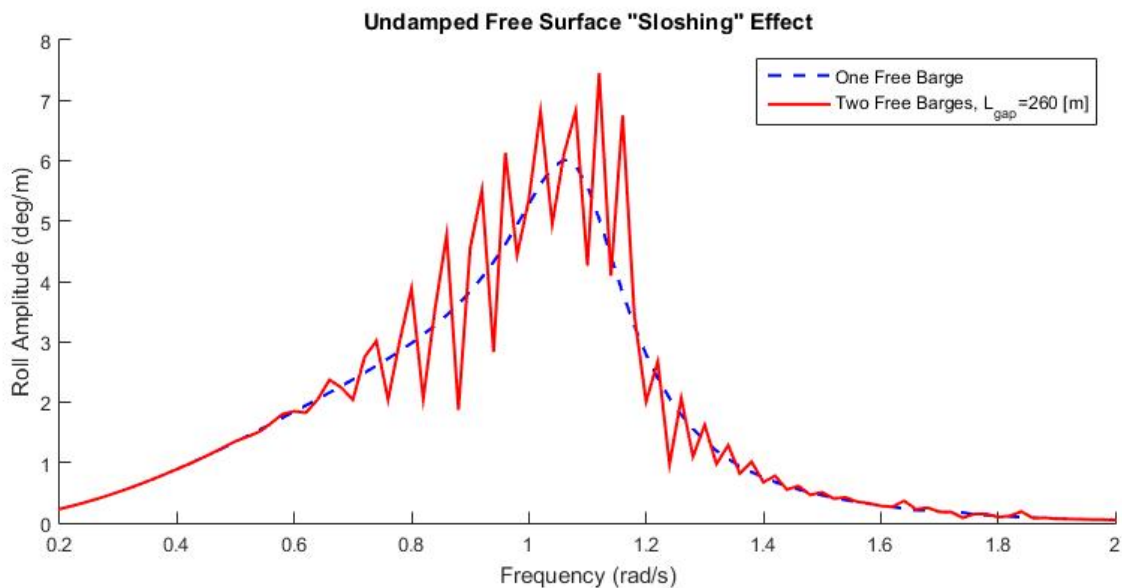
Figure 2.3.11: Irregular frequencies effect

That note is merely a reference to future research on the multibody hydrodynamic interactions where a more sophisticated (damping 'lid') approach in irregular frequencies treatment is recommended (refer to section A.5).

2.4 MOP Hydro Summary

In order for the hydrodynamic assessment of MOP final configuration to be made, motion/force response analyses were carried out for 3 different case studies. The main design parameters which will shape the assessment process were presented; then the unique geometries and external mass/stiffness properties were given as input to the 3D radiation-diffraction linear solver for the hydrodynamic added mass and damping coefficients plus the scatter forces to be determined. More specifically:

- One free barge (A0);

- Two free barges (A1), only hydrodynamically coupled;

- One catamaran barge (A2);

- Two mechanically coupled barges (A3), roll synchronization;

After postprocessing the RAO results the following conclusions are drawn:

- Even though the distance between barges is assumed to be rather high $(65m)$ when compared to the barges dimension in the transverse direction $(40m)$, the hydrodynamic coupling in beam waves (90°) in roll degree of freedom is significant (approx.30% higher response). However, this is not the case for heave and pitch degrees of freedom;

- Implementing motion synchronization in roll, the motion peak is attenuated by 45% while shifting to lower periods and outside the wave period range, excluding the possibility of resonant behavior of the configuration. Furthermore, the use of transparent rigid 3D frame makes the configuration less stiff and more mobile when compared to the 100% monolithic concept of the catamaran, resulting in lower hydrodynamic loading in roll. Finally, one can see in fig. 2.3.8 that roll hydrodynamic loading is independent of the kinematic constraint (comparing two free barges to two stiffened barges) while the catamaran force RAO peak in roll can be up to 2 orders of magnitude higher.

- Heave and pitch hydrodynamic loading is of the same order of magnitude irrespective of the configuration, showing that the, lower in magnitude but of equal importance, differential heave and pitch motions shall be mitigated by an alternative approach.

Chapter 3

MOP Motion Optimization

In the system description so far, station in surge, sway and yaw degrees of freedom are treated via the constraints employed in the first stage of the numerical frequency domain simulation, while the link contribution to the system is provided solely through a kinematic constraint to the roll degree of freedom, reducing in total the system order from a 12 to 8 rigid-body DOF. Referring back to fig. 2.3.6, the heave and pitch stiffness diagonal terms and their respective inter- and intra-couplings highlighted in red are deliberately left blank in the hydrodynamic analysis. The solution investigated in this thesis is the implementation of a passive spring-damper H_∞ controller which bounds the differential motions in the aforementioned DOF by minimizing the generalized plant (structural model interacting with waves and external mooring forces) transfer function. The theoretical background covered for the scope of this exercise is summarized in Appendix B, mainly stimulated by the excellent textbooks of Aström and Murray (2010); Skogestad and Postlethwaite (2007); Zhou et al. (1996); Perez (2006); its implementation to the concept-specific applications are based to the work of Grigoriadis and Skelton (1998); Camino et al. (2003); van Solingen et al. (2014); Burke et al. (2006); Apkarian et al. (2014) and can be found in section B.3.

In a quick preview, the hydrodynamic coefficients (added mass $A(\omega)$ and damping $B(\omega)$) and the scatter RAO component for the case with the two constrained barges were utilized to identify the radiation and scatter state-space model of the wave effect which excites the closed-loop system consisting of the structural model interconnected with the passive H_∞ controller which is affine to tunable static parameter θ. *The scope herein is to verify that under the current model formulation, the passive control definition and optimization would attenuate the system steady-state response in heave, roll and pitch to a minimal level.* This can be investigated via a "grid search" for parameter θ which is upon optimization under the criteria given in equations 3.0.1, 3.0.2. Parameter θ is a non-negative scalar and its optimization shall be investigated within a discrete space. The case

studies that will be simulated and presented in this Chapter are stated below:

- Preliminary case study: In an effort to get familiarized with the suggested methodology by Camino and Apkarian, an elementary case was elaborated for solving an integrated control and structure problem in the non-convex, non-smooth optimization framework. The case consists of the structural parameter optimization of a 3-storey building under earthquake excitation, resembling physically to the task on hand. Another argument for that case study to be documented is the verification of the numerical results obtained in comparison to the simulation on the same structural model by Camino on his seminal paper.

- Final case study: Two coupled barges are synchronized in roll via holonomic kinematic constraint, while link frame stiffness and damping parameters in heave and pitch degrees of freedom are optimized for a prescribed system performance γ; the structural parameters upper bounds will be defined by the user in two different approaches as explained in section 3.3. The link structural parameters K_s and C_s are extracted from the generalized plant and become part of a block diagonal controller, a process which can be done by employing LFT techniques (refer to B.4). This block diagonal controller is optimized via the minimization of the transfer function T_{zw} by determining static, constrained controller K

$$min_K \left\| T_{wz} \right\|_\infty < \gamma \tag{3.0.1}$$

The notation T_{zw} expresses the transfer function mapping between the exogenous input and output and is used as a minimization criteria in MIMO control design. Alternatively, a mixed-sensitivity S/KS synthesis design approach is pursued, which is comprised of finding an admissible controller K which stabilizes the plant and minimizes the infinite norm of the following cost functions

$$min_K \left\| \begin{matrix} W_p S \\ W_u KS \end{matrix} \right\| < \gamma \tag{3.0.2}$$

Findings of both approaches will be documented and compared in terms of optimization downtime and system performance. Ultimately, structural and control system design are integrated in the same analysis aiming for the derivation of jointly optimal workable solution spaces.

(a) Final Case Study: Roll Sync (0% Load Transfer)   (b) Final Case Study: Topside Coupling (100% Load Transfer)
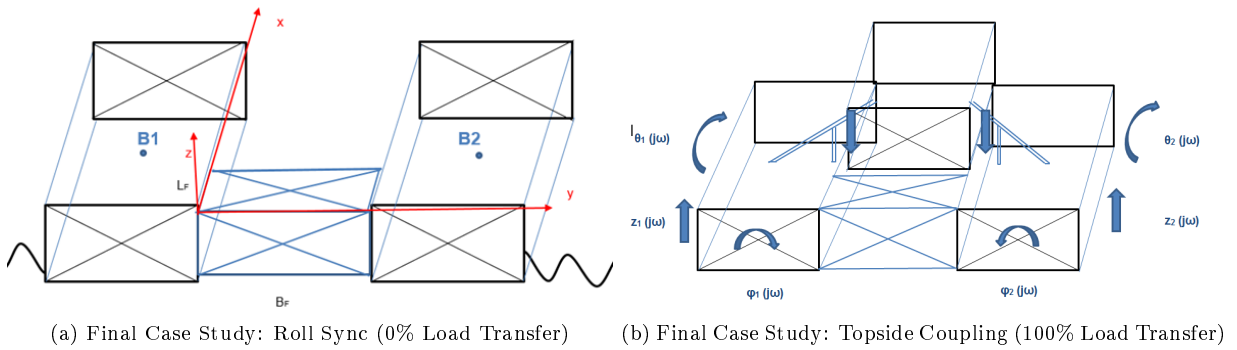
Figure 3.0.1: Conceptual Case Study

3.1 Camino Benchmark Case Validation

This case study is elaborated as an engineering exercise on the joint control and structural parameters optimization and in order to get familiarized with the essential commands of MATLAB Robust Control Toolbox [Gu (2005),Gahinet and Apkarian (2011)], namely the parametrization command `realp`, the plant-controller interconnection command `lft`, the H_∞ synthesis command `hinfstruct` which allows the user to optimize multiple fixed-order, fixed structure, centralized MIMO controllers through an iterative algorithm based entirely on the bilinear matrix inequality framework [Apkarian and Noll (2006)] e.t.c. The method allows the mass, damping and stiffness matrices to be freely parameterized while the terms within the aforementioned matrices are bounded in a realistic manner. The integrated structure and control design is shown to be equivalent to a decentralized (block diagonal) feedback control problem [Camino et al. (2003)] which consists of the interconnection of the generalized plant (determined by the equations of motion expressed in state space form) and the fixed-structure controller. The design process is then a two step approach; a nominal structure is defined with all its parameters free (or some of them, a choice subject to the optimization criteria posed by the researcher); then the structure and the controller which is affine to the structure properties are jointly optimized in iterative fashion according to H_∞ minimization (sub-optimal control).

Problem Statement   The system considered in this case study is a 3-storey building modeled by equal masses connected by spring-dampers to each other and the soil which is excited by a generalized disturbing force $f(t)$. One can clearly see the similarities between this case study to the general problem treated in this thesis; in a geometry sense the case study is about 3 masses connected in series while the final case study is about 3 masses connected in a triangle. As for the external disturbance, the excitation simulates an earthquake since this is a structural design model having the same effect as the hydrodynamic forces exerted on the barges in the final case study.
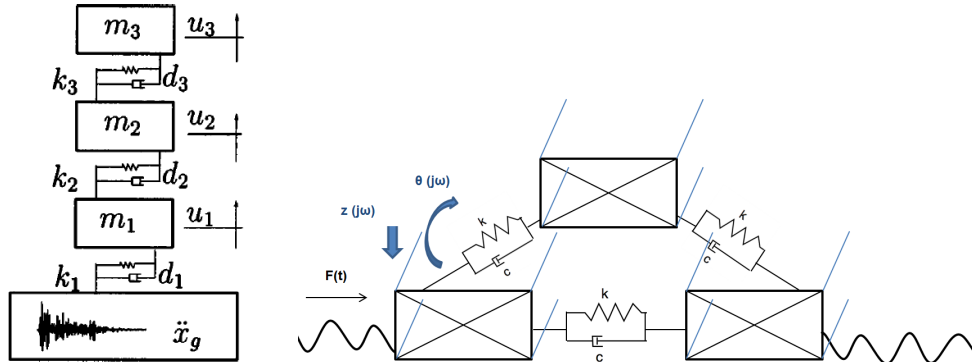
Figure 3.1.1: Example & Final Case Study Arrangements

The equation of motion for the system described would be:

$$M\ddot{q} + D\dot{q} + Sq = f(t) \tag{3.1.1}$$

where $q\epsilon\mathbb{R}^\nu$ the vector of the system generalized displacements and velocities; $M, D, S \in \mathbb{R}^{\nu\times\nu}$ the mass,damping and stiffness matrices respectively. The external force $f(t)$ shall be decomposed to the control input and the disturbance input actuating the system

$$f(t) = \tilde{B}_u u(t) + \tilde{B}_w w(t) \tag{3.1.2}$$

where the control signal is the system unknown to be determined and the exogenous disturbance is a white noise process. Changing the system representation in state space by introducing state vector $x = [q, \dot{q}]$,

$$\begin{bmatrix} I & 0 \\ 0 & M \end{bmatrix} \dot{x} = \begin{bmatrix} 0 & I \\ -S & -D \end{bmatrix} x + \begin{bmatrix} 0 \\ \tilde{B}_u \end{bmatrix} u + \begin{bmatrix} 0 \\ \tilde{B}_w \end{bmatrix} w \tag{3.1.3}$$

$$E\dot{x} = Ax + B_u u + B_w w \tag{3.1.4}$$

The building block of this approach shall be that all parameters (mass,damping & stiffness) are freely parameterized within certain bounds defined by the researcher. In this example all parameter upper and lower bounds are 2.0 and 0.5 of the nominal values presented in Table 3.1.2. Therefore, all system parameters have an affine representation

$$M(\eta) = M_0 + \sum_s \eta_s M_s \ , \ D(\beta) = D_0 + \sum_j \beta_j D_j \tag{3.1.5}$$

$$S(\gamma) = S_0 + \sum_k \gamma_k S_k \tag{3.1.6}$$

Introducing structural parameter $a\epsilon\mathbb{R}$ which contains the parameters above leaving the control input $u(t)$ to be independent, then the descriptor equation 3.1.4 becomes

$$E(a)\dot{x} = A(a)x + B_u u + B_w(a)w \tag{3.1.7}$$

Finally, the output nominal performance C_0 is defined and now the full plant P in state space form is complete (for simplicity matrix D assumed to be zero). The optimization problem consists in finding a fixed-structure 2-by-2 controller K such that the infinite norm of the forward mapping T_{wz} is minimized.

Example Illustration The nominal structural parameters for the system presented in Table 3.1.2, assuming $\tilde{B}_u = I$, $\tilde{B}_w = (m_1, m_2, m_3)^T$ and the disturbance exogenous input to be a white noise process with intensity $W = 16[m^2/s^4]$.

Floor Masses [Kg]	Damping [kN s/m]	Stiffness [kN/m]
m1=5,897	d1=67	k1=33,732
m2=5,897	d2=58	k2=29,093
m3=5,897	d3=57	k3=28,621

Figure 3.1.2: Nominal Structural Parameters

Solving the system shown in left side of figure 3.1.1, the mass matrix is block diagonal $M = diag(m_1, m_2, m_3)$ and the damping, stiffness matrices are given

$$D = \begin{bmatrix} d_1 + d_2 & -d_2 & 0 \\ -d_2 & d_2 + d_3 & -d_3 \\ 0 & -d_3 & d_3 \end{bmatrix} \; ; \; S = \begin{bmatrix} k_1 + k_2 & -k_2 & 0 \\ -k_2 & k_2 + k_3 & -k_3 \\ 0 & -k_3 & k_3 \end{bmatrix} \qquad (3.1.8)$$

The output vector C is given

$$C = \begin{bmatrix} 1 & 0 & 0 & 0 & 0 & 0 \\ -1 & 1 & 0 & 0 & 0 & 0 \\ 0 & -1 & 1 & 0 & 0 & 0 \\ 0 & 0 & 0 & 1 & 0 & 0 \\ 0 & 0 & 0 & -1 & 1 & 0 \\ 0 & 0 & 0 & 0 & -1 & 1 \end{bmatrix} \qquad (3.1.9)$$

1. Optimization of k_2, d_2 In the first example considered, the only parameters to be optimized are the stiffness and damping coefficients for the second floor. By simulating it with the script made for the cause, a peak infinite norm of $\|T_{wz}\|_\infty = 1.66$ is reached after 91 iterations. The structural parameter a equals to 3.0388 and the structural parameters under consideration have reached their upper threshold values ($k_2 = 58186 \, [kN/m]$, $d_2 = 116 \, [kN \, s/m]$). The second order controller is determined to be

$$K_1 = \frac{10009s^2 - 1.46s + 31540}{s^2 + 1.67s + 5.81 * 10^{-8}}$$

2. Optimization of all 9 nominal parameters Finally, all 9 structural parameters are set free within the subset defined above. After 117 iterations a peak norm of $\|T_{wz}\|_\infty = 1.65$ is reached and the parameter a equals to 51.0877. All 9 parameters reach the upper maxima bound (2 times the nominal value) and the second order controller along with the closed-loop transfer function bode plot

$$K_3 = \frac{17620s^2 - 21570s + 29900}{s^2 + 1.61s - 9.47 * 10^{-8}}$$

Conslusively, the theoretical basis of the methodology as introduced by Grigoriadis and further elaborated by Camino has been successfully implimated in Matlab scripting, whose end product is validated by reproducing the case study of mass, stiffness and damping properties optimization of a 3-storey building, the same study that was carried out in the seminal paper. The example also demonstrates the advantage of simultaneous controller and strucural design; by bounding the desired dynamic response of the structure via a control optimization method, the system performs (sub)optimally even without the use of active control elements.
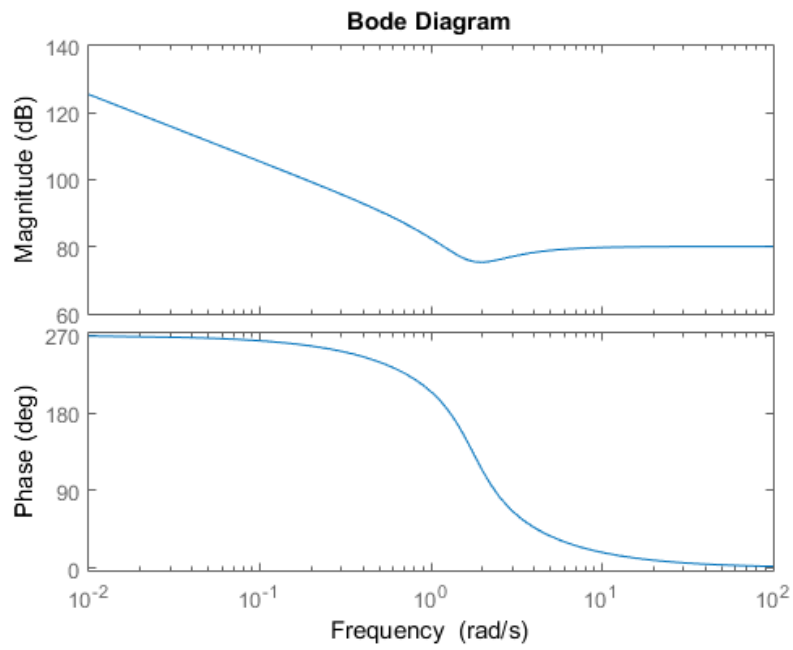
(a) Controller 1 Bode Plot
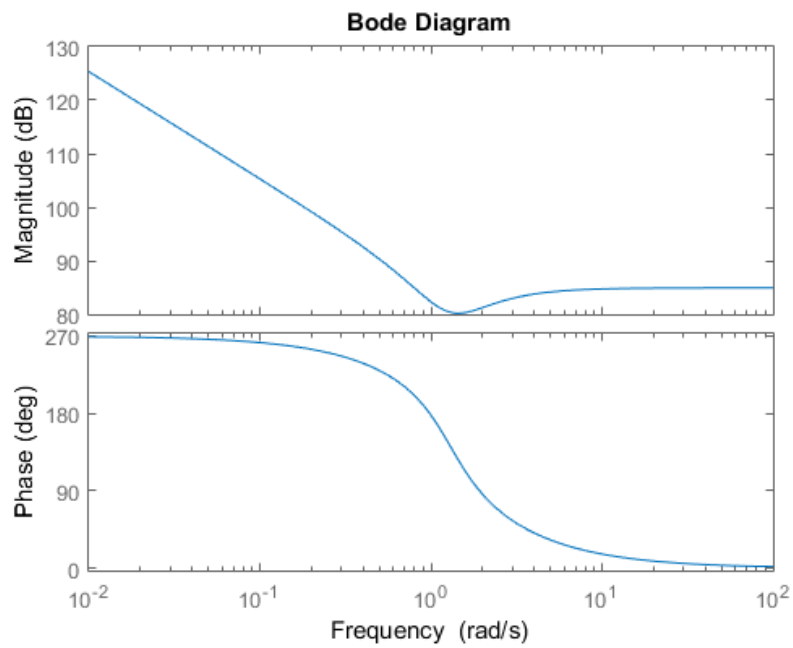
(b) Controller 2 Bode Plot

3.2   System Formulation & Structured H_∞ Synthesis in Matlab

In this section, the case study closed-loop dynamics formulated in mathematical and block diagram form (fig. 3.2.1) and modeled accordingly in MATLAB workspace will be presented.
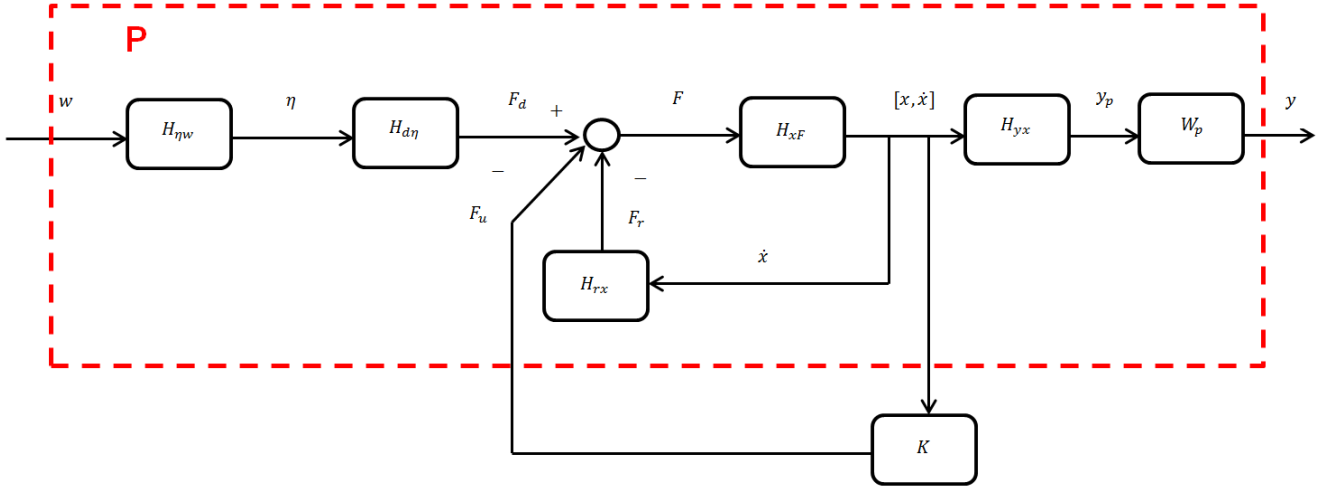
Figure 3.2.1: System in block diagram form

The plant structure will be as follows: the reference input is a white noise signal which excites a wave (JONSWAP) spectrum filter, giving the wave elevation corresponding to the seastate at hand as output (for this case study the analysis is carried out for the seastate $H_s = 3.0[m], T_z = 9[s]$). The wave elevation process $\eta(j\omega)$ excites the diffraction filter which provides the diffraction force vector (the wave force component due to the incoming wave meeting the water piercing body surface), which in turn stimulates the mechanically coupled barges. The barges displacement and velocity output signal $[x, \dot{x}]$ switches on the radiation filter and the controller (link structural stiffness and damping parameters). In more detail, the generalized plant-controller system definition is comprised of the following tasks:

3.2.1   System States Definition

Definition of the system state variables at the barges COG (hydrodynamic reference frame h) and the full system COG (platform reference frame). The output feedback controller design aims at the optimization of the link frame structural properties therefore both state system displacements and velocities are of interest. The two barges heave and pitch degrees of freedom plus the synchronized roll are adequately describing the full barges-link-platform model. The barges state vector with respect to the platform-barges frame yx is now updated to:

$$x = (z_1, \theta_1, z_2, \theta_2, \varphi)^T \tag{3.2.1}$$

The platform in turn will experience a vertical lift plus a roll rotation around x-axis (due to barges roll and differential heave) and a pitch rotation (average and differential pitch). Now

the corresponding platform output state vector can also be defined with its parameters directly correlated to the barges states:

$$y = (z, \rho, \theta, \chi, \varphi)^T \tag{3.2.2}$$

lift: $z = \frac{1}{2}\frac{(z_1+z_2)}{l_p}$ (average heave, normalized)

bank: $\rho = \frac{z_1-z_2}{l_p}$ (differential heave, normalized)

tilt: $\theta = \frac{1}{2}(\theta_1 + \theta_2)$ (average pitch)

flip: $\chi = \theta_1 - \theta_2$ (differential pitch)

roll: φ (synchronized roll)

Lift and bank are normalized by the distance l_p between the two barges COG. The transformation from barges-to-platform frame of reference relation can also be expressed in matrix form:

$$y = H_{yx}x \tag{3.2.3}$$

$$H_{yx} = \begin{bmatrix} \frac{1}{2}l_p^{-1} & 0 & \frac{1}{2}l_p^{-1} & 0 & 0 \\ l_p^{-1} & 0 & -l_p^{-1} & 0 & 0 \\ 0 & \frac{1}{2} & 0 & \frac{1}{2} & 0 \\ 0 & 1 & 0 & -1 & 0 \\ 0 & 0 & 0 & 0 & 1 \end{bmatrix} \tag{3.2.4}$$

3.2.2 Wave Elevation Process

Definition and identification of the elevation process $\eta(j\omega)$ which will be the system's exogenous input. This wave elevation function $\eta(j\omega)$ will be derived by white noise filtering, the filter being a state-space identification of the JONSWAP spectrum (refer to section A.2) as follows:

$$H_{\eta w} = \left(\frac{z}{cz^2 + 2bz + 1}\right)^4; \quad \begin{matrix} c = 1.121 \\ b = -0.458 \end{matrix} \quad [Jansen, 2015]$$

$$\dot{s} = A_{nw}s + B_{nw}w \tag{3.2.5}$$

$$\eta = C_{nw}s + D_{nw}w \tag{3.2.6}$$

3.2.3 Radiation and Diffraction Filter Subspace Identification

State-space identification of the radiation H_{rx} and diffraction $H_{d\eta}$ problem via subspace system identification method (refer to section A.6 and equations A.6.8-A.6.11,A.6.12-A.6.14;Wang (2015)) and the necessary model reduction with balanced residualization techniques (refer to subsection A.7). The need for exquisite subspace identification state space model accuracy in the works of Wang, resulted in the maximum use of the convex optimization solver capacity which can identify up to 24 internal states per degree of freedom, leading to high order systems even for models of moderate complexity. In this case, only 6 degrees of freedom are of interest (heave-roll-pitch for a 2-body model) leading to a hydrodynamic model of 265 internal states in total (121 describing the diffraction hydr. force dynamics and 144 for the radiation force dynamics). The scope is therefore to reduce the model state count without accuracy loss. The balanced residualization explained in sub.A.7 results in the model reduction by 186 states as shown in the figure below
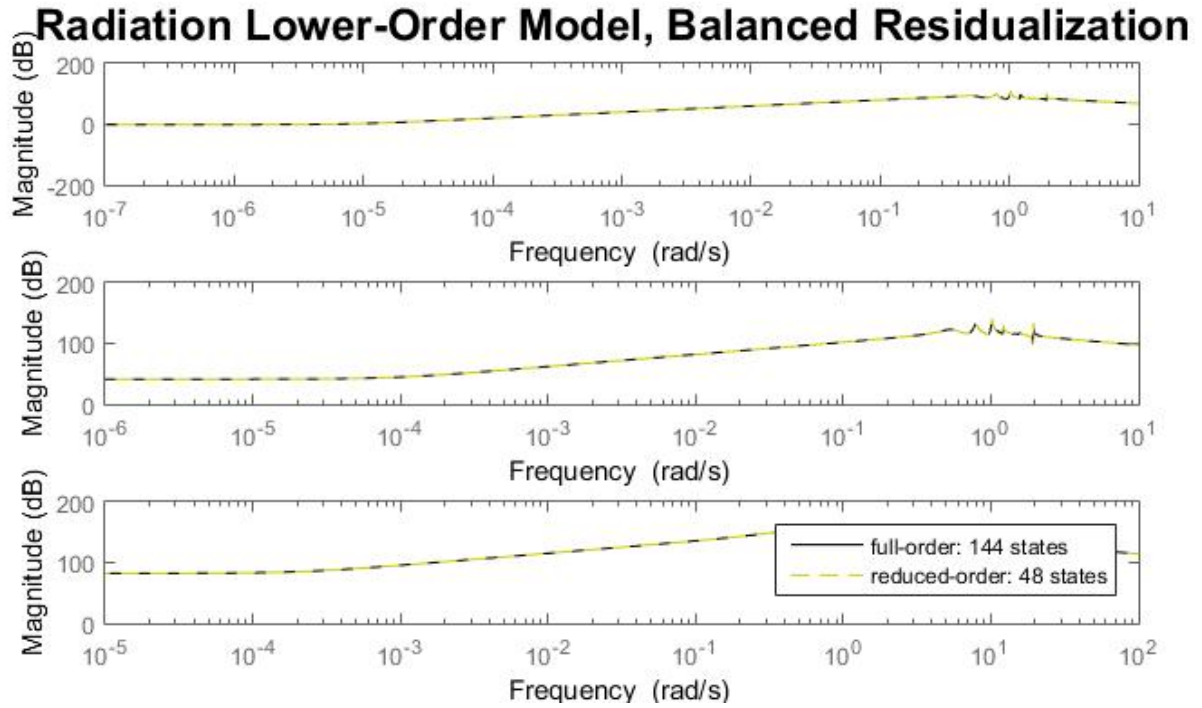
(a) Radiation model order reduction
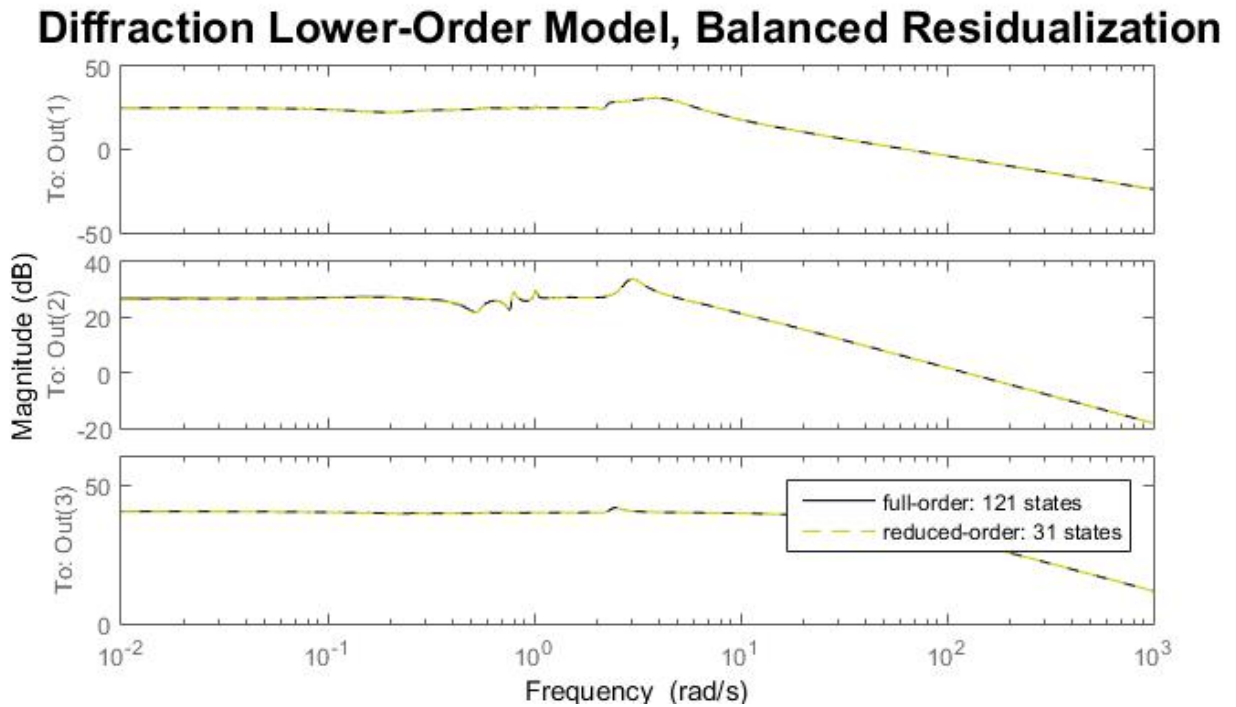
(b) Diffraction model order reduction

Figure 3.2.2: Model reduction via balanced residualization methods

3.2.4   Barges Second Order System

Formulation of the barge structural transfer function H_{xF}, which receives the total hydrodynamic force as input and provide the barge state variables (displacements and velocities) as output. The barge equation of motion requires the derivation of the full mass and stiffness matrix analytically and the expression of the set of equations in state space form. In this case study, the barge hydrostatic stiffness is already a given through numerical solver Wamit therefore only the analytical derivation of the mass matrix is required. Since the h-frame is inertial, the barge vector equation of motion in this frame will be Perez (2006):

$$M^h \ddot{\xi} = \tau^h_{hyd} \qquad\qquad (3.2.7)$$

The matrix M^h is the generalized rigid-body matrix with respect to the hydrodynamic frame and has been expressed in equation A.4.5. Finally, the second order system H_{xF} in state space form:

$$\dot{x} = \begin{bmatrix} 0 & I \\ -K^h/M^h & -C^h/M^h \end{bmatrix} x + \begin{bmatrix} 0 \\ I/M^h \end{bmatrix} F_r + \begin{bmatrix} 0 \\ I/M^h \end{bmatrix} F_d \qquad (3.2.8)$$

where the hydrostatic stiffness K^h and full mass matrix are non-zero terms already determined while the damping matrix C^h is zero, describing the internal barge dynamics. The radiation and diffraction wave forces will be fed as input to the barge state space model. The model outputs are the barge displacements and velocities. The heave-roll hydrostatic coupling is shown in the figure below where the barge frequency response functions for the heave, roll and pitch degrees of freedom have been plotted.
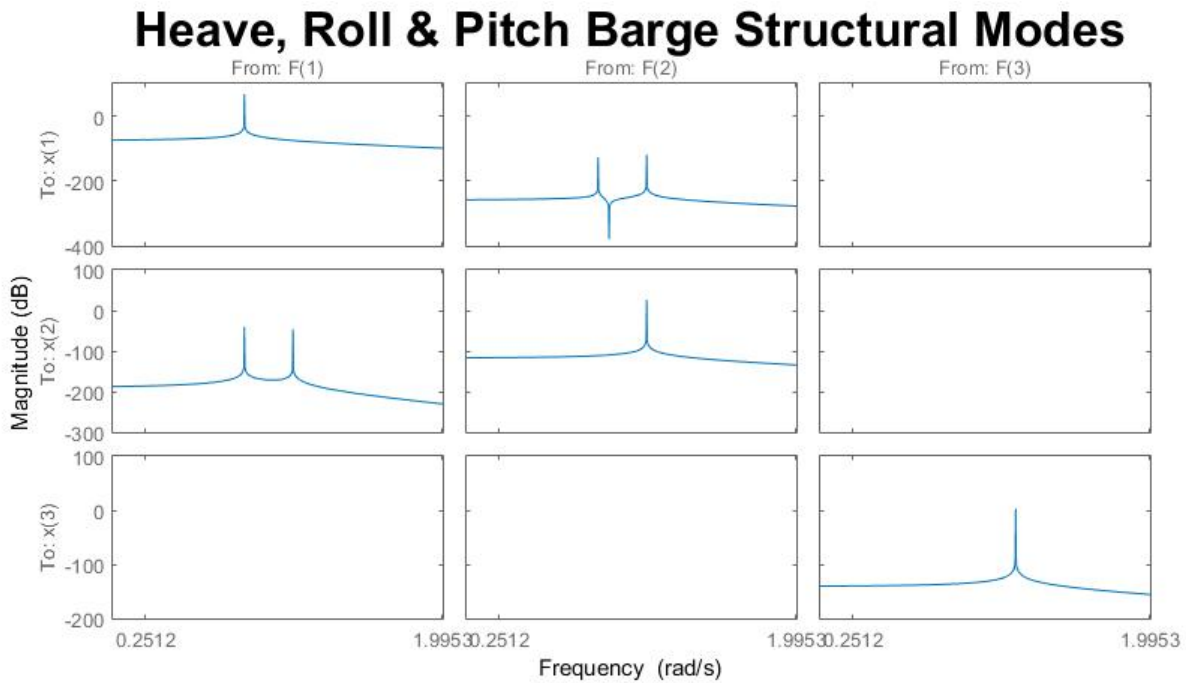
Figure 3.2.3: Heave, roll and pitch structural modes for 1 barge

3.2.5 Controller K Definition

Define diagonal controller K. The non-negative stiffness and damping terms of the link positioned in between the barges are extracted from the generalized equations of motion and become elements of a decentralized, static, fixed-structured controller K. Depending on the engineering scope of the optimization, the decision on which parameters are about to be free/fixed in the optimization process is determined. Heave, roll and pitch are the DOF of interest for the scope of this control simulation therefore the 2-body structural model is a set of 6 ODE equations. However, the stiffness and damping terms of the link need to be explicitly expressed in the K matrix making it a 12$ \times $12. The roll synchronization has already been modeled in the hydrodynamic part of the analysis as a holonomic kinematic constraint and the synchronous roll motion is proven to be significantly attenuated ($1[deg/m]$ on contrast to the roll motion for the mechanically uncoupled barges that reaches a resonant response of $9[deg/m]$ in the wave band of interest - $T_z = 5 - 9[s]$). Therefore, it is chosen to keep the link roll stiffness and damping terms out of the optimization and thus fixed. However, the heave-roll motion coupling dictates that the new, optimized system would attenuate the differential heave motion which in turn result in a respective attenuation of the roll motion. The 'strength' of this coupling will be depicted by the roll peak response attenuation in the frequency response plots of the closed-loop transfer function $PK(j\omega)$.

Furthermore, the parameter values need to be bounded so to be within the scale of the system's physical quantities; i.e the maximum link stiffness values will be determined with respect to the hydrostatic stiffness of one barge in the corresponding degree of freedom and the maximum link damping will be shaped by using the logarithmic decrement method for the barge-radiation model inteconnected system. This method is used so to measure the damping ratio for linear underdamped models like the radiation filter identified for the scope of this reasearch. The decay response in time can be casted in the form of

$$x(t) = X exp(-\zeta \omega_n t) sin(\omega_d t + \varphi) \tag{3.2.9}$$

where X is the amplitude in $[m]$, $\zeta = \frac{c}{2\sqrt{km}}$ is the damping ratio, $\omega_d = \omega_n \sqrt{1 - \zeta^2}$ is the damped frequency and finally φ is the phase angle of the damped oscillations. The logarithmic decrement δ is merely the logarithmic ratio of any two successive peaks of the time domain system transient response due to initial conditions defined by the user

$$\delta = \frac{1}{n} ln\left(\frac{x(t)}{x(t + nT)}\right), \ n : integer \ of \ successive \ peaks \tag{3.2.10}$$

and the damping ratio can thus be calculated by the formula:

$$\zeta = \frac{1}{\sqrt{1 + \left(\frac{2\pi}{\delta}\right)^2}} \tag{3.2.11}$$

Free vibrations in the barges heave and pitch degrees of freedom were carried out under the following initial conditions:

- Heave: $z_0 = 1[m], \dot{z}_0 = 0[m/s]$
- Pitch: $\theta_0 = 1[deg], \dot{\theta}_0 = 0[deg/s]$

The transient response under the effect of the initial displacement and rotation is presented in the figure below. The damping ratio calculated via the equations 3.2.10-3.2.11 is $\zeta_{heave} = 0.9\%$; $\zeta_{pitch} = 2.4\%$ resulting in damping values of $c_{heave} = 2.15E6[Nm/s]$ and $c_{pitch} = 7.01E9[Nrad/s]$, respectively.
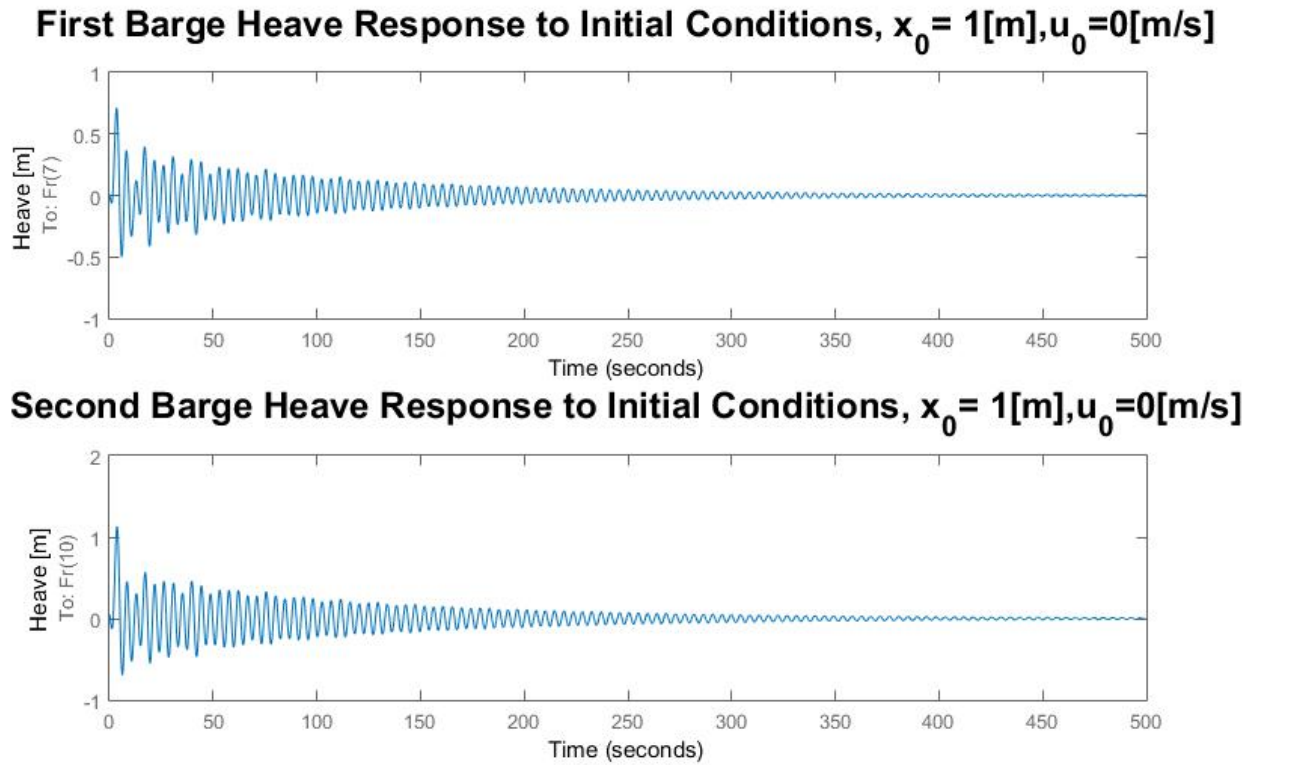
(a) Heave response to initial conditions $z_0 = 1[m], \dot{z}_0 = 0[m/s]$
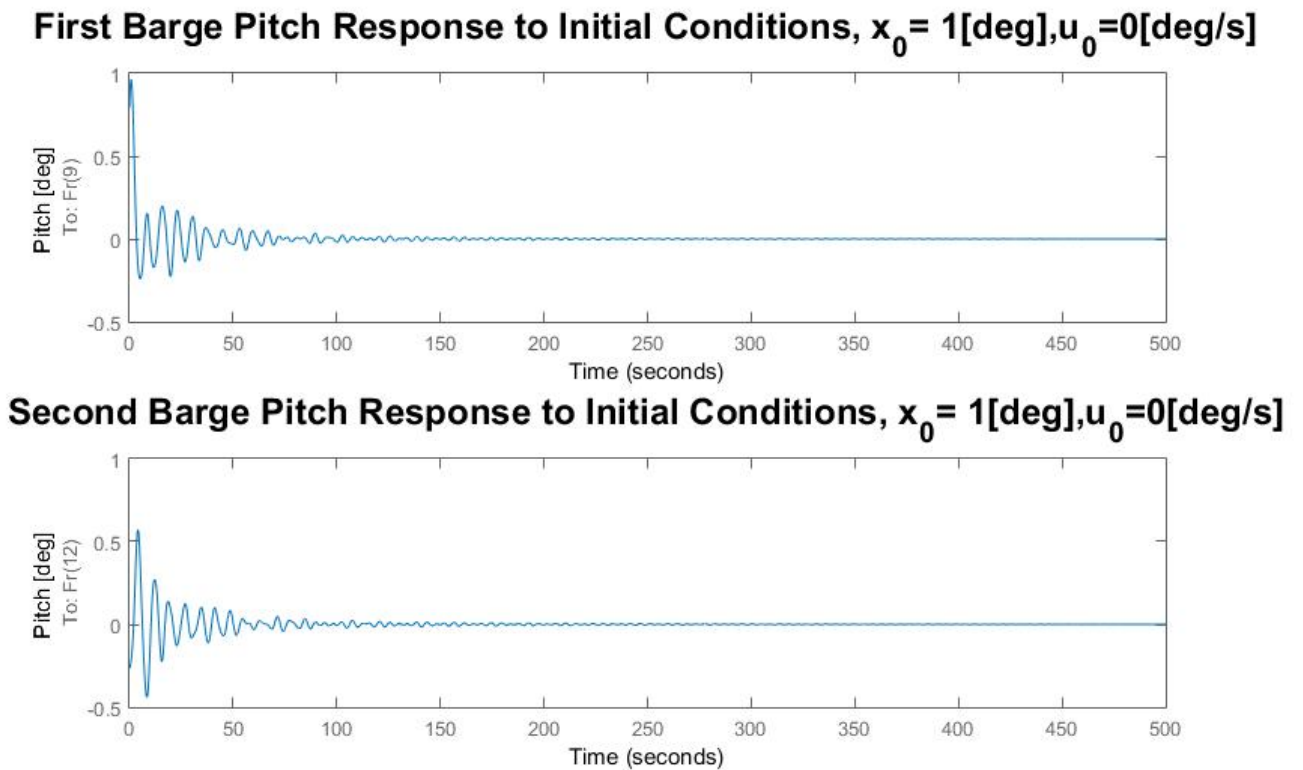
(b) Pitch response to initial conditions $\theta_0 = 1[deg], \dot{\theta}_0 = 0[deg/s]$

Figure 3.2.4: Free decay responce in heave & pitch

3.2.6   Roll Performance Filter

Choice of appropriate weight function for closed-loop performance W_p. Refering to subsection B.1, the definition and application of the band-pass filter has been given (eq. B.1.16). Assuming that the motion control mechanism attenuates effectively the bank and flip rotation around the platform reference frame but the system performance is still considered below par, a penalty can be defined around the band of interest. For example, if system roll response needs to be further reduced, a band-pass filter of the form

$$Band\ Pass\ Filter: \ \left(\frac{s}{s^2 + 2\omega_B\zeta_B s + \omega_B^2}\right)^n \tag{3.2.12}$$

could be imposed, where ω_B shall be equal to the fundamental roll frequency of the structrure ($\omega_{roll} = 0.703\ [rad/s]$) and ζ_B the damping ratio regulating the maximum allowable roll response around the resonant frequency. The choice of the filter order (integer n) depends on how quick roll-off is required. The inverse bode plot of a 12-order band pass filter for a damping ratio $\zeta_B = 0.3$ is shown in the figure below.
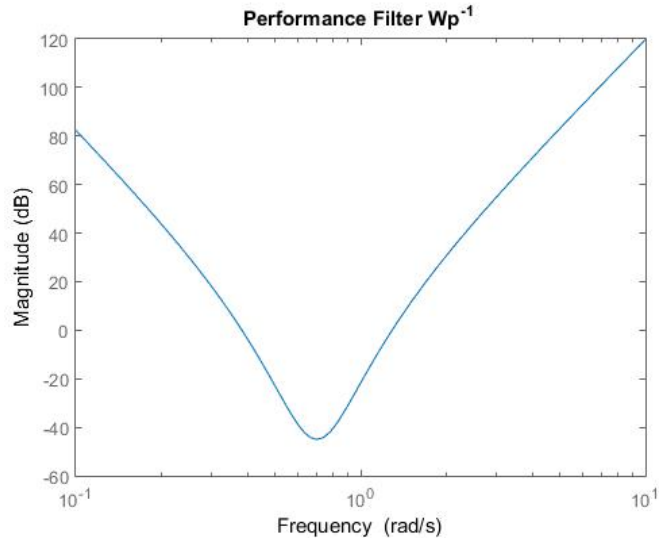
Figure 3.2.5: Band-pass filter

The control effort filter for heave and pitch DOF will be a scalar transfer function. The remaining steps comprised of the assembly of the aforementioned building blocks into the system generalized plant P
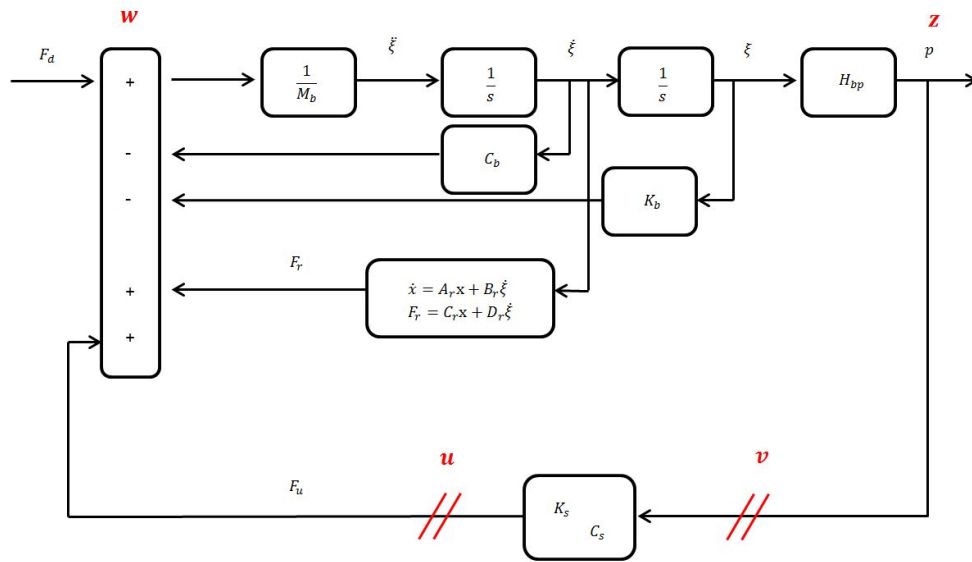
Figure 3.2.6: Radiation filter (block diagram form)

, the generalized plant and controller interconnection into standardized representation also refered to as *Standard Form* Gahinet and Apkarian (2011) and the implementation of H_∞ controller synthesis (use of hinfstruct optimization algorithm, [Apkarian and Noll (2006)]) for the T_{wz} and the mixed-sensitivity cost functions.

3.3 H_∞ Motion Optimization for MOP

In this section the integrated structural and control design concept as formulated by Grigoriadis will be incorporated in a Matlab numerical workflow where the optimization process will be carried out under the nonsmooth algorithm developed by Apkarian (`hinfstruct` - Robust Control Toolbox). The generalized plant describing the kinematically constrained barges - waves interaction as described and visualized in section 3.2 is now interconnected with the static, structured controller C as defined in section B.2 which is defined as such to provide the optimized link structural parameters (stiffness-damping) that correspond to a system allowable steady-state response in the DOF of interest. The scope of this case study is to investigate the effect of a rigid link connecting (stiffening and damping out) the configuration by comparing the system response to the constrained barges case in the previous chapter (Case A3). The verification of the beneficial effect of the link through this numerical modeling and simulation shall work as a proof of concept for MOP design.

In the system definition, the roll kinematic holonomic constraint is implemented as follows

$$\varphi_1 = \varphi_2 \tag{3.3.1}$$

where holonomic is considered to be any constraint whose expression can be integrated in the form of displacements, i.e. dependent only in (x, t). In case that the (synchronous) roll response is still higher than desired, a band pass W_P filter will be applied so to eliminate any resudual roll motion. The link structural properties will be optimized entirely in the H_∞ framework (refer to section B.2) while the effect on the system steady-state deflection will be tabulated both in the frequency and time domain. A grid search on the system performance in terms of its cost functions infinite norm will be carried out for various sets of heave-pitch link stiffness and the rationale towards the optimum solution will be given.

The equation of motion describing the barges-link-waves interactions in the frequency domain will be in the form

$$M_b * \ddot{x}(j\omega) + [C_S + C_b] * \dot{x}(j\omega) + F_R(\dot{x}) + [K_S + K_b] * x(j\omega) = F_D(\eta) + F_u + F_{ext} \tag{3.3.2}$$

where:
  M_b: barge full mass matrix
  C_S: link structural damping
  C_b : barge damping matrix
  F_R :   radiation force state space model
  K_S: link structural stiffness
  K_b : barge-platform stiffness matrix
  F_D: diffraction force state space model
  F_u : actuator force (active controller)
  F_{ext}: external force vector (mooring forces, dynamic positioning e.t.c.)

The barges full mass and hydrostatic stiffness matrix are already determined via the hydrodynamic Wamit simulation along with the scatter wave forces, properly identified in state space for postprocessing. The external force vector F_{ext} would be relevant if the horizontal DOF were in the optimization loop which is not the case in this study. However, the mooring forces could be also treated in the provided framework for a full, non-linear simulation. The same point can be made for the actuator force vector; an active control element for heave and pitch motion compensation could be designed in the H_∞ synthesis workflow so to compensate for the dynamic ripple that excites the system in transient dynamics (lift-off). In this case, the active compensation is assumed to be taken of care by the cranes hydraulic lift cylinders attached on the barges deckspace and is therefore not accounted for; nonetheless, the aforementioned case study has been already carried out and documented in the work of Wang (2015).

Since the system has been formulated in state space form and implemented in Matlab scripting, a grid search for discrete values of the parameter θ is performed. It has to be noted that for the visualization plots employed in this section, the link stiffness value in heave and pitch is 35 times higher than the corresponding hydrostatic values in the respective degrees of freedom. It will be later shown that this value ($\theta = 35$) is arguably the optimum point in the link stiffness-system performance trade-off. In figure 3.3.1 the heave, roll and pitch frequency response functions are plotted for two discrete solutions; first the "uncontrolled" scenario where the two barges are just kinematically coupled in roll and is tabulated in blue color and then the "optimized" scenario where the H_∞ synthesis is applied (red curve). By pure inspection it is clear that by employing sufficient stiffness in heave degree of freedom ($K_z = 2.1E9 \ [N/m]$) the resonant heave response is completely smoothed out, a fact that has an effect on the roll peak response as well due to hydrodynamic heave-roll coupling; by completely attenuating the dominant differential heave motion of both barges the roll spectral peak is pushed down while the secondary peaks due to coupling are extinguished completely, validating that the H_∞ principle has been successfully implemented in the MIMO cost function at hand.
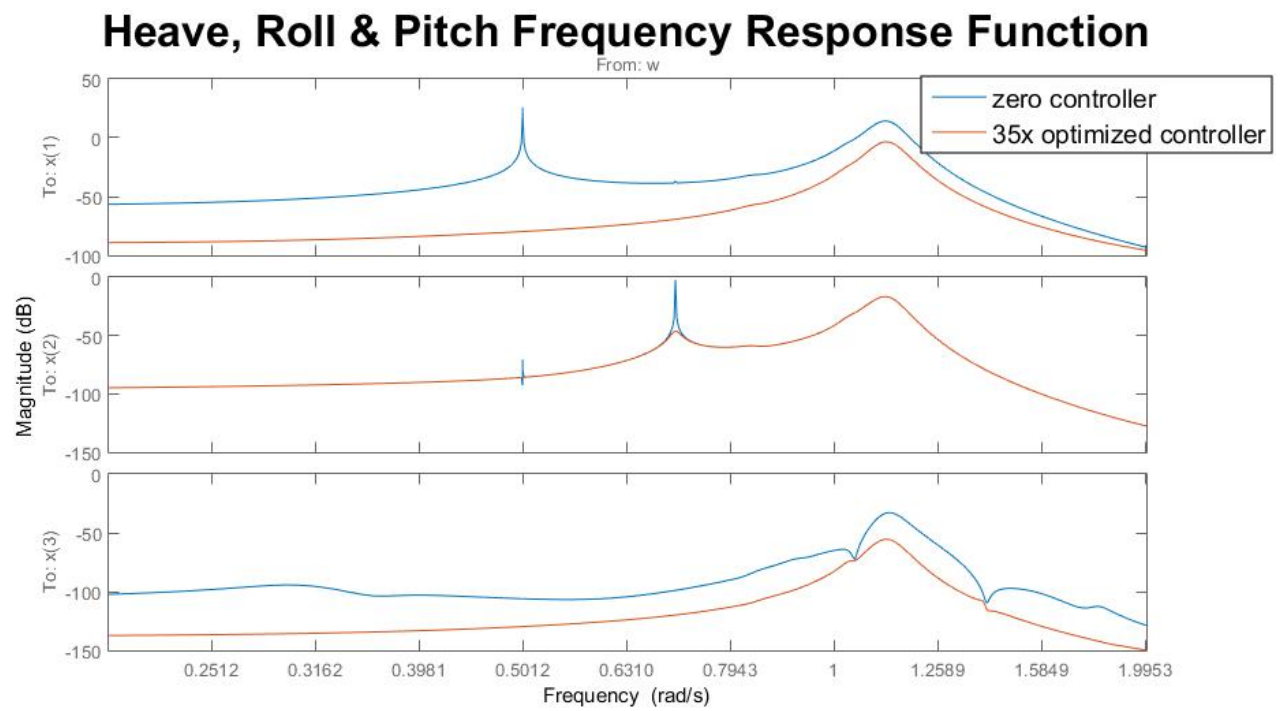
Figure 3.3.1: Heave, Roll & Pitch Frequency Response Function with and without link

However, a time domain simulation may reflect the soothing effect of the link more efficiently. In figure 3.3.2 the time response of the linked barges in irregular wave excitation is presented. The simulation sampling time is $t = 200[s]$ and the heave, roll and pitch for each barge are the 6 responses shown, respectively. It can be readily concluded that in both roll responses (second and fifth simulation) the "uncontrolled" and "controlled" scenario behavior is almost identical, showing that the roll spectral peak attenuation due to the stiffened link does not necessarily mean that the roll amplitude will be seriously attenuated. The validation that the roll kinematic constraint is successfully implemented is given via the differential roll response between barges (the roll that the link is experiencing) in figure 3.3.3. The differential roll in the "uncontrolled" case has a maximum amplitude of $2.5E - 4$, a number considered to be in the area of numerical error. It can be further noted that the first (windward) barge is heaving more (*approx.* $0.5[m]$) than the leeward barge (*less than* $0.1[m]$) as expected, while the leeward barge is pitching more due to wave trapping and higher sensitivity to weathervaning, i.e. the passive change of heading of a floating structure due to environmental action.
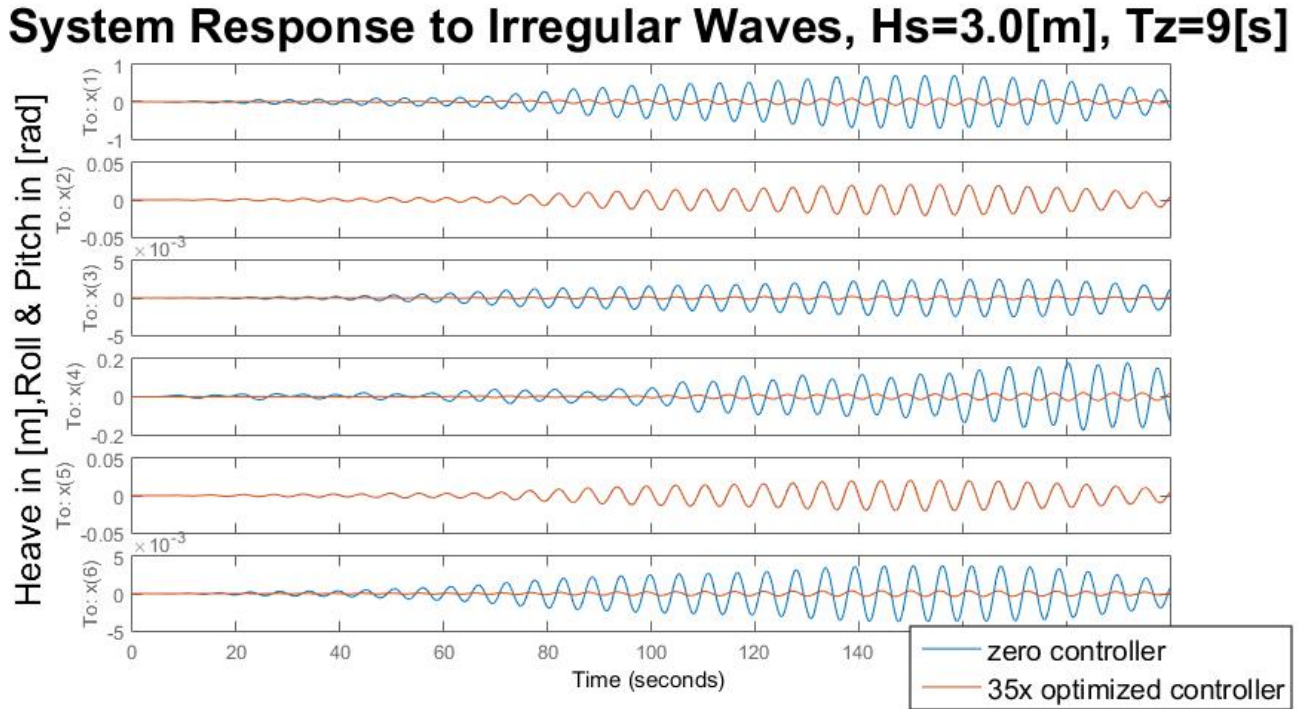
Figure 3.3.2: System Response to Irregular Waves $Hs = 3.0[m], Tz = 9[s]$

It has been already argued that during the decommissioning operation, the topside experiences a rotational deflection from static equilibrium as a result of the normalized differential heave (bank) and differential pitch (flip). In figure 3.3.4, bank and flip time simulation for both scenarios has been visualized.
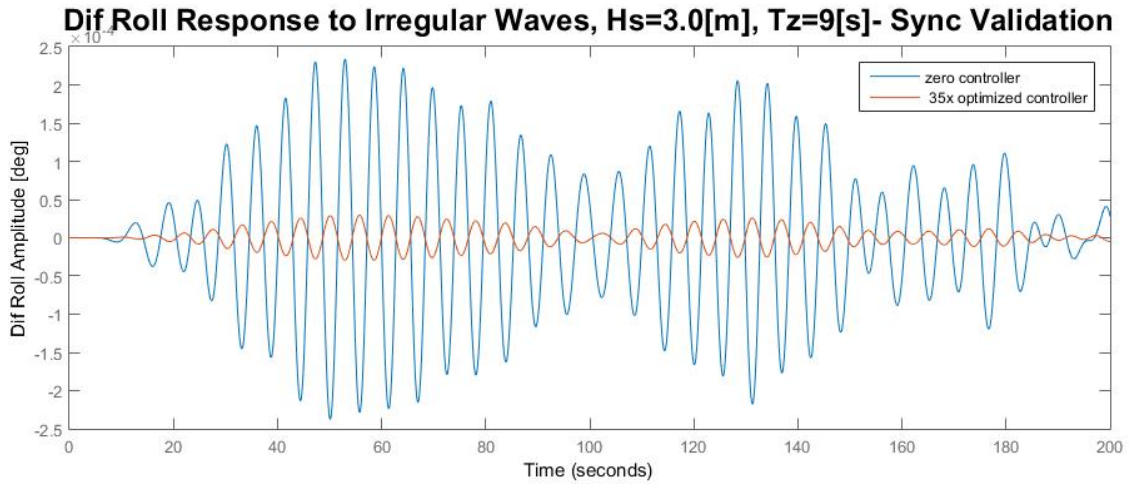
Figure 3.3.3: Validation of Mechanical Roll Coupling
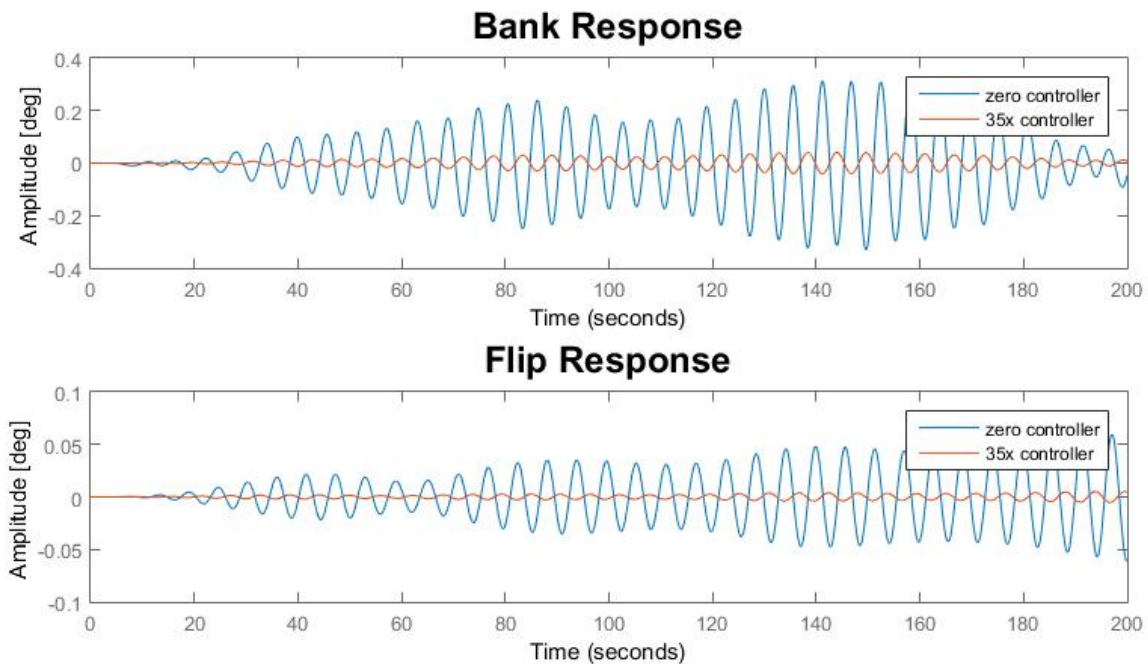
Figure 3.3.4: Bank - Flip Response to Irregular Waves $Hs = 3.0[m], Tz = 9[s]$

As expected, the link added stiffness causes a phase shift to the system response while the link material damping ($c_{heave} = 2.15E6[Nm/s]$ and $c_{pitch} = 7.01E9[Nrad/s]$) attenuates the topside rotation due to barge deflection to a minimal level. Therefore, in case that this scenario ($\theta = 35$) is adapted in next design phase, no further performance shaping of the heave and pitch transfer function is required.

As for the roll system response, the maximum dynamic response in a sufficiently long time interval of 1000 $[s]$, considering that the system fundamental roll period is around 9 $[s]$, is somewhat higher than 1.3 $[deg/m]$ resulting in excessive topside rotation. This deflection can be treated by using proper band-pass filter W_p

$$W_p = \left(\frac{s}{s^2 + 2 * 0.703 * 0.3 * s + 0.703^2} \right)^6 \tag{3.3.3}$$

(refer back to figure 3.2.5) with its peak frequency equal to the first roll frequency ($\omega_B = \omega_{roll,1} = 0.703$ $[rad/s]$). The band-pass performance filter effect in roll degree of freedom in both frequency and time domain is depicted in the figure below. It can be concluded that an performance filter whose dynamics are described by the given transfer function can effectively reduce the residual roll response within acceptable levels (< 0.1 $[deg/m]$) while working entirely in the H_∞ framework.
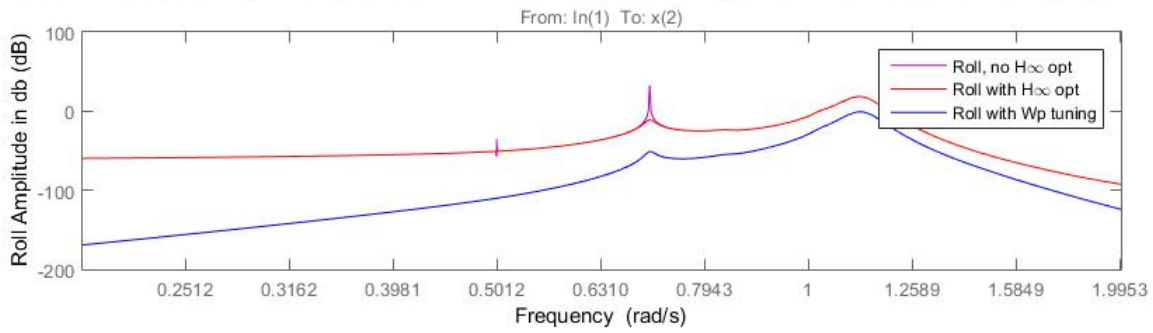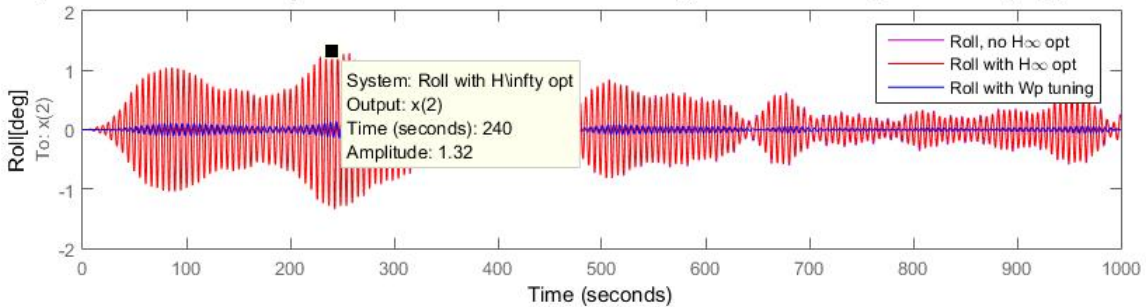
Figure 3.3.5: Synchronous Roll Response with W_p performance weight (Frequency and Time Domain)

The results so far illustrate the stiffness solution set of $[K_z, K_\theta]$ for the case where $\theta = 35$. Under the first optimization criterion, the system optimization is carried out for only one cost function (that is the $w \to z$ white noise to platform motions forward mapping) and as a result the system converges sufficiently fast ($\simeq 35\ [sec]$) to a local solution with good sub-optimal performance ($\gamma_1 = 1.07$). As for the second criterion, a S/KS mixed sensitivity stacked approach of employing band-pass filtering to roll DOF and control effort penalty in heave and pitch of each barge is applied, resulting in a 'stack' of 5 cost functions that need to be optimized under the H_∞ synthesis method. The existence of multiple cost functions rises the computational time of the optimization algorithm exponentially (in the area of 5-10 minutes), while the output system is underperforming ($\gamma_2 = 2,94$) mainly due to the fact that the algorithm output provides an admissible 'controller' where the heave material damping is zero (for computational results see the table below). Therefore the latter approach is dismissed and the optimization of T_{wz} with proper bounding of parameters is qualifying.

Link Structural Properties (ϑ=35)		
C(i,i)	Standard Approach (T_{wz})	Mixed Sensitivity Approach (S/KS)
K_{z1}	2.10E+09 $[N/m]$	2.10E+09 $[N/m]$
$K_{\theta1}$	3.92E+12 $[N/rad]$	2.23E+12 $[N/rad]$
K_{z2}	2.10E+09 $[N/m]$	4.06E+08 $[N/m]$
$K_{\theta2}$	3.92E+12 $[N/rad]$	2.14E+11 $[N/rad]$
C_{z1}	2.15E+06 $[Ns/m]$	0
$C_{\theta1}$	7.01E+09 $[Ns/rad]$	2.06E+09 $[Ns/rad]$
C_{z2}	2.15E+06 $[Ns/m]$	0
$C_{\theta2}$	7.01E+09 $[Ns/rad]$	4.27E+09 $[Ns/rad]$

Table 3.1: Comparison of link structural properties output under different solution approaches ($\theta = 35$)

The last point in the analysis workflow concerns the system performance improvement (attenuation of roll, bank and flip response) for varying parameter θ, i.e. increasing link material stiffness connecting the two barges COG under the assumption that link material damping is kept constant. As expected, for a 'soft' link design ($\theta \epsilon [2,8]$) the barges are still behaving independently resulting in poor system performance ($\gamma_i = 7.94$). However, as the link stiffness affine parameter becomes moderate ($\theta \epsilon [10,30]$), a sharply improved performance is noted, interpreted in drastically improved system's deflections in all DOF of interest. Finally, for values of $\theta > 35$, the design performance $\|T_{wz}\|_\infty$ stabilizes in a narrow performance band between 0.95 and 1.07, making it technically infeasible to "go" for a design with stiffness parameter values higher than the ones tabulated in Table 3.1.

These optimized solution sets of $[K_z, K_\theta]$ with respect to the T_{wz} infinite norm could be percieved as optimal design points that can all be go forward to design phase depending on the operational market requirements and can ultimately be fitted in a solution curve, also know as *Pareto optimal efficiency frontier*, after Vilfredo Pareto (1848–1923). This frontier signifies the optimal allocation of resources, namely link structural design and system performance in terms of platform deflections, that can be engineered for a given problem. The illustration of this optimization flow along with the optimal design point corresponding to the parameter values of Table 3.1 is presented in Figure 3.3.6.
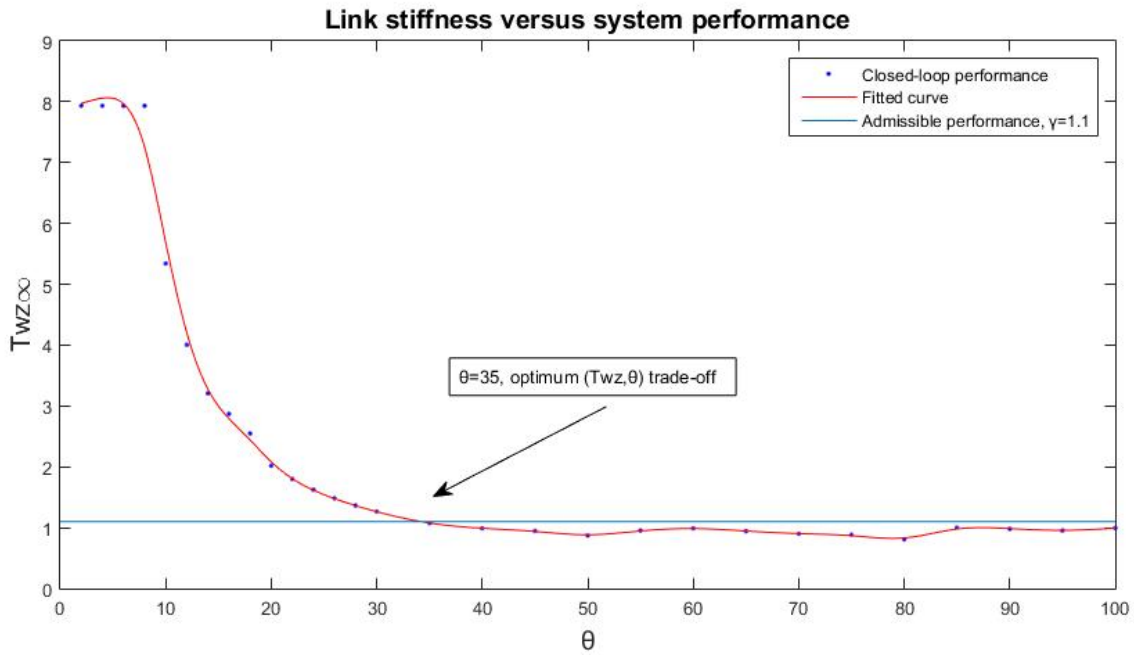
Figure 3.3.6: Grid Search for various K_z, K_θ solution sets (varying θ)

Finally, the argument that the solution corresponding to $\theta = 35$ is optimal can also be visualized via the frequency response functions and time domain simulations for different solutions, i.e. choice of small ($\theta = 6$), moderate ($\theta = 35$) an high values ($\theta = 60$) of the tunable parameter.
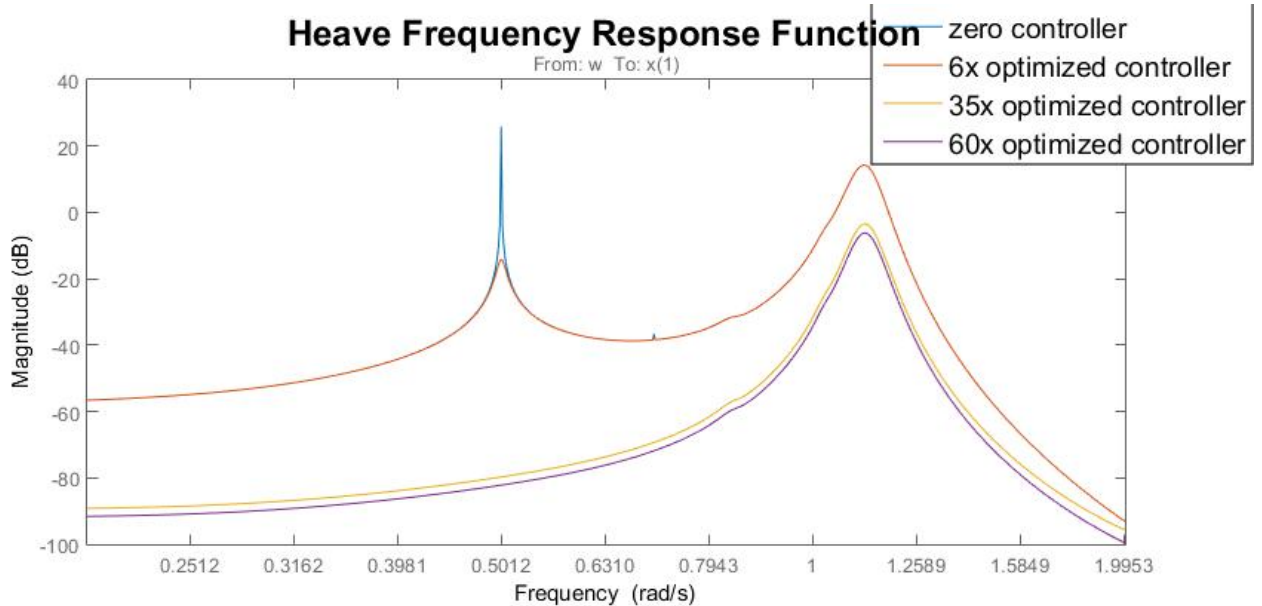
(a) Heave FRF for varying θ
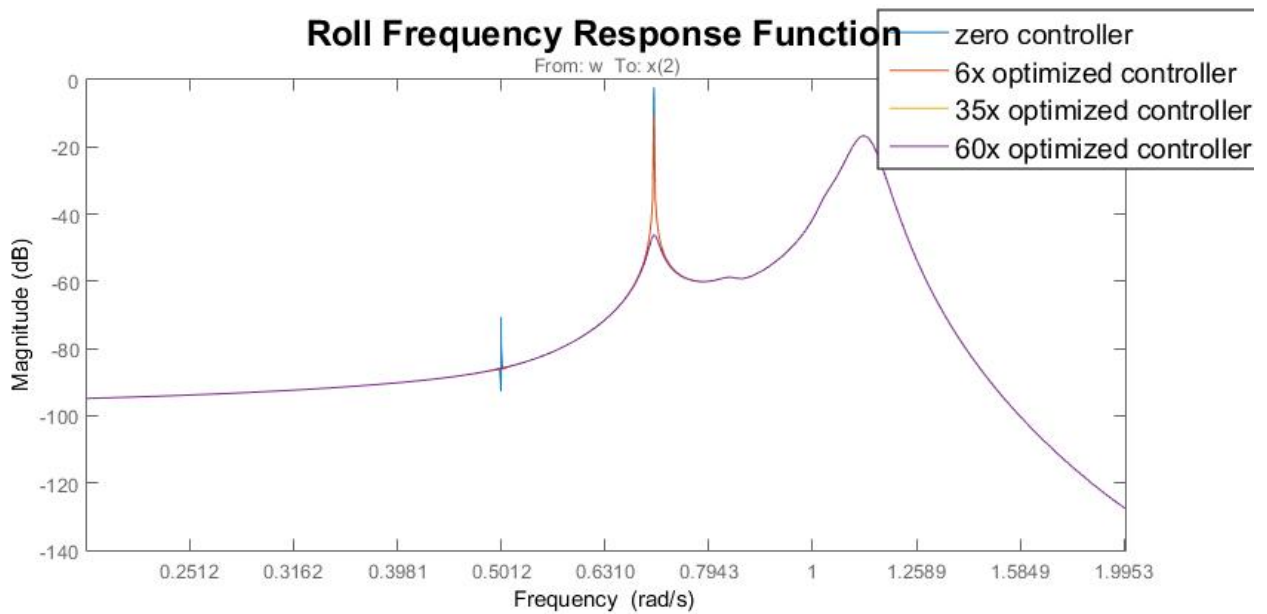
(b) Roll FRF for varying θ

Figure 3.3.7: System Frequency Response Function for varying θ

In heave frequency response function, a 'weak' link connection would attenuate the peak response but only for a moderate value the peak would be smoothed out (H_∞ scope). However a stiffer connection would barely contribute a change as shown by the 60x solution (purple curve).

Similarly for the roll frequency response function, a weak spring-dashpot passive connection is only slightly reducing the maximum roll amplitude amplitude but the optimum solution of $\theta = 35$ can cause the roll peak response to be rounded off in the range of 1.3 $[deg/m]$.
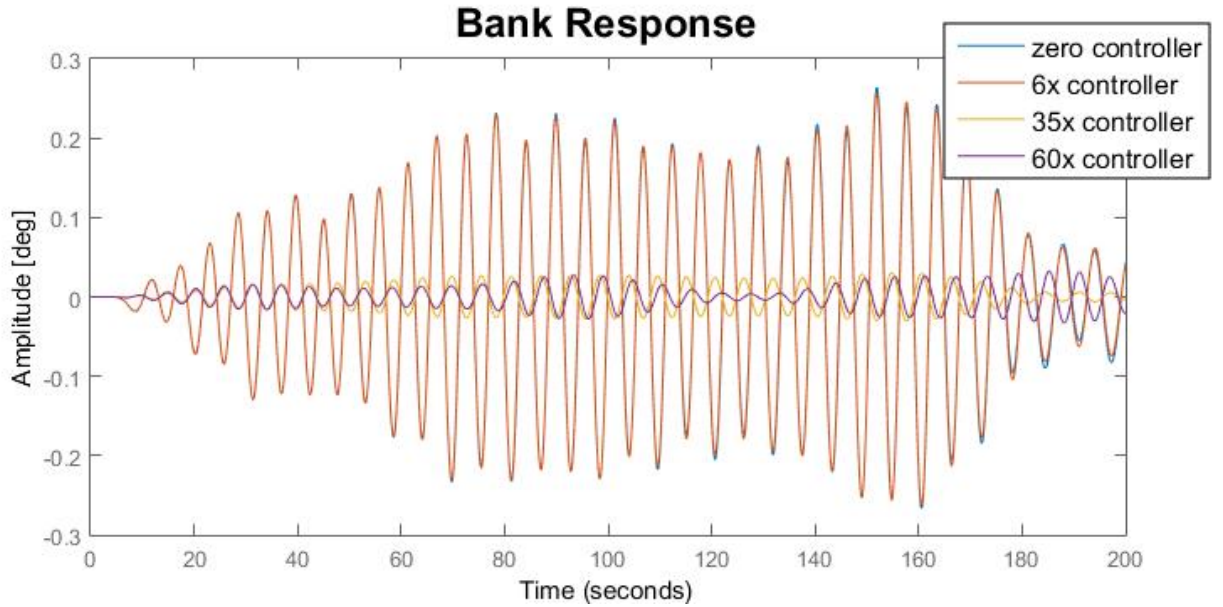
(a) Bank Response for varying θ
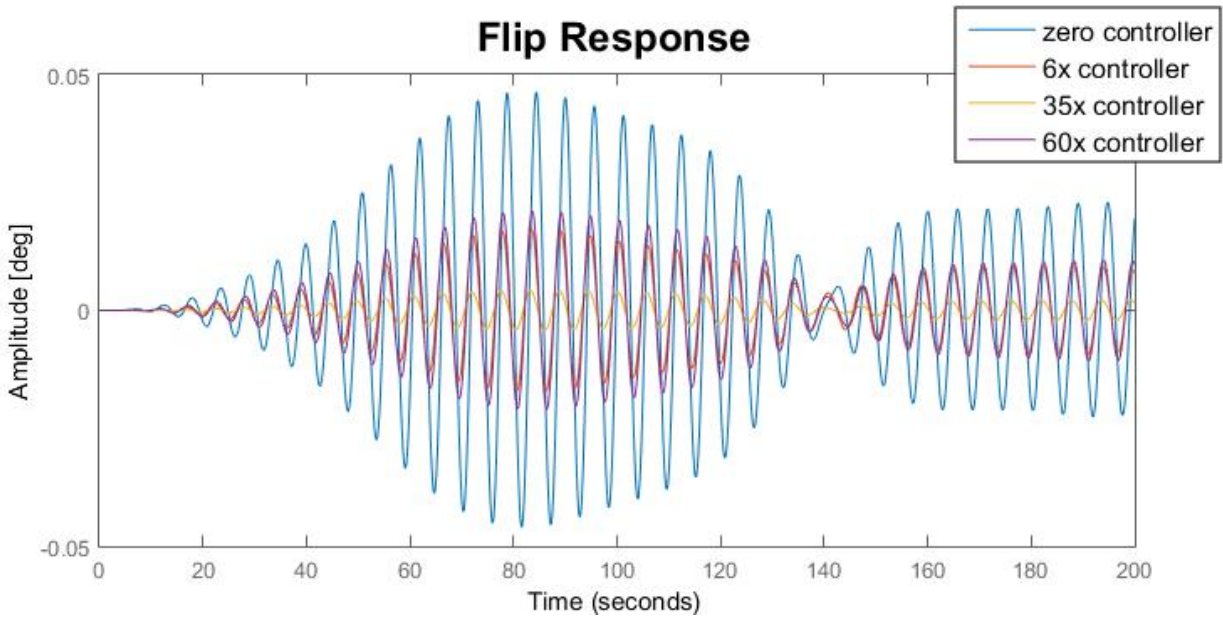
(b) Flip Response for varying θ

Figure 3.3.8: System Time Domain Simulations for varying θ

Similar conclusions can be drawn via the time domain simulations of the topside bank and flip response where the $\theta = 35$ solution is bringing a near-zero rotation for both states and obviously a stiffer solution cannot contribute better station.

Conclusively, the system descriptor dynamics (JONSWAP wave spectrum, radiation and diffraction wave effect subspace identification, barge modeling and link definition as a structured, zero order, decentralized "control" element) and kinematics (holonomic roll constraint for barge synchronization) were implemented successfully in MATLAB workflow along with the design of a performance filter element attenuating the residual first-order roll motion, described by a band-pass filter W_P, while the differential heave and pitch motion is reduced to a minimal level by adding a passive link whose parameters are affine to tunable parameter θ, optimized entirely in the H_∞ framework. As a result, the final multibody configuration ensures the required station keeping in steady state conditions (phase just before lift cylinder pretension and just after the barges-topside transient dynamics have been extinguished when fully coupled); the dynamics during lift-off have been extensively studied and respective analysis have been carried out in the works of Wang (2015)).

The passive link structural properties as derived via the system optimization plus the roll performance filter is the suggested combination of solutions for the attenuation of the system steady state response and their soothing effect has been verified in postprocessing, making this numerical workflow a proof of the MOP concept.

Chapter 4

Summary, Conclusions & Recommendations

In this Thesis a comprehensive approach on frequency domain analysis of mechanically coupled barges is made. The first part of the analysis consists of modeling diverse multibody configurations and compare their dynamic frequency response functions (FRF/RAO); more specifically the effect of a roll kinematic constraint in between barges-Case A3 is presented while its FRF is compared to the case of two freely floating barges and that of a catamaran barge configuration.

In the second part the barges-wave model is built up on a state space representation in Matlab; by successfully identifying the radiation and diffraction wave effect via constrained subspace identification algorithm tailored for this application by Janssen (2013), a new, linear time-invariant model describing the barges-wave interaction has been developed. The main objective then is to minimize the system steady-state response in (synchronized) roll, barges differential heave (denoted as ρ; bank) and differential pitch (denoted as χ; flip), the states that the topside will experience in stationary phase of the decommissioning operation, when fully coupled to the floating unit. To do so, rigid bars linking the barges are introduced with their structural properties optimized and their threshold values are derived as follows:

- link material damping is calculated by employing the logarithmic decrement method to the barges-radiation filter interconnection model; in other words, the link material damping is designed with respect to the single barge radiation damping;

- link material stiffness is up for optimization: a passive controller is defined within a static, tunable, fixed structure format. The stiffness values of this suboptimal algorithm are the components of an admissible controller derived under the following cost function minimization $min_K \|T_{wz}\|_\infty < \gamma$.

Based on the simulations presented in Chapters 2,3, the following research conclusions and recommendations for future studies can be drawn:

4.1   Conclusions

1. In the frequency domain simulation of the 3 multibody case studies, one can see that the hydrodynamic roll-roll coupling of the free floating barges (due to wave diffraction) is rather

strong, increasing the peak roll response by 30% in beam waves, compared to the corresponding response of one free floating barge, although the $65[m]$ distance between barges is rather high. However, this is not the case for heave and pitch degrees of freedom; heave-heave and pitch-pitch couplings are quite weak to non-existent as all simulations have very similar responses when compared to the one barge response. That conclusion was a first good indicator that roll hydrodynamic loading is the single design limiting parameter in terms of operability. The roll constraint is therefore deemed necessary.

2. The catamaran design is exhibiting very low roll motion response (10% of the roll response of one freely floating barge) as expected due to relatively higher configuration stiffness in all DOF; also one has to point out that the close-to-zero response at a certain period (anti-resonance or cancellation period in the literature) has also been verified by the model simulations, a desirable property of catamaran and semi-sub structures upon which its hull/pontoon dimension design is based; however, due to its stiff design, the catamaran experiences higher environmental forces (up to 2 orders of magnitude higher when compared to the other configurations), proving that this design requires more steel while making the design less agile and difficult to position between the jacket legs.

3. The roll constrained barges exhibit a roll motion response attenuated by 45% when compared to the two free floating barges but most importantly, the peak response is shifted to lower periods and consequently out of the wave period range, thus excluding the possibility of roll resonant responses throughout the operation while in steady-state. Conclusively, *the enforced roll synchronization results in roll motion optimization without adding extra stiffness to the model*, resulting to a lighter design when compared to the catamaran concept which experiences less environmental loading.

4. In the frequency domain postprocessing of the state-space model scripted in Matlab, the system response optimization with respect to the link minimum material stiffness has been successfully implemented as shown in Figure 3.3.1; the barge peak heave response has been completely smoothed and this has an effect also on the roll peak response which is hydrodynamically coupled with heave.

5. In the time-domain postprocessing, one can once more validate the successful implementation of the roll kinematic constraint (Fig.3.3.2) and differential heave and pitch motion attenuation to a minimal level via adding the passive element optimized on H_∞ framework (Fig.3.3.4). Furthermore, the residual roll response (after synchronization) is just over $1.3[deg/m]$ and further attenuation is required; a performance filter component whose dynamics were described by a band pass filter tuned on the roll channel was successfully applied so to properly treat these residual motions (Fig.3.3.5). Finally, a grid search was carried out so to determine the optimal $[\theta, \|T_{wz}\|_\infty]$ trade-off which correspond to the link material stiffness values presented in Table 3.1.

The roll kinematic constraint and respective performance band-pass filter W_P along with the bank and flip motion optimization via the H_∞ algorithm, lead to a multibody configuration with optimized motion steady-state response, yielding robust operational windows for decommissioning purposes and thus being a numerical proof of the MOP concept which can be further developed in-house.

4.2   Recommendations

1. Wamit includes the capability to analyze generalized modes of body motion thus extending beyond the classical six degrees rigid-body degrees of translation and rotation; these generalized modes can be defined so to describe and calculate structural deformations (applications on hydroelasticity for very long structures where body deformation is of essense) and motions of hinged bodies just like the case studied in this piece of research. Finally, the modeling implementation of a flexible damping lid in the free surface in between the vessels would account for the viscous damping that the linear solver cannot capture, yielding realistic responses. However, this approach requires deep knowledge of the Wamit software, good fundamentals in FORTRAN programming and background on hydroelasticity and multibody dynamics;

2. The plant-controller model carried out in Matlab ensures minimal stability and performance since no model uncertainty is considered; however the wave elevation signal derived from white noise filtering and transient dynamics during decommissioning lift-off should definitely pose uncertainty to the describing model. Therefore, the recreation of this linear model with uncertainty is recommended to be elaborated in the future;

3. The generalized plant P is a 12 x 1 non-square matrix (one white noise input; heave, roll and pitch displacement and velocity vector for each barge yielding a 12-channel output vector), which is in principle non-invertible. Therefore the definition of the sensitivity and complementary sensitivity function can be accomplished via the use of the pseudoinverse matrix. However, this approach may yield unrealistic system singular values in decomposition process, also affecting the final result and weight choice. That is why a more conservative mixed S/KS sensitivity approach is taken with a stack of 5 scalar cost functions. As a consequence the final optimization result is a poor performance estimate while the script computational time has risen exponentially. It is thus clear that S/KS mixed sensitivity approach shall be recasted for more precise derivation (and thus more techniqually feasible) of link structural properties.

4. The case studies catalogue shall be extended by simulating the dynamic response of the model in transient lift-off phase so to note how faster the system would reach steady state because of the passive link added to the model or the effect of roll compensation so to attenuate the residual roll motions; these dynamic simulation results could also be compared to the respective simulations of Wang and validate that both approaches converge to the same end result.

Appendix A

Ship Hydrodynamics

Offshore structures are experiencing external forcing induced either by the surrounding environment (waves, wind and current) or by engineering practices in order to keep the structure in course for the desired operation (mooring configuration or dynamic positioning for the horizontal excursions and rotation, control forces by actuators for the vertical motions etc.). For the particular barge structure under examination, the wave excitation is considered to be the dominant environmental disturbance and it is necessary to explicitly describe the wave modeling approach both analytically and numerically. This chapter aims in a brief but complete synopsis of the fundamental principles, assumptions and applications of 3-dimensional wave potential theory in section A.1, the modeling of young and vigorous irregular seas which best describe the sea behavior in North Sea (JONSWAP spectrum - section A.2), summarizing the essential background on ship kinematics, which describe the geometry aspect of body motion in waves (section A.3) and ship kinetics; the wave force effect to body motion (section A.4) distinguished and further explained in the following two sub-problems:

- the *radiation problem* (or ship forced excitation in calm waters) which provides the potential flow hydrodynamic coefficients, namely the added mass (Aij) and the potential damping (Bij) and

- the *scatter problem* (or vessel response to incident & diffracted wave action when stationary) which provides the generalized force vector to the inhomogeneous set of differential equations

Additionally, the theory behind the *wave response amplitude operator* (motion & force transfer function known as RAO) is provided. Furthermore, the 3D potential theory implementation in Wamit linear radiation/diffraction solver is presented and its main input-output files will be introduced and explained in order to familiarize the reader with the line of thinking narrated in the main body of this report. The files that will be presented are:

- Input files: potential control file (*.pot); geometry data file (*.gdf); configuration file (*.cfg); force control file alternative forms 1 & 2 (*.frc)

- Output files: intermediate data transfer file (*.p2f); formatted output file (*.out); auxiliary files for barge hydrostatic (*.hst) and inertia, damping and stiffness properties (*.mmx)

In section A.5 the importance of simulating a full 3D radiation-diffraction model so to depict the hydrodynamic interaction of bodies in proximity and the points that need special attention during

the numerical implementation are highlighted. Finally, the subspace identification approach used for the derivation of radiation-diffraction state space models and the corresponding methods used for their internal state reduction with no loss of information is presented in sections 2.6 & 2.7, respectively.

A.1 Potential Theory Assumptions

The fundamental principle of potential fluid flow is that the flowing material is considered to be continuous, homogeneous, inviscid and incompressible (constant fluid density ρ), while the surface tension may be neglected for a conservative system linear analysis. Therefore if a differential fluid element with block dimensions dx, dy, dz is considered , the equation of conservation of mass (*continuity equation*) will be:

$$\frac{\partial u}{\partial x} + \frac{\partial v}{\partial y} + \frac{\partial w}{\partial z} = 0 \tag{A.1.1}$$

where u,v and w are the components of the fluid velocity vector in x,y and z directions, respectively. By introducing the *velocity potential* Φ, a parameter which has no physical representation to the fluid flow but is vital for the calculation of the fluid velocity vector later on in the analysis, with the property that the velocity component in any direction is merely the derivative of the Φ function to the very same direction:

$$u = \frac{\partial \Phi}{\partial x}; v = \frac{\partial \Phi}{\partial y}; w = \frac{\partial \Phi}{\partial z} \tag{A.1.2}$$

Then, if the velocity potential components are substituted to the continuity equation, the *Laplace Equation* for potential flows is derived:

$$\nabla^2 \Phi = 0 \tag{A.1.3}$$

Additionally, via the application of the inviscous flow assumption to Newton's second law ($\overrightarrow{f} = m * \overrightarrow{a}$), the *Euler equations* of fluid flow are obtained:

$$\frac{\partial u}{\partial t} + u\frac{\partial u}{\partial x} + v\frac{\partial u}{\partial y} + w\frac{\partial u}{\partial z} = -\frac{1}{\rho}\frac{\partial p}{\partial x} \tag{A.1.4}$$

$$\frac{\partial v}{\partial t} + u\frac{\partial v}{\partial x} + v\frac{\partial v}{\partial y} + w\frac{\partial v}{\partial z} = -\frac{1}{\rho}\frac{\partial p}{\partial y} \tag{A.1.5}$$

$$\frac{\partial w}{\partial t} + u\frac{\partial w}{\partial x} + v\frac{\partial w}{\partial y} + w\frac{\partial w}{\partial z} = -\frac{1}{\rho}\frac{\partial p}{\partial z} \tag{A.1.6}$$

This assumption is valid for all stream lines except the ones within a small sublayer close to the hull surface where nonlinear (viscous) effects take place. Finally by neglecting the friction within the fluid elements constituting the flow, no energy dissipation occurs (the system is conservative), the *Bernoulli equation* for a stationary flow along a stream line Ψ, is provided:

$$\frac{V^2}{2g} + \frac{p}{\rho g} + z = constant \tag{A.1.7}$$

a formula which is used for the fluid pressure calculation on the structure (barge hull). The integration of fluid pressure along the body hull with a higher order panel method results to the hydrodynamic forces acting on the body used for the system equation of motion formulation in frequency domain. Now that the fluid flow assumptions are fully defined, it remains to define how this fluid interacts with its surroundings, namely the sea bed ($z = -h$), the free surface ($z = 0$) and the floating body by introducing proper boundary conditions in order to determine the wave velocity potential space-dependent part $P(z)$ which is yet unknown explicitly:

$$\Phi_w(x, z, t) = P(z) * sin(kx - \omega t) \tag{A.1.8}$$

At first, by substituting eq. A.1.8 in eq. A.1.3, a homogeneous linear differential equation of the second order is yielded with a straightforward general solution:

$$\frac{d^2 P(z)}{dz^2} - k^2 P(z) = 0 \implies P(z) = C_1 e^{kz} + C_2 e^{-kz} \tag{A.1.9}$$

$$\Phi_w(x, z, t) = (C_1 e^{kz} + C_2 e^{-kz}) * sin(kx - \omega t) \tag{A.1.10}$$

It stands that the seabed is impermeable to water particles and therefore it is valid to assume at $z = -h$ (*seabed boundary condition*):

$$\frac{\partial \Phi_w}{\partial z} = 0 \tag{A.1.11}$$

Substituting the free surface boundary condition to the velocity potential definition the resulting form is further simplified:

$$\Phi_w(x, z, t) = C * cosh(h + z) * sin(kx - \omega t) \tag{A.1.12}$$

Additionally, the water pressure at the free surface $z = 0$ equals the atmospheric pressure. This statement with proper manipulation of the Bernoulli equation (eq.A.1.7) yields the (linearized) *free surface dynamic boundary condition*:

$$\frac{\partial \Phi_w}{\partial t} + g\zeta = 0 \tag{A.1.13}$$

Eq.A.1.13 is very important since it relates the *wave elevation function* with the *velocity potential* which are in turn:

$$\zeta = \zeta_\alpha cos(kx - \omega t) \; ; \zeta_\alpha = \frac{\omega C}{g} cosh(kh) \tag{A.1.14}$$

$$\Phi_w = \frac{\zeta_\alpha g}{\omega} \frac{cosh(h + z)}{cosh(kh)} sin(kx - \omega t) \tag{A.1.15}$$

In deep waters ($h \to \infty$) the *velocity potential* becomes:

$$\Phi_w = \frac{\zeta_\alpha g}{\omega} e^{kz} sin(kx - \omega t) \tag{A.1.16}$$

which is the generic form that will be used from now on to the analysis. Furthermore, the vertical velocity component of a fluid particle in the free surface must be identical to the vertical velocity of the free surface it self which yields the *free surface kinematic boundary condition*, which in turn provide information for the wave kinematics, the well known *dispersion relationship*:

$$\frac{\partial \Phi}{\partial z} + \frac{\partial \zeta}{\partial t} = 0 \tag{A.1.17}$$

$$\omega^2 = kg * tanh(kh) \tag{A.1.18}$$

Eq.A.1.18 in deep water ($tanh(kh) = 1$) can be further simplified while the relation between the wave period and wave length in deep water is:

$$\omega^2 = kg \tag{A.1.19}$$

$$\lambda = \frac{g}{2\pi}\mathrm{T}^2 \tag{A.1.20}$$
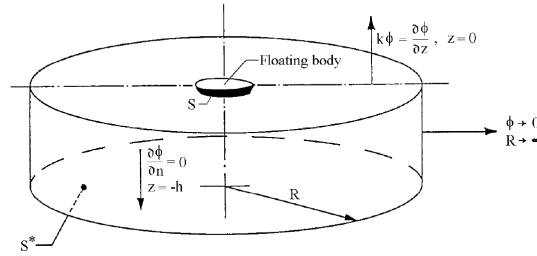
Figure A.1.1: Boundary conditions in near and far-field

The boundary conditions mentioned above capture the fluid behavior in the near-field; as far as the far-field is concerned, the velocity potential effect shall tend to zero in "sufficiently large" distance R, known as the *radiation condition*:

$$lim_{R\to\infty}\Phi = 0 \tag{A.1.21}$$

A.2 Modeling of Ocean Waves & Wave Spectra

In the previous section, the definitions describing regular waves of the linear potential theory are given. It is however well known that regular waves are not met in nature; ocean waves are random both in time and space and they should be more realistically described as a linear superposition of regular harmonic waves with its unique characteristics (wavelength, frequency, amplitude and directionality) to be modeled in a stochastic framework. It is usually assumed that the variations of a stochastic nature of the sea are much slower that the variations of the sea surface itself; therefore the sea elevation $\zeta(x, y, t)$ is considered a realization of a stationary and homogeneous zero-mean Gaussian stochastic process [Perez (2006)].

The statistical properties of the wave surface elevation are summarized in the power spectral density plot, best known as wave spectrum $S_\zeta(\omega)$, describing how the wave energy is distributed in the frequency domain. In 1968 an extensive wave measurement program known as the Joint North Sea Wave Project (abbr. JONSWAP) was carried out and it is still proven to be the wave spectrum that best describes fetch-limited wind generated seas. Its power spectral density is defined as follows:

$$S_\zeta(\omega) = \frac{320H_{1/3}^2}{T_p^4}\omega^{-5}exp(\frac{-1950}{T_p^4}\omega^{-4})\gamma^A \tag{A.2.1}$$

where:

T_p : peak period $(Tp \simeq 1.2 - 1.25 * T_z)$
$H_{1/3}$: characteristic wave height
$\gamma = 3.3(peakedness factor)$
$A = exp\{-(\frac{\frac{\omega}{\omega_p}-1}{\sigma\sqrt{2}})^2\}$
$\sigma = 0.07$ for $\omega \leq \omega_p; 0.09$ for $\omega \leq \omega_p$
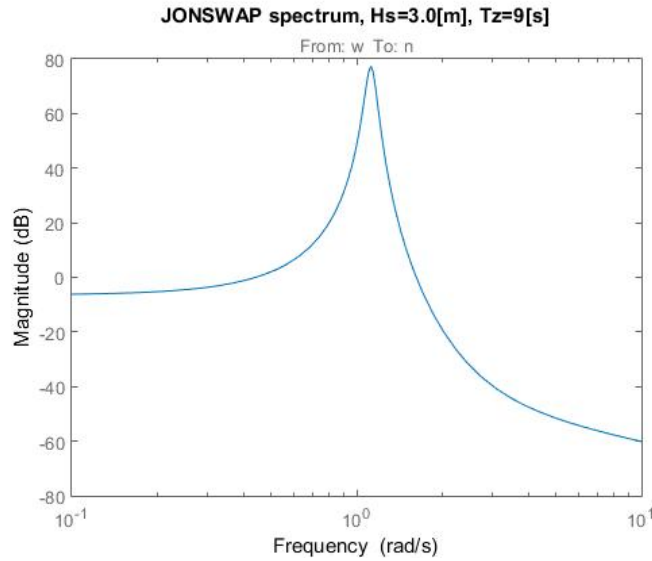
Figure A.2.1: JONSWAP spectrum for $H_s = 3.0 \; [m], T_z = 9 \; [s]$

A.3 Ship Kinematics

In section A.3 the basic ship definitions on orientation, body-fixed and steadily translating (hydrodynamic) coordinate reference frames and body motion at COG and any point of the structure will be given.

Ship Conventions

When on board, a ship looking toward the bow (front end) one is looking forward; the ship stern is aft at the other end of the ship. As one looks forward, the starboard side is one's right and the port side is one's left.

Body-fixed frame b   The b-frame (o_b, x_b, y_b, z_b) is fixed on the hull, positive x_b towards the bow, y_b towards starboard and z_b pointing downwards. For marine motion analysis the origin of this frame is conveniently chosen to be the body's center of gravity.

Steadily translating (hydrodynamic) frame h   The h-frame (o_h, x_h, y_h, z_h) is not fixed to the hull; it moves following the free surface motion; the x_h, y_b plane coincides with the mean water surface, positive x_h pointing forward, y_h pointing towards starboard and z_h pointing upwards. This frame is considered in the hydrodynamic analysis to compute the wave induced motion/forces for ship motion and motion control purposes.
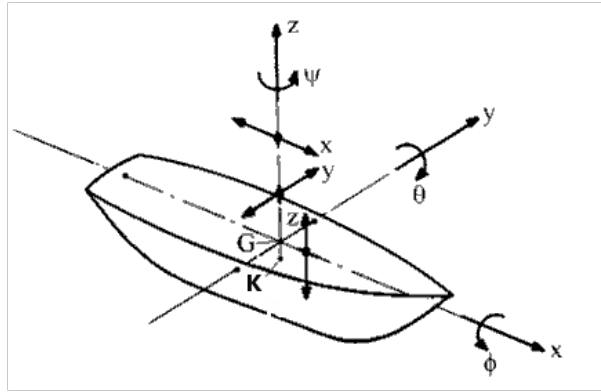
Figure A.3.1: Body-fixed and hydrodynamic frame conventions

The harmonic 6 rigid body motions in the h-frame are defined by 3 translations and 3 rotations of the body's COG (o_b, x_b, y_b, z_b) as follows:

$$Surge: \qquad x = x_a cos(\omega t + \varepsilon_{x\zeta}) \qquad\qquad (A.3.1)$$

$$Sway: \qquad y = y_a cos(\omega t + \varepsilon_{y\zeta}) \qquad\qquad (A.3.2)$$

$$Heave: \qquad z = z_a cos(\omega t + \varepsilon_{z\zeta}) \qquad\qquad (A.3.3)$$

$$Roll: \qquad \varphi = \varphi_{\alpha} cos(\omega t + \varepsilon_{\varphi\zeta}) \tag{A.3.4}$$

$$Pitch: \qquad \theta = \theta_{a} cos(\omega t + \varepsilon_{\theta\zeta}) \tag{A.3.5}$$

$$Yaw: \qquad \psi = \psi_{a} cos(\omega t + \varepsilon_{\psi\zeta}) \tag{A.3.6}$$

Knowing the motions aroung the body's COG one can calculate the motions in any point on the structure by employing the superposition principle. The transformation between the b-to-h frames comes as the multiplication of three rotations around the principal axis:

$$R_b^h(\Theta_{hb}) \triangleq R_{z,\psi} R_{y,\theta} R_{x,\phi} \tag{A.3.7}$$

where

$$
R_{x,\phi} \triangleq \begin{bmatrix} 1 & 0 & 0 \\ 0 & c\phi & -s\phi \\ 0 & s\phi & c\phi \end{bmatrix}
$$
$$
R_{y,\theta} \triangleq \begin{bmatrix} c\theta & 0 & s\theta \\ 0 & 1 & 0 \\ -s\theta & 0 & c\theta \end{bmatrix} \tag{A.3.8}
$$
$$
R_{z,\psi} \triangleq \begin{bmatrix} c\psi & -s\psi & 0 \\ s\psi & c\psi & 0 \\ 0 & 0 & 1 \end{bmatrix}
$$

Under the assumption of small angles of rotation ($cos\xi = 1$; $sin\xi = \xi$) which is necessary for the matrix linearization which now becomes:

$$
\begin{pmatrix} x \\ y \\ z \end{pmatrix} = \begin{pmatrix} 1 & -\psi & \theta \\ \psi & 1 & -\varphi \\ -\theta & \varphi & 1 \end{pmatrix} \cdot \begin{pmatrix} x_b \\ y_b \\ z_b \end{pmatrix} \tag{A.3.9}
$$

in which x,y,z,φ,ϑ,ψ are the body motions about the center of gravity. Using the eq. A.3.9 the absolute harmonic motion of a certain point $P(x_b, y_b, z_b)$ can be determined.

A.4 Ship Kinetics (3D Radiation - Scatter Theory)

The background covered in previous sections enclose the first order (linear) wave potential theory and spectral statistics in frequency domain along with the kinematics of ship motion, i.e. the geometrical aspect of motion: definition of system variables, reference frames and matrix transformations. This section is about the kinetics of body motion; the study of hydrodynamic forces acting on it and the motion response produced. With the formulation covered in sections A.3 and A.4, one can derive the dynamic model of body in waves.

The velocity potential formulation is now determined which consequently leads to the calculation of the fluid velocity vector and the corresponding hydrodynamic pressures exerted on the body surface by utilizing the linearized Bernoulli equation. The direct integration of these pressures, using complex source strength and Green's function, provide the hydrodynamic forces and moments acting on the body. However, the physical representantion of these forces and moments is not straightforward; different phenomena are superimposed in order to synthesize the velocity potential Φ which are needed to be described in detail. Therefore, a step back is taken in the definition of the velocity potentials which now becomes:

$$\Phi(x, y, z, t) = \Phi_{rad} + \Phi_{FK} + \Phi_d \tag{A.4.1}$$

where the terms represent the velocity potential components due to radiation, incoming and diffracted waves, respectively. These effects are only wave frequency dependent, subject to environmental excitation of unitary (wave) amplitude and they can be treated as a body's inherent frequency characteristic. Therefore, the way a body of known properties respond in external harmonics over a frequency range can completely describe the body's behavior; it is a hydrodynamic property. The explanation of all three phenomena is attempted herein. It is noted that second order wave excitation forces (mean and slowly-varying drift forces) become quite significant when aiming in the system station on the horizontal degrees of freedom (surge, sway and yaw), namely mooring analysis or dynamic positioning control. This falls out of the scope of this case study and is therefore not explained in depth. Finally, the actuation forces induced on the system by a control system design to counteract the effect of second order drift forces or differential motions on multibody configurations is an issue properly addressed in Chapter B.
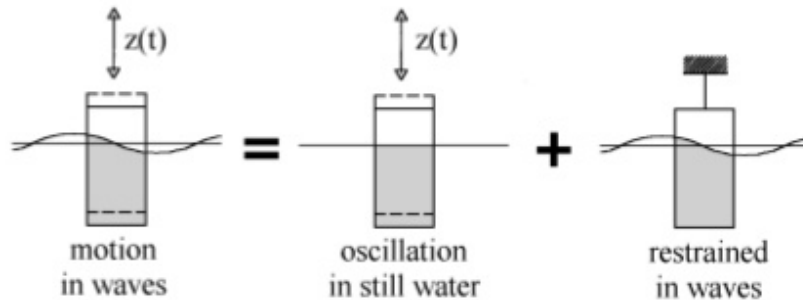
Figure A.4.1: Superposition of radiation and scatter in linear analysis

Equations of Motion

The seakeeping theory is based on the use of the hydrodynamic reference frame h to describe the body-fluid interaction. The equation of motion in the h frame will be

$$M^h \ddot{\xi} = \tau_{hyd}^h \qquad (A.4.2)$$

where ξ represents the generalized 6 rigid-body motions vector (eq. A.3.1-A.3.6). The components of the right hand side vector τ_{hyd} are the generalized hydrodynamic forces acting on the body

$$\tau_{hyd} = \tau_r + \tau_{1w} + \tau_{2w} + \tau_v + \tau_{hs} \qquad (A.4.3)$$

where

- Radiation forces (τ_r), appearing due to change in momentum of the fluid because of the body motion, further decomposed to added-mass forces (proportional to body's accelerations) and damping forces (proportional to body's velocities) - subsection A.4

- First order wave scatter forces (τ_{1w}), seperated to the incoming Froude-Kriloff forces and the diffraction forces - subsection A.4

- Second order wave drift forces (τ_{2w}), slowly varying (difference frequencies) and rapidly varying (sum frequencies) wave loads.

- Viscous forces (τ_v), non-linear damping forces due to non-conservative phenomena of energy dissipation (skin friction, flow separation phenomena etc.)

- Hydrostatic forces (τ_{hs}), restoring 'spring' forces (proportional to body's translations and rotations). The non-zero spring coefficients are in heave roll and pitch, and their non-trivial terms are namely:

$$c_{33}^h = \rho g \iint_{S_b} n_3 dS = \rho g A_{wl}$$

$$c_{35}^h = c_{53}^h = -\rho g \iint_{S_b} x n_3 dS$$

$$c_{44}^h = \rho g \iint_{S_b} y^2 n_3 dS + \rho g \nabla z_b - mg z_g = \rho g \nabla GM$$

$$c_{55}^h = \rho g \iint_{S_b} x^2 n_3 dS + \rho g \nabla z_b - mg z_g = \rho g \nabla GM_L \qquad (A.4.4)$$

Finally M is the generalized mass matrix, all with respect to the h frame:

$$M^h = \begin{bmatrix} m\ I_{3x3} & -m\ S(r^h) \\ m\ S(r^h) & I^h \end{bmatrix}$$

$$= \begin{bmatrix} m & 0 & 0 & 0 & mz_g^h & -my_g^h \\ 0 & m & 0 & -mz_g^h & 0 & mx_g^h \\ 0 & 0 & m & my_g^h & -mx_g^h & 0 \\ 0 & -mz_g^h & my_g^h & I_{xx}^h & -I_{xy}^h & -I_{xz}^h \\ mz_g^h & 0 & -mx_g^h & -I_{yx}^h & I_{yy}^h & -I_{yz}^h \\ -my_g^h & mx_g^h & 0 & -I_{zx}^h & -I_{zy}^h & I_{zz}^h \end{bmatrix} \qquad (A.4.5)$$

where the vector $r^h = [x_g^h, \ y_g^h, \ z_g^h]$ are the COG coordinates and $S(.)$ is the skew-symmetric matrix

$$S(r^h) = \begin{bmatrix} 0 & -z_g^h & y_g^h \\ z_g^h & 0 & x_g^h \\ -y_g^h & -x_g^h & 0 \end{bmatrix} \tag{A.4.6}$$

The moments of inertia for the inertia tensor I^h can be calculated as follows:

$$I_{xx} = \int_\nabla [(y^h)^2 + (z^h)^2]\rho dV \qquad\qquad I_{xy} = I_{yx} = \int_\nabla (y^h x^h)\rho dV$$

$$I_{yy} = \int_\nabla [(z^h)^2 + (x^h)^2]\rho dV \qquad\qquad I_{xz} = I_{zx} = \int_\nabla (z^h x^h)\rho dV$$

$$I_{zz} = \int_\nabla [(y^h)^2 + (x^h)^2]\rho dV \qquad\qquad I_{zy} = I_{yz} = \int_\nabla (y^h z^h)\rho dV \tag{A.4.7}$$

Radiation Effect

"The hydrodynamic forces are the total reaction forces of the fluid on the oscillating cylinder, caused by this motion in (initially) still water", Newman [1977]

Newman identified the radiation components by model basin decay tests where a body of known properties is assumed to float in calm ideal-fluid water and let oscillate under external harmonic excitation in a certain degree of freedom. The body will oscillate while this movement results in the perturbation of the water surface; the body motions radiate waves. The body-to-waves transfer of energy results to the body's motion dissipation; the radiation force has a *damping* term (proportional to body velocity $\dot{\xi}$) with a corresponding hydrodynamic damping coefficient c $[Ns/m]$. In addition to that, the body's *inertia* is interacting with the water particles around the wetted surface of the body and are contributing (adding) to the body's inertia. This component is proportional to body acceleration $\ddot{\xi}$ with a corresponding hydrodynamic added mass coefficient a $[Ns^2/m]$. Finally, the body will react to the external excitation (Archimedes law) with restoring linear *spring* terms which are present to heave, roll and pitch only with a hydrostatic stiffness coefficient k $[N/m]$. Applying Newton's second law yields:

$$F_{rad} = m\ddot{\xi} \Rightarrow (m+a)\ddot{\xi} + c\dot{\xi} + k\xi = 0 \tag{A.4.8}$$

The radiation effect is now generalized to all 6 degrees of freedom and the radiation velocity potential term $\Phi(x, y, z, t)$ is now separated to a space-dependent and time-dependent term with (separation of variables):

$$\Phi_i(x, y, z, t) = Re\left\{\varphi_i(x)v_i(t)\right\} \tag{A.4.9}$$

The wave velocity potential for deep waters is given by the following equation:

$$\Phi_i = \frac{-\zeta_\alpha g}{\omega} e^{\kappa z} sin(\omega t - kx) \tag{A.4.10}$$

Hydrodynamic forces and moments can now be calculated from a direct pressure integration of pressure p over the body wetted surface from the linearized Bernoulli equation as follows:

$$\overrightarrow{F_r} = \rho \int \int_S \left(\frac{\partial}{\partial t} \sum_{i=1}^{6} \varphi_i(x) v_i(t) \right) \overrightarrow{n} \, dS \tag{A.4.11}$$

$$M_r = \rho \int \int_S \left(\frac{\partial}{\partial t} \sum_{i=1}^{6} \varphi_i(x) v_i(t) \right) (\overrightarrow{r} x \overrightarrow{n}) \, dS \tag{A.4.12}$$

Defining the oscillatory motion (complex notation):

$$\xi_j = \xi a_j e^{-i\omega t}$$

$$v_j = \overset{.}{} = -i\omega \xi_{aj} e^{-i\omega t} \dot{\xi}_j \tag{A.4.13}$$

$$\alpha_j = \ddot{\xi}_j = -\omega^2 \xi_{aj} e^{-i\omega t}$$

By substituting eq.A.4.13 in eq.A.4.11, radiation forces can now be written in the following format:

$$\overrightarrow{F_{r,ji}} = Re \left\{ -\rho \omega^2 \xi_{ji} \int \int_S (\varphi_\iota) \, n_i dS e^{-i\omega t} \right\} \tag{A.4.14}$$

The time dependent part can now be deleted by equating eq.A.4.14 and eq.A.4.8 and hydrodynamic added mass and damping coefficients are determined for all 6 rigid body degrees of freedom:

$$a_{ji} = -\rho Re \left\{ \int \int_S \varphi_\iota n_i dS \right\}$$

$$c_{ji} = -\rho \omega Im \left\{ \int \int_S \varphi_\iota n_i dS \right\}, i, j = 1..3 \tag{A.4.15}$$

$$a_{ji=} - \rho Re \left\{ \int \int_s \varphi_i (\overrightarrow{r} x \overrightarrow{n})_i dS \right\}$$

$$c_{ji} = -\rho \omega Im \left\{ \int \int_s \varphi_i (\overrightarrow{r} x \overrightarrow{n})_i dS \right\}, i, j = 4..6 \tag{A.4.16}$$

Scatter Wave effect

The incoming and diffracted wave effect (scatter problem) is identified experimentally by constraining the body in all 6 degrees of freedom and calculating the wave loads exerted on the body by the generated waves. In the analytical formulation of the hydrodynamic potential added mass and damping, the problem consisted of a set of *homogeneous* linear differential equations just by merely assuming that the incoming wave velocity potential (Φ_0) and the respective diffracted potential (Φ_7) are zero while the radiation force components migrated to the left side of the equation. In this instance, the incoming wave (so-called Froude-Krilov force) and diffracted forces and moments are non trivial and therefore treated separately. The r.h.s of eq.A.4.8 is now:

$$F_{FK} + F_d = -\rho \int \int_S \left(\frac{\partial \Phi_{FK}}{\partial t} + \frac{\partial \Phi_d}{\partial t} \right) \vec{n} dS \tag{A.4.17}$$

By principle, the velocity potential on the hull of a restrained rigid body with zero forward speed will be zero (no water pressure can penetrate the ship hull):

$$\frac{\partial \Phi}{\partial n} = \frac{\partial \Phi_{FK}}{\partial n} + \frac{\partial \Phi_d}{\partial n} = 0 \tag{A.4.18}$$

Where n the outward normal vector on the body surface S. Eq.A.4.18 is the sixth boundary condition of the potential theory for rigid bodies which can be transformed to the following equation after separation of variables in eq.A.4.9:

$$\frac{\partial \varphi_{FK}}{\partial n} = -\frac{\partial \varphi_d}{\partial n} \tag{A.4.19}$$

Eq.A.4.19 is the so-called kinematic boundary condition on the body surface and makes the calculation of the space dependent term of the diffraction potential possible, since the respective incoming wave potential is well known from linear theory formulations (eq.A.1.16). With proper algebraic manipulations, namely Green's second theorem application in eliminating the diffraction potential term, the scatter wave load equals to the following:

$$F_{sc} = F_{FK} + F_d = -i\rho\omega e^{-i\omega t} \int \int_s (\varphi_{FK} \frac{\partial \varphi_{rad}}{\partial n} + \varphi_{rad} \frac{\partial \varphi_{FK}}{\partial n}) dS \tag{A.4.20}$$

Solving Potentials

The space-dependent part of the velocity potential φ_j ($j = 1..7$) as expressed in eq.A.4.9 at a point on the mean wetted surface of the body S_0 due to its motion in the radiation and diffraction modes can be represented by a continuous distribution of pulsating sources on the hull surface, also known as Green Function:

$$\varphi_j(x, y, z) = \frac{1}{4\pi} \int \int_{S_0} \sigma_j(\hat{x}, \hat{y}, \hat{z}) \, G(x, y, z, \hat{x}, \hat{y}, \hat{z}) \, dS_0 \, j = 1..7 \tag{A.4.21}$$

where:

- $\sigma_j(\hat{x}, \hat{y}, \hat{z})$ is the complex source strength in an arbitrary point $(\hat{x}, \hat{y}, \hat{z})$ on S_0 due to the body motion in the corresponding mode

- $G(x, y, z, \hat{x}, \hat{y}, \hat{z})$ is the Green's function of the source in an arbitrary point $(\hat{x}, \hat{y}, \hat{z})$ on the potential $\varphi_j(x, y, z)$ in a point located at (x, y, z), singular for $(\hat{x}, \hat{y}, \hat{z}) = (x, y, z)$ satisfying the linear potential theory assumptions (Laplace equation, seabed and free surface boundary conditions along with the radiation condition in the far-field)

The unknown source strengths $\sigma_j(\hat{x}, \hat{y}, \hat{z})$ are determined based on the normal velocity boundary condition (Journee, 2001):

$$\frac{\partial \varphi_j}{\partial n} = n_j = -\frac{1}{2}\sigma_j(x, y, z) + \frac{1}{4\pi} \int \int_{S_0} \sigma_j(\hat{x}, \hat{y}, \hat{z}) \, \frac{\partial G(x, y, z, \hat{x}, \hat{y}, \hat{z})}{\partial n} \, dS_0 \tag{A.4.22}$$

For the solution of the diffraction potential φ_7 the body surface kinematic boundary condition (eq. A.4.19) is employed.

System Response in Waves (Motion & Force RAO)

It is already mentioned that in an experimental setup, the researcher can specify the incoming wave characteristics (amplitude and frequency) and with proper devices the radiation and wave effect on the body (either in force or motion response) can also be determined. By choosing a wave of unitary amplitude and for a selected range of incoming frequencies, the motion and force transfer function of the body is specified for different headings. In that way, the Response Amplitude Operator (RAO) of the body in the frequency domain is a frequency inherent characteristic of the body which, if combined with the desired wave spectrum for different operations, will provide the motion/force responses for the particular sea state condition. First the wave elevation (eq.A.1.14), body oscillation and external force equations are expressed in complex notation and its real part is extracted:

$$\zeta(t) = Re\left\{\widetilde{\zeta}e^{-i\omega t}\right\} \tag{A.4.23}$$

$$F_o(t) = Re\left\{\widetilde{F_o}e^{F\zeta}e^{-i\omega t}\right\} \tag{A.4.24}$$

$$\xi(t) = Re\left\{\widetilde{\xi}e^{\xi\zeta}e^{-i\omega t}\right\} \tag{A.4.25}$$

Then the motion and force response amplitude operators for each degree of freedom expressed in the frequency domain (only space dependent part) are defined:

$$RAO_M = \frac{\widetilde{\xi}}{\widetilde{\zeta}}e^{\xi\zeta} \tag{A.4.26}$$

$$RAO_F = \frac{\widetilde{F_o}}{\widetilde{\zeta}}e^{F\zeta} \tag{A.4.27}$$

By equating the l.h.s of eq.A.4.8 and the r.h.s of eq.A.4.20, the *frequency-equation of motion* in matrix notation at the hydrodynamic reference frame is obtained:

$$-\omega^2 * [M^h + A^h(\omega)] * \widetilde{\xi} + \iota\omega C(\omega) * \widetilde{\xi} + K * \widetilde{\xi} = \widetilde{F_o} \tag{A.4.28}$$

A.5   Multibody Hydrodynamic Interaction

The multibody interactions of floating units in side-by-side operations is becoming a critical topic absorbing research attention by the industry and the offshore related academia. These interactions include the hydrodynamic coupling caused by the amplification of body wave fields when in close proximity and the mechanical coupling caused by the human intervention either with mooring lines or dynamic positioning for system station keeping or by the use of rigid-elastic connections between bodies for relative motion attenuation.

The hydrodynamic interaction of bodies is more complex and requires a full radiation-diffraction solution taking all bodies simultaneously into account; a laborious task which cannot be carried out analytically therefore the use of numerical solvers is necessary. On the other hand, the mechanical couplings can be introduced analytically in a straightforward manner by the use of kinematic constraints and implementing them to the derived equations of motion for the floating bodies, reducing the system's independent degrees of freedom. The equation of motion for multiple bodies is of the form:

$$\sum_{m=1}^{M}\{-\omega^2[M_{ij} + A(\omega)_{ij}] + i\omega[C_s + C(\omega)_{ij}] + K_{hyd} + K_s\}\xi_j = F_j + F_{ext} \qquad (A.5.1)$$

where M_{ij} is the body full mass matrix, $A(\omega)$ and $C(\omega)$ the hydrodynamic added mass and damping matrices as defined in eq. A.4.15-A.4.16, K_{hyd} is the hydrostatic body stiffness matrix and C_s, K_s are the damping and stiffness properties of the structural elements. Finally, the right hand side is the generalized force vector, consisting of the wave scatter force vector and the external force vector exerted to the system (mooring forces, dynamic positioning, actuation force etc.).

According to the excellent literature survey by Chen (2011), the term 'multibody' in hydrodynamics-related literature is used to describe the presence of two or more floating bodies in close proximity $(4 - 10[m])$. As explained above, one single rigid body in waves is excited due to incoming sea waves, whose components are diffracted due to the body presence and radiated due to body external excitation, all linearly superimposed under potential theory. In other words, each body in waves has a motion response defined by its unique, near wave field. Adding a second body in relevant proximity to the first, it is automatically exposed to the previously described wave field. As a result, the second body in turn reacts by generating its own radiation and diffracted waves. It is evident that these two wave fields are superimposed to create a new, complicated wave field which is amplified when compared to the initial wave fields. Therefore, the resulting body motions are significantly different from the motions of the single body and these responses are also heavily dependent on parameters like the wave directionality β (weather- and lee-ward bodies, exposed or shielded respectively by the environmental excitation), distance of bodies L_{gap}, their geometry dimensions and properties etc. The interaction between these floating structures is called hydrodynamic coupling. Due to the aforementioned assumptions, viscous effects are neglected and the multibody boundary value problem is readily solved in the potential theory framework, sometimes leading to unrealistic kinematics of the free surface in the gap between the bodies, a problem whose solution will be addressed later on.

The motion/force behavior of bodies in close proximity is given by the RAO in all 6 ridig body modes as described analytically in subsection A.4. For the scope of this exersice the hydrodynamic analysis of multi-body systems is restricted to frequency domain assuming linear system behavior:

- Linear potential wave theory

- Rigid floating bodies; no body deformations

- Quasi-static pretension before lift-off

- Viscous damping neglected

- Horizontal degrees of freedom (surge, sway & yaw) out of the final optimization scope; no mooring/dynamic positioning analysis for system station keeping is carried out

Therefore, although the radiation-diffraction problem is solved in full for all 6 rigid modes per body, the vertical degrees of freedom, namely heave, roll and pitch, will be the ones investigated in result postprocessing; in side-by-side offshore operations, the vertical relative motions between the bodies are the limiting operational and design criterion since these are strongly affected by the hydrodynamic coupling.

Additionally, the linear radiation-diffraction solvers tend to overestimate the resonant behavior of the free surface in the gap between the two vessels since the non-linear effects which in practice contribute to the dissipation of these extreme wave elevations are not taken into account. A lot of experimental studies and analytical approaches to that issue are carried out, especially in the past decade; to hold the free surface motion to a realistic level, Buchner et al. (2001) developed an analytical time-domain method based on visual observations from model testing by placing a rigid lid in the gap between the two bodies for the accurate calculation of the drift forces. Buchner also took the relative viscous damping into account for the correct prediction of the low-frequency motion response and finally used complete matrix of retardation functions (wave memory effect) for the correct estimation of heave and pitch motions. The unrealistic kinematics are supressed since it is impossible for the free surface to perturb when capped by a rigid lid, except the lid ends where noticeable free surface wave elevation due to diffraction was observed. Huijsmans et al. (2001) also contributed to that end by developing a robust linear potential solver for multibody systems by using the very same lid technique to circumvent unrealistic high water velocities on the ship's hull. The formulation of the 'rigid lid' approach to this problem is similar to the formulation to suppress irregular frequencies [Journèe and Massie (2001)].

Based on that novel approach, Newman (2003) introduces a flexible lid which allows the free surface to perturb under proper damping coefficient; that was possible by incorporating a set of generalized modes simulating the free surface elevation as the movement of a 'flexible mat' to the numerical scheme. All methods described above require the input of 'artificial' damping factors in order to surpress a numerical issue that was proven to occur by visual observation during model testing. Chen (2005) further proposed a linear dissipation term ε to modify the free surface equation. In the whole fluid domain an irrotational free damping force is introduced

$$F = \mu \nabla \Phi \qquad (A.5.2)$$

where μ is the damping parameter. By applying this damping force, the potentials are now only affected by the free surface boundary condition which is now transformed into:

$$\frac{\partial \varphi}{\partial z} - (1 - i\varepsilon)\frac{\omega^2}{g}\varphi = 0 \qquad (A.5.3)$$

where $\varepsilon = \mu/\omega$ is the nondimensional damping parameter. The selection of ε shall be chosen by comparing the numerical first or second order transfer functions to the experimental results. The conventional no-lid free surface kinematic boundary condition along with the rigid lid approach introduced first by Buchner and the damping lid approach by Chen are summarized in the table below.

Conventional	Rigid Lid [Buchner, Huijsmans]	Damping Lid [Newman, Chen]
-	Rigid	Semi-permeable
Undamped wave elevation	No wave elevation	Damped, tuned wave elevation
$\frac{\partial \varphi}{\partial z} - \frac{\omega^2}{g}\varphi = 0$	$\frac{\partial \varphi}{\partial n} = 0$	$\frac{\partial \varphi}{\partial z} - (1 - i\varepsilon)\frac{\omega^2}{g}\varphi = 0$

Table A.1: Free surface boundary conditions

Pauw et al. (2007) tried to determine a method of tuning ε to the case of side-by-side moored vessels in proximity by fitting the model basin results to the numerical model damped with proper ε. First, the free surface wave RAO in the gap between the vessels when fixed showed an interesting observation: superposition of incoming and diffracted waves result in cancellation in nodes at certain frequencies. This motion cancellation depends on the ratio between the gap dimensions (gap width in this case) and the wavelength. Figure A.5.1 shows the effect of wave cancellation at frequencies between $0.5 - 0.8[rad/s]$. Resonant peaks in the frequency range between $0.8 - 1.2[rad/s]$ are also observed; these are sloshing modes due to wave trapping in the gap. These resonances are attenuated in practice by viscous damping effects which cannot be captured by the linear radiation-diffraction solver; instead the nondimensional damping parameter ε is used to account for that effect. Secondly, it was observed that in the force RAO comparing the numerical and experimental results in the horizontal degrees of freedom, the calculated resonance peaks were not in line to the experimental ones, also due to the non-linear effect in the experimental results which is not captured by the solver.

(a) Wave motion RAO in gap for fixed vessels   (b) Experimental and numerical first order loads
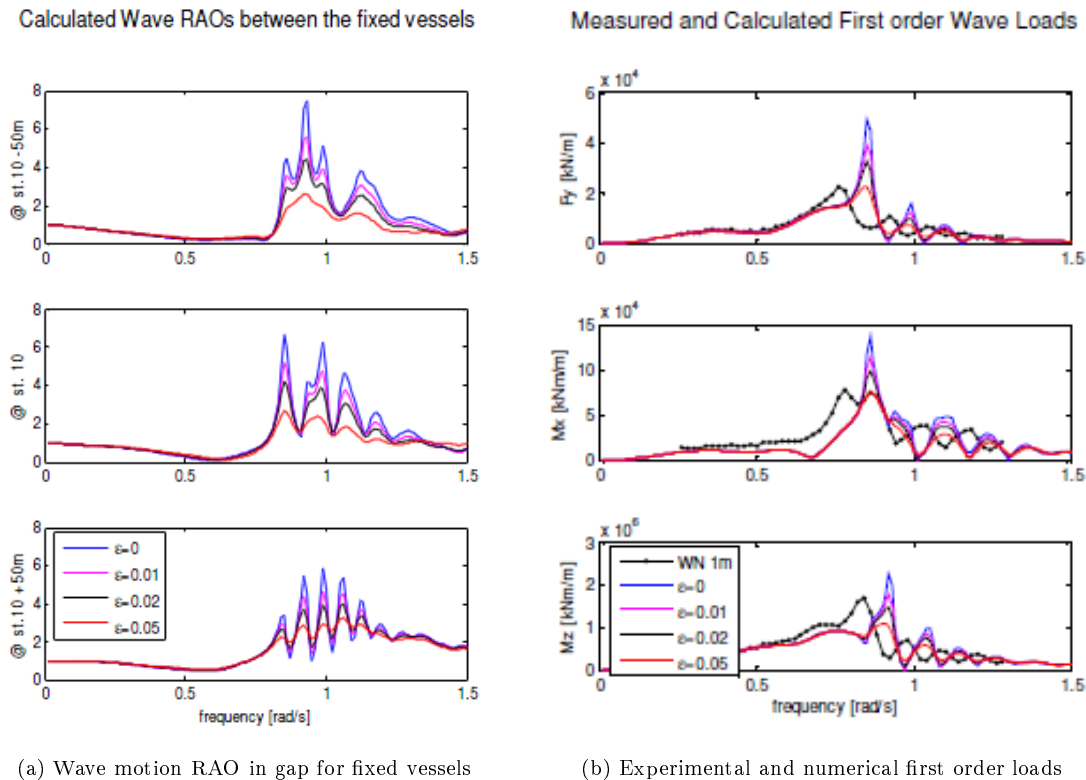
Figure A.5.1: Damping lid effect in gap between vessels (Pauw et al. (2007))

Conclusively, the hydrodynamic coupling of vessels in close proximity require a full three dimensional radiation diffraction solution in order to capture the complexity of the superimposed wave fields. However, special attention needs to be taken in the numerical output concerning the resonant peaks due to sloshing by the diffracted waves trapped in the gap by adding proper damping parameter to the free surface kinematic boundary condition. Since there is no universal method of tuning parameter ε, the computed results should be compared to exprimental observations and proper fitting should be carried out by employing various damping values. Only in case of large gap distances (higher than $25m$) it can be said that a unique value of ε can be determined [Fournier et al. (2006)].

A.6 Wave Effect Identification

The equation of motion for a rigid body under wave excitation has been expressed in frequency domain in eq. A.5.1. It is however necessary to express that very equation in a linear, state-space form for control design applications like the one investigated in this Thesis. The radiation-related part of the EOM has been derived by Cummins (1962):

$$[M + A]\ddot{x}(t) + \int_0^t K(t - \tau)\dot{x}d\tau + Cx(t) = F_{ext}(t) \tag{A.6.1}$$

where the convolution term denotes the fluid memory effect, i.e. the correlation of the fluid momentum gradient of subsequent time intervals. Ogilvie (1964) further elaborated on Cummins fluid memory EOM in the frequency domain using the Fourier Transform and deriving the added mass and damping matrices depending on the convolution integral as follows:

$$A(\omega) = A(\infty) - \frac{1}{\omega} \int_0^\infty K(t)\ sin(\omega\tau)\ d\tau \tag{A.6.2}$$

$$B(\omega) = \int_0^\infty K(t)\ cos(\omega\tau)\ d\tau \tag{A.6.3}$$

In turn the retardation function can be expressed in time domain by employing the inverse Fourier Transform

$$K(t) = \frac{2}{\pi} \int_0^\infty B(\omega)\ cos(\omega t)\ d\omega \tag{A.6.4}$$

or equivalently

$$K(t) = -\frac{2}{\pi} \int_0^\infty \omega(A(\omega) - A(\infty))\ sin(\omega t)\ d\omega \tag{A.6.5}$$

Finally the retardation function which describes the fluid frequency response is of the form

$$K(j\omega) = \int_0^\infty K(t)e^{-j\omega t}dt = B(\omega) + j\omega(A(\omega) - A(\infty)) \tag{A.6.6}$$

The numerical modeling and direct calculation of a convolution integral for high-order and multi degree of freedom systems is considered a laborious task so the investigation of an alternative representation of the convolution term has been extensively investigated. The option which facilitates the system control design of MIMO systems and therefore qualifies for the scope of this analysis is the convolution term replacement by an equivalent state-space model of the form

$$\dot{x}_r = A_r x_r + B_r \xi\ ;\ F_r = C_r x_r + D_r \xi \tag{A.6.7}$$

where x_r is the radiation internal state vector and A_r, B_r, C_r, D_r are the matrices that describe the LTI system. The radiation filter transfer function is assumed to be strictly proper (refer to subsection B.1) so $H_{rx}(j\omega) \to 0\ for\ \omega \to \infty$, corresponding to zero D matrix. The radiation problem identification is a Multiple-Input, Multiple-Output (MIMO) 6-input, 6-output closed-loop output feedback system consisting of each corresponding barge heave,roll and pitch radiation forces. In

principle, system pitch response is decoupled from the remaining two degrees of freedom and therefore the problem can be further simplified in two subproblems with state vector rank of 4 and 2, respectively. Both systems are identified via a system identification toolbox elaborated in-house by Shaofeng Wang as a part of his own Thesis research topic, in Python programming software.

Radiation

$$\dot{x_{r1}} = A_{r1}x_{r1} + B_{r1}\dot{\xi} \quad (heave - roll \ identification) \tag{A.6.8}$$

$$\dot{x_{r2}} = A_{r2}x_{r2} + B_{r2}\dot{\xi} \quad (pitch - pitch \ identification) \tag{A.6.9}$$

$$F_{R1} = C_{r1}x_{r1} \ ; \ F_{r2} = C_{r2}x_{r2} \tag{A.6.10}$$

$$F_R = (F_{Rz1}, M_{R\varphi1}, M_{R\theta1}, F_{Rz2}, M_{R\varphi2}, M_{R\theta2})^{\mathrm{T}} \tag{A.6.11}$$

Diffraction state-space model

$$\dot{z} = A_{d\eta}z + B_{dn}\eta \tag{A.6.12}$$

$$F_D = C_{d\eta}z + D_{dn}\eta \tag{A.6.13}$$

$$F_D = (F_{Dz1}, M_{D\varphi1}, M_{D\theta1}, F_{Dz2}, M_{D\varphi2}, M_{D\theta2})^{\mathrm{T}} \tag{A.6.14}$$

The

unknown state-space matrices are determined with system identification. The objective of a system identification method is to obtain the lowest-order possible that is able to produce the system behavior while maintaining stability of the resulting model (Taghipour et al. (2008)). The convolution term is thus replaced by alternative models based on the following types of data:

- Complex hydrodynamic coefficients $A(j\omega)$ and $B(j\omega)$

- The retardation functions $K(t)$ and its respective frequency response $K(j\omega)$

- The force-to-motion transfer function $H^{FM}(j\omega)$

Knowing the hydrodynamic added mass and damping transfer functions in frequency domain, the frequency-domain identification is thus chosen for the determination of the force-to-motion transfer function and the A, B, C, D state-space matrices.
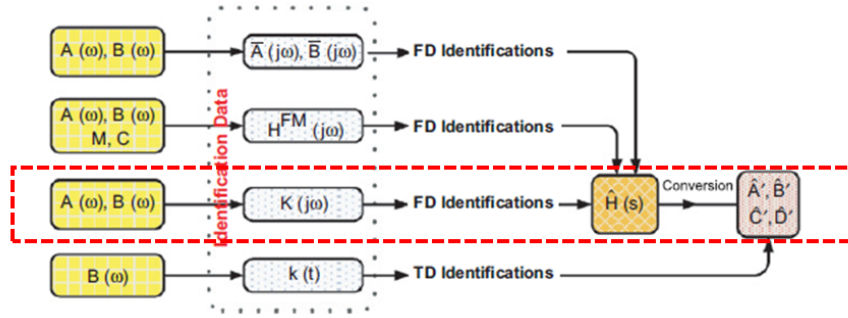
Figure A.6.1: Identification approaches Taghipour et al. (2008)

The properties of the retardation function $K(t)$ and its frequency response $K(j\omega)$ as summarized by Perez and Fossen (2008) and how these properties are implemented as constraints in the convex optimization process for the subspace system identification method of A,B,C,D used for this concept are excellently given in the work of (Wang (2015) - refer to Chapters 5-6). In an effort for maximum accuracy in the data fitting, Wang used the capacity threshold of 24 states of the convex optimization solver in the idetified state space model. As for the diffraction problem, it can be identified as an unconstrained (no fluid memory effect on this phenomena) Single-Input, Multiple-Output (SIMO) open-loop system where the wave elevation process $\eta(j\omega)$ is properly filtered providing a 6-state output force vector.

A.7   Wave Model Order Reduction

The maximum of 24 states per degree of freedom in the (radiation & diffraction) wave effect identification resulted in an accumulated wave model of 265 states. Additionally, the generalized plant describing the wave-barge-topside interaction also has filters for the wave elevation process (JONSWAP) spectrum, the structural closed-loop modeling the barge-link interaction and the output performance weight W_P, making the system cummulative state vector close to 300, which is considered techniqually infeasible for control system design purposes. Therefore, it is suggested that the fast modes of the state-space realization (MIMO singular values of lowest magnitude that affect less the system dynamics) to be taken out of the system. Given the fact that the H_∞ controller will be designed to have fixed-order and structure as it will be further described in Chapter B, the order of the open-loop plant model is reduced prior to the controller design. The model reduction problem as defined by Skogestad and Postlethwaite (2007) is that given a high order LTI stable model P, find a low-order approximation P_a such that the infinity norm of the difference $\|P - P_a\|_\infty$ is minimal and the error $P - P_a$ is stable. The balance residualization technique used will be presented herein.

(Minimal) Residualization

Assuming $(A, \ B, \ C, \ D)$ is a minimal state-space realization of a stable plant model $P(s)$, the aim is to distinguish the state vector x in two subvectors where the latter x_2 is the vector that contains the fast (high-frequecy) modes that will be removed. After the proper linear algebra the $A, \ B, \ C$ matrices are partioned into

$$\dot{x}_1 = A_{11}x_1 + A_{12}x_2 + B_1u$$
$$\dot{x}_2 = A_{21}x_1 + A_{22}x_2 + B_2u \qquad (A.7.1)$$
$$y = C_1x_1 + C_2x_2 + Du$$

By setting $\dot{x}_2 = 0$, thus residualizing state sub-vector x_2 and solving for x_2 and substituting the result of x_2 to the first equation, the resulting state-space representation and respective matrix minimal realization would be

$$\dot{x}_1 = (A_{11} - A_{12}A_{22}^{-1}A_{21})x_1 + (B_1 - A_{12}A_{22}^{-1}B_2)u \qquad (A.7.2)$$

$$y = (C_1 - C_2A_{22}^{-1}A_{21})x_1 + (D - C_2A_{22}^{-1}B_2)u \qquad (A.7.3)$$

$$A_r \triangleq A_{11} - A_{12}A_{22}^{-1}A_{21} \qquad (A.7.4)$$

$$B_r \triangleq B_1 - A_{12}A_{22}^{-1}B_2 \qquad (A.7.5)$$

$$C_r \triangleq C_1 - C_2A_{22}^{-1}A_{21} \qquad (A.7.6)$$

$$D_r \triangleq D - C_2A_{22}^{-1}B_2 \qquad (A.7.7)$$

The reduced order model $P_a(s) = (A_r, \ B_r, \ C_r, \ D_r)$ is the residualization of the original plant realization $P(s) = (A, \ B, \ C, \ D)$. An important property of residualization is that it preserves the steady-state system gain since the residualization process sets the x_2 vector derivatives to zero which are zero anyway at steady-state, making it clear that model reduction by residualization is more appropriate for low-frequency modeling (Skogestad and Postlethwaite (2007)).

Balanced Residualization

Using the same definition of minimal state-space realization as in subsection A.7, then (A, B, C, D) is a balanced realization if the solutions to the following Lyapunov equations

$$AP + PA^T + BB^T = 0 \tag{A.7.8}$$

$$A^T Q + QA + C^T C = 0 \tag{A.7.9}$$

are $P = Q = diag(\sigma_1, \sigma_2, ..., \sigma_n) \triangleq \Sigma$ where $\sigma_i, \ i = 1...n$, is a model singular value in descending order and P, Q are the controllability and observability Gramians defined as

$$P \triangleq \int_0^\infty e^{At} BB^T e^{A^T t} dt \tag{A.7.10}$$

$$Q \triangleq \int_0^\infty e^{A^T t} C^T C e^{At} dt \tag{A.7.11}$$

In a balanced realization each singular value is directly related to a state of the balanced system and the magnitude of σ_i is a measure of the contribution of the correspoding state x_i to the system transfer function behavior. Therefore by sorting the singular values in descending order and balancing the system making each system state as controllable as it is observable, the model reduction occurs be merely removing the states which have little effect on the system's input-output behavior Skogestad and Postlethwaite (2007). Assuming that the balanced realization (A, B, C, D) of $P(s)$ and the singular value diagonal Gramian matrix Σ are partitioned

$$A = \begin{bmatrix} A_{11} & A_{12} \\ A_{21} & A_{22} \end{bmatrix}; \ B = \begin{bmatrix} B_1 \\ B_2 \end{bmatrix}; \ C = \begin{bmatrix} C_1 & C_2 \end{bmatrix}; \ \Sigma = \begin{bmatrix} \Sigma_1 & 0 \\ 0 & \Sigma_2 \end{bmatrix} \tag{A.7.12}$$

where $\Sigma_1 = diag(\sigma_1, \sigma_2, ...\sigma_\kappa)$, $\Sigma_2 = diag(\sigma_{\kappa+1}, ...\sigma_n)$ for $\sigma_\kappa > \sigma_{\varkappa+1}$. In the exact fashion as in subsection A.7, the derivatives of the states corresponding to the Σ_2 are set to zero, yielding the balanced residualization of $P(s)$, in the exact same form as tabulated in eq. A.7.4-A.7.7.

A.8   Simulation in Wamit

Input files

- Potential Control File (.pot): the user specifies the operational water depth, whether both problems (radiation & diffraction) should be solved and which modes are free to vibrate or stay fixed; the modes which are defined as fixed produce a negative value in post-processed results which stand for the corresponding reaction forces & moments (Force RAO). Furthermore, the range of frequencies and wave headings are stated and finally the coordinates of the body (or bodies) with respect to the global coordinate system as shown in figure A.8.2.

```
! potential for A0 - no external stiffness - one barge
-1        HBOT
1 1       IRAD IDIFF
-91.         NFRE
0.2 0.02     FRE(1), increment
-19.         NBETA
0. 15.       BETA(1), increment
1       NBODY
zero.gdf
0. 0. 0. 0. XBODY
0 0 0 0 0 0 IMODE
```

Figure A.8.1: Potential file for 1 body run
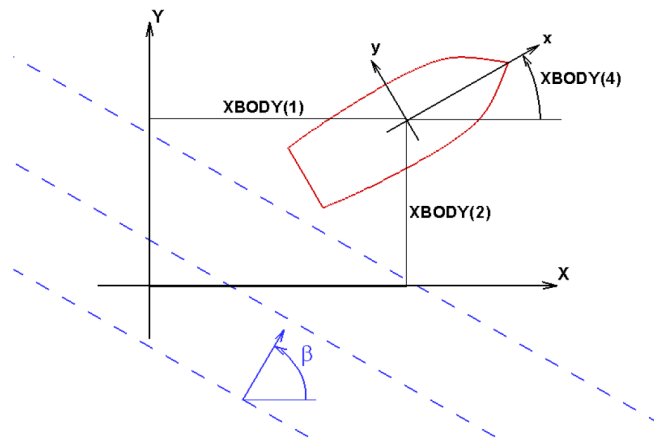
Figure A.8.2: Global & local body coordinates; wave heading angle definition

- Force Control File (.frc): the user specifies which are the desired outputs from the analysis. In the present case study the added mass and damping coefficients (.1) and body RAOs (.4) are requested as output. Furthermore, the inertia properties of bodies can be given as input through two different forms; either as a 3x3 diagonal radii of gyration matrix (per body) or as a 6x6 diagonal full mass matrix (again, per body). In every single run made for all case studies, the run was first performed with the first approach (alternative form 1) and subsequently

the full mass matrix was generated by solving the FORCE subprogram of Wamit (the mass matrix is given through .mmx output file).

```
! force file Alternative form 2 - no external stiffness - one barge
1 0 0 2 0 0 0 0 0                                      IOPTN(I)
1.0                                                    RHO
0.00 0.00 -0.1 0.00 0.00 -0.1                          XCG,YCG,ZCG
 1                                                     Mass
2.400000E+04, 0, 0, 0, -2.400000E+03, 0
0, 2.400000E+04, 0, 2.400000E+03, 0, 0
0, 0, 2.400000E+04, 0, 0, 0
0, 2.400000E+03, 0, 1.532162E+06, 0, 0
-2.400000E+03, 0, 0, 0, 1.832201E+07, 0
0, 0, 0, 0, 0, 1.937108E+07
 0                                                     Damping
 0                                                     Stiffness
 0                                                     NFIELD
 0                                                     XFIELD
```

Figure A.8.3: Force file alternative form 2 for 1 body run (mass in [tonnes])

Figure A.8.4: Full mass matrix (mass in [tonnes])

- Configuration File (.cfg): the user add any extra parameters that must be specified; which form of .frc file is being given as input, the input data for period or frequency range in the .pot file, the use of low-order or high-order panel method & the panel size concerning the body geometry etc.

```
! configuration for A0 - no external stiffness - one barge
ILOWHI=1
IALTFRC=2
ISOLVE=1
IPERIN=2
IPEROUT=2
PANEL_SIZE=8.25
TOLGAPWL=0.001
NCPU=4
RAMGBMAX=2
USERID_PATH=D:\WAMITV706  (directory for *.exe, *.dll, and userid.wam)
```

Figure A.8.5: Configuration input file for 1 body run

- Geometry Date File (.gdf): the user can describe the body geometry in four different ways, namely:

    - IGDEF=0: The geometry is a flat quadrilateral with patch coordinates issued in the gdf file explicitly. The low order panel method is utilized.
    - IGDEF=1: The patch geometry is represented by B-splines (high order panel method).
    - IGDEF=2: The geometry is given as input from a Multisurf[1] ($*.ms2$) file.
    - IGDEF>2: The geometry of each patch is represented explicitly by a special subroutine scripted in FORTRAN with optional data in the GDF file. In this case study the subroutine BARGE (IGDEF=-5) is utilized with two planes of symmetry (ISX=ISY=1) for the Castoro XI geometry specifications.

```
! geometry - no mooring stiffness - one barge
1 9.80665    ULEN GRAV
1 1          ISX ISY
3 -5         NPATCH IGDEF
1            NLINES
75.0    20.0    4.00     half-length, half-beam, draft
```

Figure A.8.6: Geometry input file for 1 body run

Output files

Several outputs can be generated by WAMIT and the user specifies the ones that are of importance during result post processing by other software. The default WAMIT output files consist of the formatted output file (*.out) which summarizes all input and output parameters of each run, the (*.mmx) file which summarizes the external full mass, stiffness and damping matrices of the system, the (*.hst) file to output values of the hydrostatic matrix and other .log files which contain remarks or pointing out potential errors during the run. For this case study, the user is also requesting the files (*.1) and (*.4) which output the radiation added mass and damping matrices for all input frequencies and headings and the motion/force RAO, respectively.

---

[1]http://aerohydro.com/?wpsc-product=multisurf-8-7-standard

Appendix B

Motion Control Design

This chapter aims to familiarize the reader with the fundamentals on the topics covered for the scope of this Thesis; in section B.1 the essential background on feedback control design which is provided, which is later refered to in the case studies implementation in Chapter 3. Section B.2 focuses on the H_∞ suboptimal controller synthesis for a standard problem; the convex H_∞ controller synthesis and the corresponding nonconvex, nonsmooth synthesis are presented successively in subsections B.2,B.2. Finally the concept of hybrid structural and control design as first introduced by Grigoriadis and Wu (1997) is presented in section B.3.

B.1 Feedback Control

Closed-loop Transfer Function

Before taking multiple-input-multiple-output (MIMO) systems into consideration, it is deemed neccessary to review a few fundamental concepts of classic feedback theory, well-proven for decades in the development of design techniques for single-input-single-output (SISO) feedback control systems, at least the ones who are thoroughly studied and utilized for the scope of this thesis exercise. A control system main objective is to shape the behavior of the system's output y by manipulating the plant G control input signal u. Thus, for a certain reference input r, the goal of a control engineer is to minimize the control error $e = y - r$; the algorithm for adjusting u based on the information fed back to the system is the controller K [Skogestad and Postlethwaite (2007)]. The major issue in feedback control consists in plant uncertainty; the models may change is course of time and therefore their deterministic modeling would be inaccurate, also affecting the feedback loop robustness. At this point it needs to be pointed out that the modeling process followed for this control system did not include uncertainty to its scope; thus no system robust stability and performance can be guaranteed. Conclusively, the terms nominal stability NS (stable with no model uncertainty) and nominal performance NP (system satisfying the performance criteria without model uncertainty included in design) will be used later on in this report.

Furthermore, the systems are identified and expressed in the linear, time-invariant state-space form

$$\dot{x} = Ax + Bu \tag{B.1.1}$$

$$y = Cx + Du \tag{B.1.2}$$

making extensive use of rational transfer functions G(s) of the form

$$G(s) = \frac{\beta_{n_z} s^{n_z} + ... + \beta_1 s + \beta_0}{s^n + a_{n-1} s^{n-1} + ... + a_1 s + a_0} \tag{B.1.3}$$

in frequency domain for the design of the system's building blocks (radiation & diffraction filters, barge, topside and link structural model, H_∞ controller), providing important advantages when compared to state space models, namely:

- Important concepts like transfer function peaks, roll-off frequency, phase margin, bandwidth etc. provide invaluable insight in the system's properties shaping process;

- $G(j\omega)$ is the the frequency response of the transfer function to a sinusoidal input of frequency ω;

- A system series interconnection in frequency domain is merely the mutliplication of the individual transfer functions, avoiding the laborious convolution integral analytical derivation required for systems expressed in time domain;

- System's fundamental properties (poles, gains & zeros) are explicitly evident via numerator-denominator factorization, helping into avoiding undesirable phenomena during transfer function shaping (zero-pole cancellation, closed-loop instability etc.).

For proper system with $n \geq n_z$ as defined below the transfer function can also be expressed as

$$G(s) = C(sI - A)^{-1}B + D \tag{B.1.4}$$

Definition 3.1 - Proper Transfer Function. A system $G(s)$ is called:

- Strictly proper if $G(j\omega) \to 0$ as $\omega \to \infty$

- Semi-proper or bi-proper if $G(j\omega) \to D \neq 0$ as $\omega \to \infty$

- A system G(s) either strictly or semi-proper is proper

- Improper if $G(j\omega) \to \infty$ as $\omega \to \infty$

Definition 3.2 - Frequency and bandwidth

- (Gain) crossover frequency: The frequency where the closed-loop frequency response $GK(j\omega)$ drops below the 1 *db* magnitude.

- (Phase) crossover frequency: The frequency where $GK(j\omega)$ phase plot crosses the -180 *deg*.

- Bandwidth ω_B: The frequency where $|S(j\omega)|$ first crosses 3 *db* from below, or equivalently,

- Bandwidth ω_{BT}: The highest frequency where $|T(j\omega)|$ crosses 3 *db* from above.

Evaluating Closed-Loop Stability & Performance

In principle, the implementation of high gains back to P may yield closed-loop instability; therefore one has to use high feedback gains over the frequency range where the control process aims at, while ensuring that the gains 'roll off' in higher frequencies so to avoid instability. The closed-loop design becomes more critical over the gain crossover frequency ω_c. Two methods are widely used to determine closed-loop stability:

- Closed-loop poles are evaluated either graphically or numerically; the system is stable if and only if all poles are lying in the left-half plane (the roots real part is always non-positive). Equivalently, the closed-loop PK poles are the state-space A matrix eigenvalues (matlab commands `damp` and `eig`, respectively).

- Use of Nyquist stability criterion upon which GK, when plotted in the complex plane, the number of open-loop unstable poles equals the number of contour encirclements around the critical point -1. In general, the closeness of the curve $GK(j\omega)$ to the point -1 in the complex plane is a good measure of how close a stable closed-loop system is to instability [Skogestad and Postlethwaite (2007)].

(a) closed-loop Pole Zero Plot   (b) closed-loop Nyquist Plot
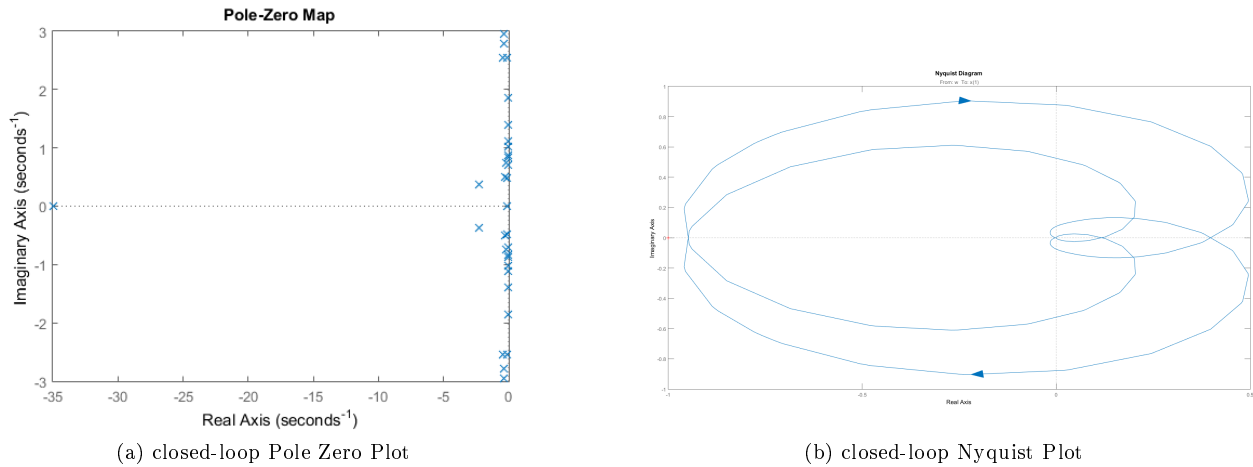
Figure B.1.1: Evaluating closed-loop Stability

Higher control gains in principle improve the system performance but as explained above, gains above a certain threshold induce instability. Therefore, the stability in the expense of system performance trade-off is subject to optimization for the control engineer. The measures of quantitative assessing performance are thus integral in the design of the system feedback properties are:

- Gain and phase margins: the gain margin is defined as the system gain obtained in between the gain and phase crossover frequencies (see fig. B.1.2) whereas the phase margin defined as the phase roll-off of the closed-loop frequency response in the same frequency range:

$$GM = \frac{1}{|GK(j\omega_{180}|} \qquad PM = \angle GK(j\omega_c) + 180^{0} \tag{B.1.5}$$
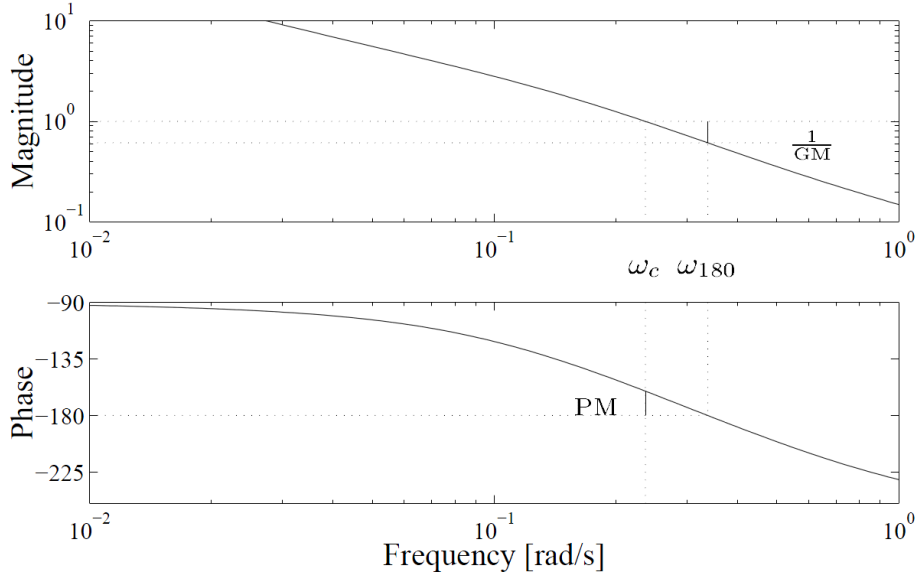
Figure B.1.2: Bode Plot of GK(jω) with gain and phase margin (GM & PM)

- Sensitivity (S) and complementary sensitivity (T) function peaks: For a closed-loop transfer function $GK(s)$ the following terminology is used in the control literature:

$$S = (I + GK)^{-1} \quad sensitivity \; function \tag{B.1.6}$$

$$T = (I + GK)^{-1}GK \quad complementary \; sensitivity \; function \tag{B.1.7}$$

where the S function is the forward transfer function from the disturbance to the output while T function is the closed-loop transfer function mapping the input reference signal to the output. It can be easily derived that:

$$S + T = I \tag{B.1.8}$$

which in practice means that their singular values difference should never exceed 1. The maximum S and T maximum peaks are defined as follows:

$$M_S = max_\omega \, |S(j\omega)| \quad M_T = max_\omega \, |T(j\omega)| \tag{B.1.9}$$

Large values of M_S or M_T are an indicator of system poor performance and therefore an upper bound for M_T is a common design specification in classic control applications. Similarly for M_S boundness, the S function is usually small at low frequencies but since proper plants are considered, GK should roll-off to 0 in higher frequencies or equivalently $S \rightarrow 1$. In the intermediate frequency range, it is unavoidable that $M_S > 1$ so a measure of system performance is how close to 1 is the M_S value. A typical requirement (but not a general rule) is that M_S shall be less than 2 (6 *db*) and M_T less than 1.25 (2 *db*). Conclusively, ω_B and ω_c

are good performance indicators and optimally S function shall be as close to 0 as possible at lower frequencies and close to 1 at intermediate frequencies.

Controller Design

The controller design methods can be distinguished in three basic designs: shaping of transfer functions, signal-based approach and numerical optimization. In the first approach, the designer specifies the transfer function allowable amplitudes in certain frequencies and shapes admissible controllers to reach that cause. It is a method that is based on the trial and error efforts of the control engineer who aims to obtain a closed-loop frequency response with the desirable properties. Therefore, loop shaping approach is a laborious task which is infeasible when considering complicated MIMO systems. As for the numerical optimization approach, the user tries to directly optimize the closed-loop transfer function by manipulating system properties like the rise time, stability margins etc. Computationally, such optimization problems may be difficult to solve, especially if one does not have convexity in the controller parameters; also including the system performance evaluation and controller design in a single-step procedure, the problem formulation is far more critical than in an iterative two-step approach [Skogestad and Postlethwaite (2007)].

The method mostly used in complicated MIMO plants, which is also employed in this exercise, is the signal based approach which involves the closed-loop system optimization via the minimization of the norm of a transfer function. This application considers a wave reference excitation and therefore the input signal is harmonic; so a signal-based H_∞ controller synthesis method has qualified as the appropriate closed-loop optimization method. This approach may also add model uncertainty for robust controller design, an application extension that would be of added value in possible follow-up research. The theoretical background on H_∞ controller synthesis is presented in section B.2.

The H_∞ controller design approach provide on hand all admissible (obeying to the engineer specifications on order and structure) controllers K that bring closed-loop stability under certain performance bound γ. Therefore, the only 'manual' task is the choice of proper weight functions to further shape the closed-loop transfer function behavior.

H_∞ Norm

By definition, the H_∞ of a scalar transfer function is the peak value of the system frequency response $|G(j\omega)|$

$$\|G(s)\|_\infty \triangleq max_\omega |G(j\omega)|$$

The 'infinite' symbol represents the maximum magnitude (singular value) over the frequency domain written as

$$max_\omega |G(j\omega)| = lim_{p\to\infty}(\int\limits_{-\infty}^{\infty} |G(j\omega)|^p \, d\omega)^{\frac{1}{p}}$$

and H stands for Hardy space [Zhou et al. (1996)]. H_∞ conclusively represents the set of stable and proper transfer functions with bounded infinite norm. In terms of performance, the H_∞

norm is the peak of the trasfer function magnitude and by introducing proper weights it can be interpreted as the magnitude of a closed-loop transfer function relative to a specified upper bound. The H_∞ norm is computed numerically from a state-space realization as the smallest value of γ such that the Hamiltonian matrix H has no eigenvalues on the imaginary axis where

$$H = \begin{bmatrix} A + BR^{-1}D^TC & BR^{-1}B^T \\ -C^T(I + DR^{-1}D^T)C & -(A + BR^{-1}D^TC)^T \end{bmatrix}$$ (B.1.10)

for $R = \gamma^2 I - D^T D$ [Zhou et al. (1996)]. This process shall be iterative when one may start with a large value of γ and reduce it until imaginary eigenvalues for H appear.

Weighted Sensitivity - Band Pass Filter

It has been concluded from subsection B.1 that the sensitivity function is a representative indicator of the closed-loop system performance; furthermore only magnitude of S function is relevant and not phase. The main specifications for the sensitivity function shall incorporate minimum bandwidth frequency ω_B and tracking error at selected frequencies, function shape over certain range and maximum peak magnitude as analyzed in subsection B.1 [Skogestad and Postlethwaite (2007)]. All these *loopshaping* specifications may be captured at once by proper definition of all these mixed sensitivity specifications.
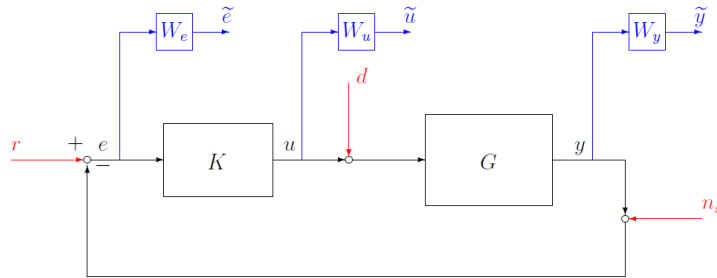
Figure B.1.3: closed-loop transfer function in standard block diagram form

Defining the standard control scheme in fig.B.1.3, featuring the open-loop system G, the controller K, the measured output y, the control signal u and the tracking error e. Red signals are inputs, n_s for noise, d for disturbance input and r for reference signal. The blue signals are properly weighted output signals namely $\tilde{e} = W_e e$, $\tilde{u} = W_u u$, $\tilde{y} = W_y y$. But what is the objective of these weight functions? For instance the transfer function W_e (or W_P in Skogestad and Postlethwaite (2007)) from reference r to error e

$$T_{re} = S = (I + GK)^{-1}$$ (B.1.11)

is a performance channel describing how fast the system follows the reference (tracking error); the W_P filter aims to minimize the infinite norm of the sensitivity function

$$|S(j\omega)| < 1/|w_P(j\omega)|, \ for \ \omega\epsilon(-\infty, \infty)$$

$$\Leftrightarrow |w_P S| < 1, \; for \; \omega \epsilon (-\infty, \infty)$$

$$\Leftrightarrow \|w_P S\|_\infty < 1 \tag{B.1.12}$$

The transfer function W_u from reference r to control signal u

$$T_{ru} = KS = K(I + GK)^{-1} \tag{B.1.13}$$

is a 'penalty' filter on the control effort exerted on the system (usually a scalar is used in practice). Finally by penalizing the output signal, an upper bound is enforced on the desired bandwidth while simultaneously specifying other closed-loop system performance properties like the steep roll-off in high and low frequency bandwidth. To do that the transfer function W_y(or W_T in Skogestad) is used to the mapping from reference r to output signal y

$$T_{ry} = T = GK(I + GK)^{-1} \tag{B.1.14}$$

Any of the aforementioned performance weights shape depend on the application requirement; essentially setting up a performance bound to any channel at a certain point of the system (reference to error, reference to output etc.) could be practically interpreted as setting a 'penalty' on undesirable behavior of the closed-loop transfer function. For instance, if low-frequency activity is required a high pass filter is used; in order to provide better roll-off in higher frequencies a low pass filter is employed. However, there are cases where both low- and high-frequency activity needs to be rejected. By cascading a single low and a high pass filter, a new filter is created which passes only a selected range or band of frequencies while attenuating all the others.

$$High \; Pass \; Filter: \; \frac{s^2 + 2\omega_H \zeta_H s + \omega_H^2}{s^2 + 2\omega_H^* \zeta_H^* s + \omega_H^{2*}} \; ; \; Low \; Pass \; Filter: \; \frac{\omega_L^2}{s^2 + 2\omega_L \zeta_L s + \omega_L^2} \tag{B.1.15}$$

$$Band \; Pass \; Filter: \; \frac{s}{s^2 + 2\omega_B \zeta_B s + \omega_B^2} \tag{B.1.16}$$

where ω is the bandwidth frequency and β the damping ratio used. If further performance improvement is needed, a higher order filter is required so to achieve a steeper slope. To properly adress and combine all specifications at once with the H_∞ framework, a mixed-sensitivity approach is followed where the overall optimization criterion can be expressed as follows

$$\|T\|_\infty = max_\omega \bar{\sigma}(N(j\omega)) < 1 \; ; \; N = \begin{bmatrix} W_P S \\ W_u KS \end{bmatrix} \tag{B.1.17}$$

In an effort to visualize the generalized setting of such system, the mixed-sensitivity problem can be expressed as in the figure below, where a single exogenous input exists and defining an output vector $z = [z_1 \; z_2]^T$, where $z_1 = W_p y$ is the shaped by band-pass filter W_P reference tracking signal and $z_2 = W_u u$ the shaped control signal. The augmented generalized plant $P(s)$ now becomes

$$\begin{bmatrix} z_1 \\ z_2 \\ v \end{bmatrix} = \begin{bmatrix} W_p & -W_p G \\ 0 & W_u \\ I & -G \end{bmatrix} \begin{bmatrix} w \\ u \end{bmatrix} \tag{B.1.18}$$
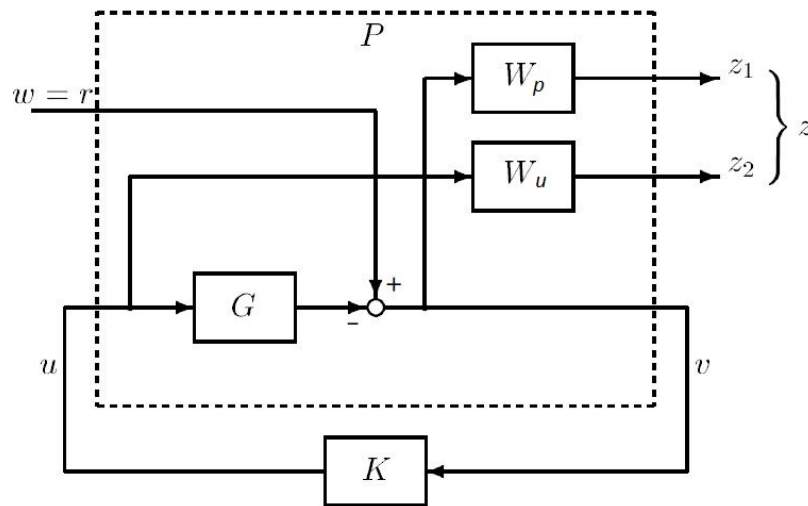
Figure B.1.4: S/KS mixed sensitivity minimization in Standard Form

The weights are now the tuning parameters, meaning that the system performance according to the desired specifications requires some hand tuning of the weight coefficients. Similarly, an S/KS/T mixed cost function can be defined in the same context in case that reference tracking is also desired, an S/T stacked approach when the control effort is not required to be bounded etc. It has to be noted that by adding cost functions to the stacked approach, the shaping of the closed-loop transfer function becomes more difficult to converge to a local solution mainly because of the design trade-offs that have to be made simultaneously.

B.2 H_∞ Control

Introduction

The first paper upon which the later work on the H_∞ framework based to came by Zames (1981); a state-space formulation of H_∞ optimal control theory in an input-output setting. In 1984, Doyle 'solved' the H_∞ problem focusing on 2 x 2 block problems but the problem was casted in several algebraic Ricatti equations (ARE) of increasing dimension, adding the complexity of computation even for small problems. Limebeer and Halikias (1988) later showed that, for problems transformable to 2 x 1 problems, a minimal realization of the controller has state dimension no greater than that of the generalized plant P, introducing the idea that there may exist optimal controllers of lower dimension for multivariable system case studies. Doyle et al. (1989) derived simple state-space formulas for all controllers solving the 'simple' case of H_∞ problem. He showed that for a given performance vector $\gamma > 0$, a controller exists if and only if the unique stabilizing solutions to two algebraic Riccati equations (ARE) are positive definite and the spectral radius of their product is less than γ^2. Zhou and Khargonekar (1988) showed that the H_∞ norm of the closed-loop transfer function can be completely casted within one algebraic Riccati equation; he was also the first to solve the H_∞ optimization problem by introducing static (zero order) gains to the state feedback law. A new approach in control design was suggested by Gahinet and Apkarian (1994) who based his solution on the linear matrix inequalities (LMI) framework, reducing the problem formulation to one inequality. Unfortunately, all aforementioned approaches (ARE, LMI) of solving the problem between the 80's up until early '00s lead to full order, convex, 'unstructured' controllers; the significant computational effort required made it infeasible for these premature *optimization* solutions to be implemented in practice to the control industry, which prefers 'simple' *tuning* control solutions like PIDs or control architectures combining PIDs with performance filters which are structured.

Definition 4.3

A controller K of the form (state-space and matrix form):

$$K : \left\{ \begin{array}{l} \dot{x_k} = A_k x_k + B_k y \\ u = C_k x_k + D_k y \end{array} \right. \; ; \; K(s) = \left[\begin{array}{cc} A_k & B_k \\ C_k & D_k \end{array} \right] \tag{B.2.1}$$

is called *structured* if the state-space matrices A_k, B_k, C_k, D_k depend smoothly on a design parameter vector θ varying in its parameter space R^n or a constrained subset of R^n, where θ denotes the vector of free tunable parameters.

The main problem that arises when constraining the structure and order of the controller is that the optimization problem becomes nonconvex and NP (nondeterministic polynomial time),van Solingen et al. (2014). Several approaches for fixed-structure controller design has emerged since the bilinear matrix inequality (BMI) techniques are used in conjuction with nonsmooth cost functions minimization by Apkarian and Noll (2006) being the one presented in this Thesis.

H_∞ General Control Problem Formulation

It would be quite useful to have a generic standardized problem formulation upon which all optimization problems can be casted. The H_∞ problem can then be stated as follows: given a real rational transfer matrix $P(s)$ called the generalized plant, determining the forward mapping be-

tween the weighted exogenous inputs (w) and outputs (z) to manipulated control signals (u) and sensed outputs (v) which interconnect the plant with the controller $K(s)$ as defined in eq. B.2.1. The closed-loop system is optimized so to find all the admissible controllers K as follows
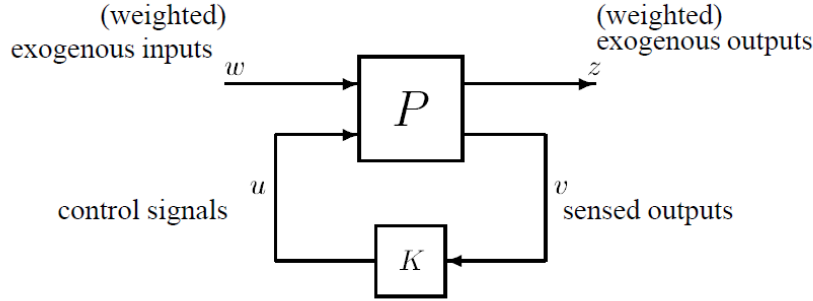

Figure B.2.1: General control configuration (no model uncertainty)

Optimal H_∞ Control: Find the (solution space of) all admissible controllers $K(s)$ such that the highest singular value in the forward LFT (refer to Appendix A - B.4) mapping from w to z $\|T_{zw}\|_\infty$ is minimized, where the objective function is the lower LFT

$$T_{wz}(s) = F_l(P, K) = P_{11} + P_{12}K(I - P_{22}K)^{-1}P_{21}, \tag{B.2.2}$$

In theory, an optimal solution space subject to prescribed parameter boundaries is all a researcher should ultimately aim at. For instance, in subsection 3.1, an optimal H_∞ controller is calculated for the recreation of the case study formulated in the works of Camino et al. (2003) and the possibility of a joint structural-control design framework is investigated. In practice however, a solution via optimal H_∞ controller synthesis is unique in MIMO systems and is considered to be an "expensive" solution both in modeling and numerical implementation. On the other hand, a controller that provide internal stability and output performance below a certain upper bound γ is a more efficient approach which sometimes provide a controller with better properties (e.g. lower bandwidth, quicker roll off in high frequency band).

Sub optimal H_∞ Control: For some prescribed constant γ for the system output performance, find all admissible controllers $K(s)$ under which

$$\|T_{zw}\|_\infty < \gamma$$

$$subject\ to \quad K\ stabilizes\ P\ internally \tag{B.2.3}$$

$$K \ \epsilon \ K\kappa$$

The plant $P(s)$ has a state-space and matrix representation of the form

$$P: \quad \begin{cases} \dot{x} = Ax + B_1w + B_2u \\ z = C_1x + D_{11}w + D_{12}u \\ y = C_2x + D_{21}w + D_{22}u \end{cases} ; \ P(s) = \begin{bmatrix} A & B_1 & B_2 \\ C_1 & D_{11} & D_{12} \\ C_2 & D_{21} & D_{22} \end{bmatrix} \tag{B.2.4}$$

where $x \,\epsilon\, R^{n_p}$ is the system states, $u \,\epsilon\, R^{n_u}$ the control states, $y \,\epsilon\, R^{n_y}$ the measured output, $w \,\epsilon\, R^{n_w}$ the exogenous input and $z \,\epsilon\, R^{n_z}$ the regulated output. As soon as $D_{22} = 0$, the closed-loop transfer objective function has the state-space representation

$$T_{wz} = \left[\begin{array}{cc} A(K) & B(K) \\ C(K) & D(K) \end{array} \right] \tag{B.2.5}$$

and the state dimension of the interconnected closed-loop transfer function is $n_p + k$. When working in the convex framework (K_{full}: full-order controllers) the total order would be $N :=$ $n_p^2 + n_p(n_y + n_u) + n_y n_u$, making the solution process relatively 'easy' (essentially convex), however making the K_{full} infeasible to handle in practice. When smaller (fixed-structure and fixed-order) controller spaces are required the problem in eq.B.2.3 becomes 'harder' (nonconvex and sometimes NP) to solve. For the sake of completion, both the convex solution as given by Doyle et al. (1989); Zhou et al. (1996) solved in the ARE and LMI framework, respectively, and the nonconvex, nonsmooth approach by Apkarian and Noll (2006) are described; the latter will be essentially adopted and implemented in this assignment's application through a script employing the function `hinfstruct` based on that very work by Apkarian, Noll and Gahinet, available in Matlab Robust Control Toolbox.

Convex H_∞ Synthesis

Assumptions on P

This section presents the assumptions taken on the generalized plant P defined in eq. B.2.4 that will be used in the H_∞ control case and how does the the K matrix is being derived so to minimize T_{wz}. K is constrained so to provide internal stability, meaning that states of P and K go to zero when the exogenous input $w = 0$. The assumptions that K is proper, real, rational transfer function, detectable and stabilizable is assumed throughout these two subsections; therefore by using the term 'controller' it means that these properties are always fulfilled. This is the definition of an admissible controller as given by Zhou et al. (1996) (refer to Lemma 16.1, p.415). The realization of the generalized plant P for the 'simple' H_∞ case is of the form:

$$P := \begin{bmatrix} A & B_1 & B_2 \\ C_1 & 0 & D_{12} \\ C_2 & D_{21} & 0 \end{bmatrix} \tag{B.2.6}$$

The following assumptions are made in the H_∞ problem:

1. $(A,\ B_1)$ is stabilizable and (C_1, A) is detectable

2. (A, B_2) is stabililizable and (C_2, A) is detectable

3. D_{12} and D_{21} have full rank

4. $\begin{bmatrix} A - j\omega I & B_2 \\ C_1 & D_{12} \end{bmatrix}$ has full column rank for all ω

5. $\begin{bmatrix} A - j\omega I & B_1 \\ C_2 & D_{21} \end{bmatrix}$ has full row rank for all ω

6. $D_{12}^T[C_1\ \ D_{12}] = [0\ \ I]$ and $[B_1\ \ D_{21}]^T D_{21}^T = 0$

Assumption [1] along with [2] guarantees that the two Hamiltonian matrices (H_∞ and J_∞ for the H_∞ problem) belong to $Dom(Ric)$ (refer to Appendix A - B.4). This assumption simplify the problem statements and proofs but if it is relaxed it can be properly modified so to still stand correct. An important simplification that comes from [1] is that internal stability is equivalent to input-output stability ($T_{wz}\ \epsilon\ \mathbb{RH}_\infty$). Assumption [2] is necessary and sufficient for P to be internally stabilizable, but not needed to prove the equivalence of internal stability and $T_{wz}\ \epsilon\ \mathbb{RH}_\infty$ [Doyle et al. (1989)]. Supposing that assumptions [1],[2] and [6] simultaneously hold then the controller K is admissible if $T_{wz}\ \epsilon\ \mathbb{RH}_\infty$ [Zhou et al. (1996)]. Assumption [3] is sufficient to ensure that the controllers are proper and hence realizable. Assumptions [4], [5] ensure no zero-pole cancellations on the imaginary axis which in turn cause closed-loop instability. Two additional assumptions that are implicit in the assumed realization for $P(s)$ are that $D_{11} = D_{22} = 0$. By relaxing these formulas and especially D_{11}, the formulas are getting substantially more complicated.

H_∞ suboptimal case

The problem considered is already presented in subsection B.2: find all admissible K so that $\|T_{zw}\|_\infty < \gamma$. Let $\gamma_{min} := min\{\|T_{zw}\|_\infty : K(s)\ \ admissible\}$ be the optimal system performance

level. By definition $\gamma > \gamma_{min}$ in order for suboptimal controllers to exist. The H_∞ solutions involve the Hamiltonian matrices

$$H_\infty = \begin{bmatrix} A & \gamma^{-2}B_1B_1^T - B_2B_2^T \\ -C_1^TC_1 & -A^T \end{bmatrix} \;;\; J_\infty = \begin{bmatrix} A^T & \gamma^{-2}C_1^TC_1 - C_2^TC_2 \\ -B_1B_1^T & -A \end{bmatrix} \quad \text{(B.2.7)}$$

The important difference when compared to the general H_2 case is that the $(1,2)$-blocks are not sign definite so it is not guaranteed that $H_\infty \in Dom(Ric)$ or $Ric(H_\infty) \geqq 0$. It needs to be noted that by using the term $(1,2)$- blocks a combination of the expressions from the H_∞ norm and the H_2 synthesis definition [Zhou et al. (1996)] is meant. This can be solved using the algorithm of [Doyle et al. (1989)]:

Theorem 4.1: H_∞ suboptimal control
There exists an admissible controller such that $\|T_{zw}\| < \gamma$ if the following conditions hold

1. $H_\infty \in Dom(Ric)$ and $X_\infty \geqq 0$ is a solution to the ARE

$$A^TX_\infty + X_\infty A + C_1^TC_1 + X_\infty(\gamma^{-2}B_1B_1^T - B_2B_2^T)X_\infty = 0 \quad \text{(B.2.8)}$$

   such that $Re\{j\omega_i[A + (\gamma^{-2}B_1B_1^T - B_2B_2^T)X_\infty]\} < 0$, *for all i*

2. $J_\infty \in Dom(Ric)$ and $Y_\infty \geqq 0$ is a solution to the ARE

$$AY_\infty + Y_\infty A^T + B_1B_1^T + Y_\infty(\gamma^{-2}C_1^TC_1 - C_2^TC_2)Y_\infty = 0 \quad \text{(B.2.9)}$$

   such that $Re\{j\omega_i[A + Y_\infty(\gamma^{-2}C_1^TC_1 - C_2^TC_2)]\} < 0$, *for all i*

3. $\rho(X_\infty Y_\infty) < \gamma^2$

Moreover, when these conditions hold, all admissible controllers are then given by $K = F_l(K_c, Q)$ where

$$K_c(s) = \begin{bmatrix} A_\infty & -Z_\infty L_\infty & Z_\infty B_2 \\ F_\infty & 0 & I \\ -C_2 & I & 0 \end{bmatrix} \quad \text{(B.2.10)}$$

$$F_\infty = -B_2^TX_\infty \;,\; L_\infty = -Y_\infty C_2^T \;,\; Z_\infty = (I - \gamma^{-2}Y_\infty X_\infty)^{-1} \quad \text{(B.2.11)}$$

$$A_\infty = A + \gamma^{-2}B_1B_1^TX_\infty + B_2F_\infty + Z_\infty L_\infty C_2 \quad \text{(B.2.12)}$$

and $Q(s)$ any stable, proper transfer function such that $\|Q\|_\infty < \gamma$. For $Q(s) = 0$ it holds that

$$K(s) = K_{C11}(s) = -F_\infty(sI - A_\infty)^{-1}Z_\infty L_\infty \quad \text{(B.2.13)}$$

This is the 'central' controller that has the same order (number of states) as the generalized plant $P(s)$

Nonconvex, Nonsmooth H_∞ Synthesis

Nonconvex H_∞ Control Problem Statement

The convex controller synthesis method which was investigated and ultimately solved between late 80's to mid-90's provided *unstructured* controllers whose order was at best equal to those of the generalized plant, making it impossible to be implemented in practice for medium to large scale systems (the state space model describing the hydrodynamic loading of coupled barges alone, examined in Chapter 3 has state order of 265 if no model reduction techniques are applied - also refer to section A.7). This incompatibility between H_∞ theory and control engineering practice is highlighted by the extensive use of control *tuning* techniques, i.e. PID control. Therefore, the controller design techniques based on linear matrix inequalities (LMI) and algebraic Ricatti equations (ARE) may provide sound controllers which are however unstructured and thus inapplicable in practice. The need to optimize fixed-structure feedback controllers with the possibility to also address challenging design problems, e.g. static/fixed-order, decentralized control, optimization of PID control, simultaneous design and stabilization problems etc., emerged the investigation of H_∞ synthesis via bilinear matrix inequalities (BMIs) which are by definition nonconvex problems.

Computing a reduced fixed-order H_∞ controller is significantly more complicated than computing the full-order controller. Assuming the order of controller K to be fixed at $k < n_p$, where n_p is the number of states of the generalized plant P. This controller would have the following structure:

$$K_\kappa = \{K : \ K \ as \ in \ B.2 \ with \ size(A_K) = \kappa \ x \ \kappa\}$$

The vector of tunable elements is $\theta = (vec(A_k), vec(B_k), vec(C_k), vec(D_k))$ of total dimension $n = k^2 + k(n_y + n_u) + n_y n_u$. This structure is obviously of lower order when compared to the full-order controller which has $n_{full} = n_p^2 + n_p(n_y + n_u) + n_y n_u$ tunable elements. By considering the lower-order model, instead of solving two decoupled Ricatti equations (eq. B.2.8,B.2.9), four coupled Riccati equations need to be solved; a task which is already formulated. One therefore obtains an LMI coupled with a rank constraint, a nonconvex problem which is equivalent to a BMI.

Nonsmooth Optimization

Optimization code for BMI problems has been developed by several groups; the novel work of [Apkarian and Noll (2006)] will be presented herein and cited throughout this report. Apkarian has concluded that the BMI approach runs into numerical difficulties even for moderate size problems (described by less than 100 states). This is mainly due to the presence of Lyapunov variables whose number grow quadratically with the number of states implemented. He thus came up with an approach which do not employ Lyapunov variables, leading to moderate size optimization even for large scale problems (order of several hundreds of states). This approach comes at the expense of defining nonsmooth cost functions which require special optimization techniques.

Nonsmooth optimization of the H_∞ norm

Assuming that fixed-structure controller is affine to parameter $\theta \, \epsilon \, R^n$, the closed-loop transfer function T_{wz} has the following representation:

$$T_{wz}(P, K(\theta)) := \left[\begin{array}{cc} A(K(\theta)) & B(K(\theta)) \\ C(K(\theta)) & D(K(\theta)) \end{array} \right]$$

The suboptimal H_∞ control problem (eq.B.2.3) then becomes

$$f(\theta) := \|T_{wz}(P, K(\theta))\|_\infty = max_\omega \bar{\sigma}(C(K(\theta))(j\omega I - A(K(\theta)))^{-1}B(K(\theta)) + D(K(\theta))) \quad \text{(B.2.14)}$$

a nonsmooth, nonconvex function. Its domain $D_f = \{\theta \, \epsilon \, R^n : \, f(\theta) < \infty\}$ contains the internally stabilizing set

$$D_s = \{\theta \, \epsilon \, R^n : \, K(\theta) \text{ stabilizes } P \text{ internally}\}$$

The H_∞ controller is synthesized via the Hamiltonian bisection algorithm, further used to characterize and compute the Clarke subdifferential of f function. This allows to formulate necessary optimality conditions which are in turn used to compute descent steps, a novel method by [Apkarian and Noll (2006)] to characterize locally optimal solutions of eq.B.2.3. In an effort to reduce the literature complexity to the absolute essentials, the analytical formulation of the first-order nonsmooth algorithm is not presented and one shall be refered to section VI of the seminal paper.

Subdifferential of H_∞ Norm   The method formulation begins by characterizing the subdifferential of the H_∞ norm and deriving the expressions for the Clarke subdifferential of several nonconvex functions $f(x) = \|G(x)\|_\infty$, where G is a smooth operator defined on R^n space. Considering the well-known H_∞ norm of G transfer function $\|G\|_\infty = max_\omega \bar{\sigma}(G(j\omega))$ with G stable, let $G(j\omega) = U\Sigma V^H$ be the singular value decomposition of the transfer function. By picking e.g. u to be the first column of U and v the first column of V, that is, $u = G(j\omega)v/\|G\|_\infty$. Then the linear functional $\varphi = \varphi_{u,v,\omega}$ defined as follows

$$\varphi(H) = Re\{u^H H(j\omega)v\}$$

$$= \|G\|_\infty^{-1} Re\{Tr[vv^H G(j\omega)^H H(j\omega)]\} \quad \text{(B.2.15)}$$

$$= \|G\|_\infty^{-1} Re\{Tr[G(j\omega)^H uu^H H(j\omega)]\}$$

continuous on H_∞ space of stable transfer functions and a subgradient of $\|.\|_\infty$ at G. Assuming that the columns of Q_u form an orthonormal basis of the eigenspace of $G(j\omega)G(j\omega)^H$ associated with the largest eigenvalue

$$\lambda_1(G(j\omega)G(j\omega)^H) = \bar{\sigma}(G(j\omega))^2 \quad \text{(B.2.16)}$$

and that the columns of Q_v form an orthonormal basis of the eigenspace of $G(j\omega)^H G(j\omega)$ associated with the same eigenvalue, then for all complex Hermitian matrices $Y_u, Y_v \, \epsilon \, B$ holds that,

$$\varphi(H) = \|G\|_\infty^{-1} Re\{Tr[Q_v Y_v Q_v^H G(j\omega)^H H(j\omega)]\} \quad \text{(B.2.17)}$$

$$\|G\|_\infty^{-1} Re\{Tr[G(j\omega)^H Q_u Y_u Q_u^H H(j\omega)]\}$$

a subgradient of $\|.\|_\infty$ at G. Finally, with $G(s)$ rational and assuming there exist finitely many frequencies where $\|G\|_\infty = max_\omega \bar{\sigma}(G(j\omega))$ holds, all subgradients are of the form

$$\varphi(H) = \|G\|_\infty^{-1} Re\{\sum Tr[G(j\omega)^H Q_v Y_v Q_v^H H(j\omega)]\} \tag{B.2.18}$$

Assuming now that G_s is a smooth operator mapping into the H_∞ space of stable transfer functions G, the composite function $f(x) = \|G(x)\|_\infty$ is Clarke differentiable at x with

$$\partial f(x) = G_s^{'} * [\partial \|.\| (G_s(x))] \tag{B.2.19}$$

where $\partial \|.\|_\infty$ is the subdifferential of the H_∞ norm, and where $G_s^{'}$ is the adjoint of G_s.

Clarke Subdifferentials in Closed-Loop   Moving forward in formulating the Clarke subdifferentials in closed-loop transfer function and using the known generalized plant P partition

$$P(s) := \left[\begin{array}{cc} P_{11}(s) & P_{12}(s) \\ P_{21}(s) & P_{22}(s) \end{array} \right] \tag{B.2.20}$$

our aim is the subdifferential $\partial f(K)$ of $f := \|.\|_\infty o\ T_{wz}$ at K. The derivative of the closed-loop forward mapping would be of the form

$$T_{wz}^{'}(K)\delta K := G_{12}\delta K G_{21}$$

where δK is an element of the same matrix space as K and with the definitions

$$\left[\begin{array}{cc} T_{wz}(K,s) & G_{12}(K,s) \\ G_{21}(K,s) & * \end{array} \right] := \left[\begin{array}{cc} P_{11} + P_{12}K(I - P_{22}K)^{-1}P_{21} & P_{12}(I - KP_{22})^{-1} \\ (I - P_{22}K)^{-1}P_{21} & * \end{array} \right] \tag{B.2.21}$$

and the closed-loop state space data

$$A(K) := A + B_2KC_2 \quad B(K) := B_1 + B_2KD_{21}$$

$$C(K) := C_1 + D_{12}KC_2 \quad D(K) := D_{11} + D_{12}KD_{21} \tag{B.2.22}$$

Now let $\varphi = \varphi_Y$ be a subgradient of $\|.\|_\infty$ at T_{wz} of the form (eq. B.2.17) and with $\|T_{wz}(K)\|_\infty$ attained at frequency ω. According to the chain rule, the subgradients Φ_Y of f at K are of the form $\Phi_Y := T_{wz}^{'}(K) * \varphi_Y \epsilon\ M_{m2,p2}$. Consequently, for a static K, the Clarke subdifferential of $f(K) := \|T_{wz}\|_\infty$ at K consists of all subgradients Φ_Y of the form

$$\Phi_Y = \|T_{wz}(K)\|_\infty^{-1} Re(G_{21}(K,j\omega)T_{wz}(K,j\omega)^H QYQ^H G_{12}(K,j\omega))^T \tag{B.2.23}$$

Φ_Y is now an element of the same matrix space as K and acts on test vectors δK through $\prec\Phi_Y, \delta K\succ = Tr(\Phi_Y^T \delta K)$. Expression B.2.23 is generic and can be implemented to problems of practical interest. For instance, this theory is going to be used for decentralized control, i.e. all controller gains in the diagonal are freely parameterized whereas the off-diagonal terms are zero. Considering a pattern matrix W with binary structure where $W_{ij} = 0$ when the controller gain is off-diagonal and fixed and where $W_{ij} = 1$ for i=j, the Clarke subdifferential of $f = \|.\|_\infty oF$ at K is then of the form

$$W \odot \Phi_Y$$

where $\Phi_Y \epsilon \partial \|.\|_\infty (F(K))$ and where symbol $\odot$ stands for Schur's product.

Descent Method   Considering the problem of minimizing $f(x) = \|G_s(x)\|_\infty$, a necessary condition for optimality is $0 \in \partial f(x) = G'_s(x) * \partial \|.\|_\infty (G_s(x))$. It is therefore reasonable to consider the program

$$d = -\frac{g}{\|g\|}$$

$$g = argmin\{\|\varphi_Y\| : Y = (Y_1, ..., Y_q)\} \tag{B.2.24}$$

which either shows that $0 \in \partial f(x)$, or produces the direction of the steepest descent at x if $0 \notin \partial f(x)$. By vectorizing $y = vec(Y)$, then we may represent φ_Y by a matrix vector product, $\varphi_Y = \Phi_y$. Program of eq. B.2.24 would then be equivalent to the following semi-definite programming

$$minimize\ t$$

$$subject\ to \begin{bmatrix} t & y^T \Phi^T \\ \Phi_y & tI \end{bmatrix} \succcurlyeq 0 \tag{B.2.25}$$

$$Y_i \succcurlyeq 0, \quad i = 1..., q$$

$$e^T y = 1$$

where $e^T y = 1$ encodes the constraint $\sum_i Tr(Y_i) = 1$. The direction d of steepest descent at x is then obtained as $d = -\Phi_y/\|\Phi_y\|$, where (t,y) is solution of eq. B.2.25.

Definition 4.4: Nonsmooth technique for H_∞ norm optimization algorithm.
Conclusively the steepest descent method for the H_∞ norm can be summarized as follows:

1. If $0 \in \partial f(x)$, stop the iteration, else

2. Solve eq. B.2.25 and determine the direction d of the steepest descent at x

3. Perform a line search and find a descent step $x^+ = x + td$

4. Replace x by x^+ and start again

Apkarian points out that this preliminary approach to the nonsmooth optimization may not converge due to function f nonsmoothness, he therefore further develops this algorithm into a more sophisticated first-order descent method which is not disclosed herein. Finally, the nonsmooth algorithm of minimizing the constrained H_∞ norm is numerically tested and compared to the full-order H_∞ norm and to other iterative methods for reduced-order control, namely the Frank and Wolfe (FW) and the augmented Lagrangian (AL) methods. The nonsmooth algorithm converge to a local minima for large scale systems whereas FW and AL seem unable to converge to a solution. However, for moderate systems (less than 100 states) NS and AL achieve more or less the same performance at the same K, yielding the same result.

B.3 Integrated H_∞ Structural & Control Design

In section B.2 the investigation of structured H_∞ synthesis for fixed-structured, fixed-order controller K has been presented, covering the theoretical background in B.2 and its numerical application in section 3.2; however what is going to be optimized is yet unspecified. Possible approaches would be to optimize the static gain parameters of a PID controller under the problem formulated in B.2.3 or even go for an observer-based controller. However, the concept of simultaneously designing the behavior of the structural model included in the generalized plant (barges-topside in the scope of the Thesis) along with the controller parameters (link in between barges) and satisfy the prescribed performance specifications as first developed by Grigoriadis and Wu (1997) was considered appealing. By extracting the stiffness and damping scalar parameters of the link diagonal members from the generalized plant and making them tunable terms of a diagonal controller $K(s)$, we achieve to compute the stiffness and damping values which correspond to system's suboptimal performance. [Grigoriadis and Wu (1997); Grigoriadis and Skelton (1998)] work preceded [Apkarian and Noll (2006)] nonsmooth algorithm and consequently employs instead an iterative two-step procedure by splitting one nonconvex to two convex problems; successively a controller design and a plant/controller redesign step.More specifically, assuming that the plant state-space parameters (eq. B.2.4) are all affine functions of a design parameter $\theta \, \epsilon \, \mathbb{R}$ so the generalized plant is now of the form

$$P(s) = \begin{bmatrix} A(\theta) & B_1(\theta) & B_2(\theta) \\ C_1(\theta) & 0 & D_{12}(\theta) \\ C_2(\theta) & D_{21}(\theta) & 0 \end{bmatrix} \tag{B.3.1}$$

the optimization can be casted on two steps.

- Step 1: Fix θ so for determined $A(\theta)$, $B_1(\theta)$, $C_1(\theta)$ solve the minimization problem $\|T_{wz}\|_\infty < \gamma$ and get the output feedback controlled data $\hat{A}_k$, $\hat{B}_k$, $\hat{C}_k$, $\hat{D}_k$.

- Step 2: Fix symmetric matrices R, $S > 0$ and solve the optimization problem again subject to the new controller data, so to obtain a new value of θ and controlled values $\hat{A}_k$, $\hat{B}_k$, $\hat{C}_k$, $\hat{D}_k$. This iteration stops when $|\gamma_{i+1} - \gamma_i| < \varepsilon$, where ε is a prescribed iteration tolerance. Nominal performance is thus achieved by solving each step by an LMI as shown in Theorem 4.2 below.

Theorem 4.2 Integrated H_∞ Plant/Controller Design via two-step successive LMIs
Considering a n-order LTI system with the state space representation

$$\begin{bmatrix} \dot{x} \\ e \\ y \end{bmatrix} = \begin{bmatrix} A(\theta) & B_1(\theta) & B_2(\theta) \\ C_1(\theta) & 0 & D_{12}(\theta) \\ C_2(\theta) & D_{21}(\theta) & 0 \end{bmatrix} \begin{bmatrix} x \\ w \\ u \end{bmatrix}$$

Then the following statement hold: there exist symmetric matrices R, $S > 0$ such that

$$\begin{bmatrix} N_R & 0 \\ 0 & I \end{bmatrix}^T \begin{bmatrix} AR + RA^T & RC_1^T & B_1 \\ C_1 R & -\gamma I & 0 \\ B_1^T & 0 & -\gamma I \end{bmatrix} \begin{bmatrix} N_R & 0 \\ 0 & I \end{bmatrix} < 0$$

$$\begin{bmatrix} N_S & 0 \\ 0 & I \end{bmatrix}^T \begin{bmatrix} SA + A^T S & SB_1 & C_1^T \\ B_1^T S & -\gamma I & 0 \\ C_1 & 0 & -\gamma I \end{bmatrix} \begin{bmatrix} N_S & 0 \\ 0 & I \end{bmatrix} < 0$$

$$\begin{bmatrix} R & I \\ I & S \end{bmatrix} \geqq 0$$

where N_R, N_s denote the null spaces of $\begin{bmatrix} B_2^T & D_{12}^T \end{bmatrix}$ and $[C_2 \ \ D_{21}]$ respectively.

Based on the idea of Grigoriadis, [Camino et al. (2003)] further extended the integrated structural and control design by introducing a 'convexifying' function so to make the structural constraint convex and solve the convergence problem for lower-order controllers, since by that time, all algorithms were formulated entirely in the LMI/ARE framework, making the nonconvex optimization problems intractable in yielding a local minima. This convexifying function disappears at a saddle point of one iteration and gets updated for the next step. Camino also argues that his methodology can incorporate different types of performance constraints (i.e. system control effort and output upper bound) while the algorithm does not fix the Lyapunov matrices (matrices R, S in Theorem 4.2 just formulated above), making the tuning of the mass matrix possible along with the stiffness and damping matrices. For further information on the formulation of the convexifying function, one may refer to Camino et al. (2003); De Oliveira et al. (2000). Finally, the algorithm is being numerically tested for a simple structural model simulating the behavior of a 3-storey building to earthquake excitation. Various successive examples of letting structural parameters free to optimization are presented along with comparison of the algorithm performance to the various examples. In an effort to validate these results, a simplifying recreation of his aforementioned case study is carried out by incorporating Apkarian's nonsmooth algorithm in section 3.1, yielding similar stiffness and damping output values and showing that the nonsmooth approach can be well implemented numerically in the concept of integrated structural & control design via the `hinfstruct` algorithm in Matlab.

B.4 Essential definitions on Motion Control

Linear Fractional Transformation

Definition   A mapping $F : \mathbb{C} \mapsto \mathbb{C}$ of the form:

$$F(s) = \frac{a + bs}{c + ds} \tag{B.4.1}$$

with a,b,c and d ϵ $\mathbb{C}$ is called a linear fractional transformations (abbrev. LFT). If $c \neq 0$ then $F(s) = \alpha + \beta s(1 - \gamma s)^{-1}$. The same concept can be applied in matrix algebra, considering a complex matrix

$$P = \begin{pmatrix} P_{11} & P_{12} \\ P_{21} & P_{22} \end{pmatrix} \tag{B.4.2}$$

and another complex matrix K of compatible size (the structural controller). A lower and a upper LFT can be defined as follows, provided that the LFT definition is well-posed (inverse matrices exist, Zhou et al. (1996)):

$$F_l(P, K) = P_{11} + P_{12}K(I - P_{22}K)^{-1}P_{21} \tag{B.4.3}$$

$$F_u(P, K) = P_{22} + P_{21}K(I - P_{11}K)^{-1}P_{12} \tag{B.4.4}$$

Application   A feedback control system can be rearranged as an LFT and is widely used as a method to standardize block diagrams for robust control analysis and design. Referring back to fig B.2.1, the block diagram formulation is transformed in matrix notation

$$\begin{bmatrix} z \\ v \end{bmatrix} = \begin{bmatrix} P_{11} & P_{12} \\ P_{21} & P_{22} \end{bmatrix} \begin{bmatrix} w \\ u \end{bmatrix}, \; u = Kv \tag{B.4.5}$$

and its respective LFT would have the following form:

$$T_{zw} = F_l(P, K) = P_{11} + P_{12}K(I - P_{22}K)^{-1}P_{21} \tag{B.4.6}$$

Hamiltonian Matrix

A Hamiltonian matrix is a $2n$ x $2n$ matrix A such that JA is symmetric, where J is the skew symmetric matrix

$$J = \begin{bmatrix} 0 & I_n \\ -I_n & 0 \end{bmatrix}$$

and I_n the n x n identity matrix. In other words, A is Hamiltonian if and only if $(JA)^T = JA$.

The Riccati Operator

Let A,Q,R be real n x n matrices with Q and R symmetric. Define the $2n$ x $2n$ Hamiltonian matrix

$$H := \begin{bmatrix} A & R \\ Q & -A' \end{bmatrix} \tag{B.4.7}$$

Assume H has no eigenvalues on the imaginary axis. Then it must have n eigenvalues in $Re(s) < 0$ and n in $Re(s) > 0$. Consider the two n- dimensional spectral subspaces $\Phi_-(H)$ and $\Phi_+(H)$: the former is the invariant subspace corresponding to eigenvalues in $Re(s) < 0$; the latter to eigenvalues in $Re(s) > 0$. Finding a basis for $\Phi_-(H)$, stacking the basis vectors up to form a matrix and partitioning it we get

$$\Phi_-(H) = Im \begin{bmatrix} X_1 \\ X_2 \end{bmatrix} \tag{B.4.8}$$

where $X_1, X_2 \, \epsilon \, R^{nxn}$. If X_1 is nonsingular or equivalently the two subspaces

$$\Phi_-(H), \; Im \begin{bmatrix} 0 \\ I \end{bmatrix} \tag{B.4.9}$$

we can set $X := X_2 X_1^{-1}$. Then X is uniquely determined by $H \to X$ which is a function denoted as Ric; thus $X = Ric(H)$. We will take the domain of Ric, denoted $Dom(Ric)$ to consist of Hamiltonian matrices H with two properties, namely H has no eigenvalues in the imaginary axis and the two subspaces in B.4.9 are complementary, hence refered to as stability and complementary properties, respectively. The following results give some properties of X as well as verifiable conditions under which H belongs to $Dom(Ric)$. The definition given above and the following Lemmas on the Riccati operator can also be found in Doyle et al. (1989).

Lemma 1 (Bounded Real Lemma)   Suppose $H \, \epsilon \, Dom(Ric)$ and $X = Ric(H)$. Then:

- X is symmetric;

- X satisfies the following algebraic Riccati equation

$$A'X + XA + XRX + -Q = 0$$

- $A + RX$ is stable.

Lemma 2   Suppose H has no imaginary eigenvalues, R is either positive semidefinite or negative semidefinite and (A, R) is stabilizable. Then $H \, \epsilon \, Dom(Ric)$

Lemma 3   Suppose H has the form

$$H = \begin{bmatrix} A & -BB' \\ -C'C & -A' \end{bmatrix}$$

with (A, B) stabilizable and (C, A) detectable (denote the unobservable subspace by Φ). Then $H \, \epsilon \, Dom(Ric)$, $X = Ric(H) \geqq 0$, and $ker(X) \subset \Phi$.

Computing the H_∞ Norm

For the transfer function $G(s)$, with A stable and $\gamma > 0$, define the Hamiltonian matrix

$$H := \begin{bmatrix} A & \gamma^{-2}BB' \\ -C'C & -A' \end{bmatrix}$$

Lemma 4 The following conditions are equivalent (the proof of Lemma 4 is given in Boyd et al. (1989))

- $\|G\|_\infty < \gamma$

- H has no eigenvalues on the imaginary axis

- $H \; \epsilon \; Dom(Ric)$

- $H \; \epsilon \; Dom(Ric)$ and $Ric(H) \geqq 0$ ($Ric(H) > 0$ if (C,A) is observable)

The equivalence of b and c follows from Lemma 2, while the equivalence of c and d follows from Lemma 1. Equivalently for the calculation of the H_∞ norm the next Lemma can be used (its proof is given in Zhou et al. (1996)).

Lemma 5 Let $\gamma > 0$ and

$$G(s) = \begin{bmatrix} A & B \\ C & D \end{bmatrix} \; \epsilon \; RL_\infty$$

Then $\|G\|_\infty < \gamma$ if and only if $\overline{\sigma}(D) < \gamma$ and H has no eigenvalues in the imaginary axis where

$$H = \begin{bmatrix} A + BR^{-1}D^T C & BR^{-1}B^T \\ -C^T(I + DR^{-1}D^T)C & -(A + BR^{-1}D^T C)^T \end{bmatrix} \tag{B.4.10}$$

for $R = \gamma^2 I - D^T D$.

Bibliography

Apkarian, P., P. Gahinet, and C. Buhr (2014). Multi-model, multi-objective tuning of fixed-structure controllers. In *Control Conference (ECC), 2014 European*, pp. 856–861. IEEE.

Apkarian, P. and D. Noll (2006). Nonsmooth h∞ synthesis. *Automatic Control, IEEE Transactions on 51*(1), 71–86.

Aström, K. J. and R. M. Murray (2010). *Feedback systems: an introduction for scientists and engineers*. Princeton university press.

Benne, K. (2014). Alternative methods for offshore topsides lifting. Master's thesis, TU Delft.

Boyd, S., V. Balakrishnan, and P. Kabamba (1989). A bisection method for computing the h∞ norm of a transfer matrix and related problems. *Mathematics of Control, Signals and Systems 2*(3), 207–219.

Buchner, B., A. Van Dijk, J. De Wilde, et al. (2001). Numerical multiple-body simulations of side-by-side mooring to an fpso. In *The Eleventh International Offshore and Polar Engineering Conference*. International Society of Offshore and Polar Engineers.

Burke, J., D. Henrion, A. Lewis, and M. Overton (2006). Hifoo-a matlab package for fixed-order controller design and h∞ optimization. In *Fifth IFAC Symposium on Robust Control Design, Toulouse*.

Camino, J. F., M. C. de Oliveira, and R. E. Skelton (2003). Convexifying linear matrix inequality methods for integrating structure and control design. *Journal of Structural Engineering 129*(7), 978–988.

Chen, X. (2011). Offshore hydrodynamics and applications. *The IES Journal Part A: Civil & Structural Engineering 4*(3), 124–142.

Chen, X.-B. (2005). Hydrodynamic analysis for offshore lng terminals. In *Proceedings of the 2nd International Workshop on Applied Offshore Hydrodynamics, Rio de Janeiro*.

Cummins, W. (1962). The impulse response function and ship motions. Technical report, DTIC Document.

De Oliveira, M., J. Camino, and R. Skelton (2000). A convexifying algorithm for the design of structured linear controllers. In *Decision and Control, 2000. Proceedings of the 39th IEEE Conference on*, Volume 3, pp. 2781–2786. IEEE.

Doyle, J. C., K. Glover, P. P. Khargonekar, and B. A. Francis (1989). State-space solutions to standard h 2 and h∞ control problems. *Automatic Control, IEEE Transactions on 34* (8), 831–847.

Fournier, J.-R., M. Naciri, and X.-B. Chen (2006). Hydrodynamics of two side-by-sidevessels. experiments & numericalsimulations.

Gahinet, P. and P. Apkarian (1994). A linear matrix inequality approach to h∞ control. *International journal of robust and nonlinear control 4* (4), 421–448.

Gahinet, P. and P. Apkarian (2011). Structured h∞ synthesis in matlab. *Proc. IFAC, Milan, Italy*.

Grigoriadis, K. M. and R. E. Skelton (1998). Integrated structural and control design for vector second-order systems via lmis. In *American Control Conference, 1998. Proceedings of the 1998*, Volume 3, pp. 1625–1629. IEEE.

Grigoriadis, K. M. and F. Wu (1997). Integrated h∞ plant/controller design via linear matrix inequalities. In *Decision and Control, 1997., Proceedings of the 36th IEEE Conference on*, Volume 1, pp. 789–790. IEEE.

Gu, D.-W. (2005). *Robust control design with MATLAB®*, Volume 1. Springer Science & Business Media.

Huijsmans, R., J. Pinkster, J. De Wilde, et al. (2001). Diffraction and radiation of waves around side-by-side moored vessels. In *The Eleventh International Offshore and Polar Engineering Conference*. International Society of Offshore and Polar Engineers.

Jamieson, A. (2013). Decommissioning in north sea. Technical report, Royal Acadamy of Engineering.

Janssen, R. (2013). A novel strategy for the identification of radiation force models; a constrained, frequency domain approach. Master's thesis, TU Delft.

Journèe, J. M. and W. Massie (2001). Offshore hydrodynamics. *Delft University of Technology 4*, 38.

Limebeer, D. and G. Halikias (1988). An analysis of pole-zero cancellations in h∞ optimal control problems of the second kind. *SIAM J. Control Optim. 26*, 646.

Newman, J. (2003). Application of generalized modes for the simulation of free surface patches in multi body hydrodynamics. *Proc. 4th annual WAMIT Consortium report*, 8–9.

Newman, J. (2004). Progress in wave load computations on offshore structures. In *Invited Lecture, 23th OMAE Conference, Vancouver, Canada, http://www. wamit. com/publications*.

Newman, J. and C. Lee (1999). Heave response of a semi-submersible near resonance. In *International Workshop on Wa-ter Waves and Floating Bodies*.

Ogilvie, T. F. (1964). Recent progress toward the understanding and prediction of ship motions. In *5th Symposium on naval hydrodynamics*, Volume 1, pp. 2–5. Bergen, Norway.

Pauw, W. H., R. H. Huijsmans, and A. Voogt (2007). Advances in the hydrodynamics of side-by-side moored vessels. In *ASME 2007 26th International Conference on Offshore Mechanics and Arctic Engineering*, pp. 597–603. American Society of Mechanical Engineers.

Perez, T. (2006). *Ship motion control: course keeping and roll stabilisation using rudder and fins*. Springer Science & Business Media.

Perez, T. and T. I. Fossen (2008). Joint identification of infinite-frequency added mass and fluid-memory models of marine structures. *Modeling, Identification and Control 29*(3), 93–102.

Sea, S. E. . D. N. (2014). Decommissioning in the north sea. Technical report, ARUP.

Skogestad, S. and I. Postlethwaite (2007). *Multivariable feedback control: analysis and design*, Volume 2. Wiley New York.

Sun, L., R. E. Taylor, and P. H. Taylor (2010). First-and second-order analysis of resonant waves between adjacent barges. *Journal of Fluids and Structures 26*(6), 954–978.

Taghipour, R., T. Perez, and T. Moan (2008). Hybrid frequency–time domain models for dynamic response analysis of marine structures. *Ocean Engineering 35*(7), 685–705.

van Solingen, E., J.-W. van Wingerden, R. De Breuker, and M. Verhaegen (2014). Optimization of linear parameterizable h∞ controllers in the frequency domain. In *World Congress*, Volume 19, pp. 736–741.

Wang, S. (2015). Multibody dynamic analysis of the lift-off operation. Master's thesis, Delft University of Technology.

Zames, G. (1981). Feedback and optimal sensitivity: Model reference transformations, multiplicative seminorms, and approximate inverses. *Automatic Control, IEEE Transactions on 26*(2), 301–320.

Zhou, K., J. C. Doyle, K. Glover, et al. (1996). *Robust and optimal control*, Volume 40. Prentice hall New Jersey.

Zhou, K. and P. P. Khargonekar (1988). An algebraic riccati equation approach to h∞ optimization. *Systems & Control Letters 11*(2), 85–91.